UNIVERSITAT POLITÈCNICA DE VALÈNCIA

DEPARTAMENTO DE MAQUINAS Y MOTORES TERMICOS

ANALYTICAL AND EXPERIMENTAL INVESTIGATION OF TEMPERATURE-SWING INSULATION ON ENGINE PERFORMANCE

Doctoral Thesis for the degree of Doctor of Philosophy

Presented by: Peter Andruskiewicz
Supervised by: Professor Raul Payri

Tribunal Members:	Dr. Antonio José Torregrosa	President
	Dr. Pedro Acisclo Rodriguez	Secretary
	Dr. Todd David Fansler	Vocal

Valencia, Spain
September, 2017

DOCTORAL THESIS

ANALYTICAL AND EXPERIMENTAL INVESTIGATION OF TEMPERATURE-SWING INSULATION ON ENGINE PERFORMANCE

Presented by: Peter Andruskiewicz

Supervised by: Professor Raúl Payri

REVIEWERS	TRIBUNAL MEMBERS
Dr. Todd David Fansler	Dr. Antonio José Torregrosa
Dr. Juan José Hernández	Dr. Pedro Acisclo Rodriguez
Dr. Mark Aaron Hoffman	Dr. Todd David Fansler

Valencia, Spain

September, 2017

Resumen

Los materiales aislantes han sido investigados a fondo por sus posibles mejoras en la eficiencia térmica de los motores de combustión interna alternativos. Estas mejoras se ven reflejadas tanto directamente en el trabajo indicado como indirectamente a través de la reducción del sistema de refrigeración del propio motor. Diferentes estudios, tanto experimentales como analíticos, han mostrado la reducción en la transferencia de calor a través de las paredes de la cámara de combustión mediante la utilización de estos materiales. Sin embargo, demostrar la conversión de la energía térmica adicional en trabajo indicado ha resultado más difícil. En ciertos estudios se pudieron obtener mejoras en el trabajo indicado durante la carrera de expansión, pero éstas fueron reducidas debido a un menor rendimiento volumétrico debido al calentamiento de la carga durante el proceso de admisión y un mayor trabajo en la carrera de compresión. Típicamente, las únicas mejoras en el trabajo al freno provendrían de la reducción de pérdidas por bombeo en los motores turboalimentados, o de la extracción de la energía adicional de los gases de escape a través de turbinas.

El concepto de los materiales con oscilación de la temperatura durante el ciclo motor intenta aprovechar los beneficios del aislamiento durante los procesos de combustión y expansión, mitigando las perdidas por el incremento de la temperatura de las paredes durante la admisión y la compresión. La combinación de baja capacidad calorífica y baja conductividad térmica permitiría que la temperatura de la superficie de la cámara de combustión respondiera rápidamente a la temperatura del gas durante el proceso de combustión. Las temperaturas de la superficie son capaces de aumentar en respuesta al pico de flujo de calor, minimizando así la diferencia de temperatura entre el gas y la pared en la carrera de expansión cuando es posible la mayor conversión de energía térmica en trabajo mecánico. La combinación de baja capacidad calorífica y conductividad térmica es también esencial para permitir este aumento de temperatura durante la combustión y para permitir que la superficie se enfríe durante la expansión y el escape para no perjudicar así el rendimiento volumétrico del motor durante la carrera de admisión y minimizar el trabajo de compresión realizado en el siguiente ciclo.

En esta tesis se han desarrollado modelos térmicos y termodinámicos para predecir los efectos de las propiedades de los materiales en las paredes y caracterizar los efectos de la transferencia de calor en diferentes partes del ciclo sobre el trabajo indicado, el rendimiento volumétrico, la energía en los gases de escape y las temperaturas del gas para un motor de combustión interna alternativo. También se ha evaluado el impacto del uso de estos materiales en el knock en motores de combustión de encendido provocado, ya que los estudios experimentales de esta tesis se realizaron en un motor de estas características.

Durante la investigación se evaluaron materiales aislantes convencionales para comprender el estado actual de esta técnica y para adquirir también experiencia en el análisis de materiales aislantes con oscilación de temperatura. Desafortunadamente, los efectos de la permeabilidad a través de la porosidad del material en los recubrimientos convencionales, la absorción de combustible y la relación de compresión tendieron a ocultar los efectos de la oscilación de la temperatura y la reducción de la transferencia de calor a través de las paredes. Así pues, se analizó el impacto individual de cada uno de estos mecanismos y su influencia en el rendimiento del motor para así definir un nuevo material con las características necesarias que mejorasen el aislante con de oscilación de temperatura.

Finalmente, a partir de los estudios de esta fase de análisis, se creó un nuevo material y se aplicó a la superficie del pistón y a la superficie interna de las válvulas de admisión y de escape. Los datos de motor se tomaron con estos componentes recubiertos del nuevo material aislante con oscilación de temperatura y se compararon con los datos de referencia del mismo motor donde no se utilizó recubrimiento. Aunque el material resistió en la mayoría de ensayos experimentales, el análisis de los datos sugiere que el material no estaba completamente sellado y sufrían las mismas pérdidas de permeabilidad que afectaban al aislamiento convencional. Esta investigación demuestra que es necesario un desarrollo adicional para llegar a una solución robusta y eficaz que minimice la transferencia de calor a través de las paredes de la cámara de combustión mediante materiales aislantes con oscilación de la temperatura para motores de combustión interna. El éxito de estos materiales aislantes con oscilación de temperatura requiere una muy baja conductividad térmica, capacidad calorífica y un espesor de aislamiento apropiado, así como sellado elástico de cualquier volumen poroso dentro del revestimiento para evitar pérdidas adicionales de calor y de combustible a lo largo del ciclo.

Resum

Els materials aïllants han estat investigats a fons per les seves possibles millores en l'eficiència tèrmica en el motors de combustió interna alternatius. Aquestes millores es veuen reflectides tant directament en el treball indicat com indirectament a través de la reducció del sistema de refrigeració del propi motor. Diferents estudis, tant experimentals com analítics, han mostrat la reducció en la transferència de calor a través de les parets de la cambra de combustió mitjançant la utilització d'aquests materials. No obstant això, demostrar la conversió de l'energia tèrmica addicional en treball indicat ha resultat més difícil. En certs estudis es van poder obtenir millores en el treball indicat durant la carrera d'expansió, però aquestes van ser reduïdes a causa d'un menor rendiment volumètric causat de l'escalfament de la càrrega durant el procés d'admissió i un major treball en la carrera de compressió. Típicament, les úniques millores en el treball al fre provindrien de la reducció de pèrdues per bombeig en els motors turbo alimentats, o de l'extracció addicional de l'energia dels gasos d'escapament a través de turbines.

El concepte dels materials amb oscil·lació de la temperatura durant el cicle motor intenta aprofitar els beneficis de l'aïllament durant els processos de combustió i expansió, mitigant les perdudes per l'increment de la temperatura de les parets durant l'admissió i la compressió. La combinació de baixa capacitat calorífica i baixa conductivitat tèrmica permetria que la temperatura de la superfície de la cambra de combustió respongués ràpidament a la temperatura del gas durant el procés de combustió. Les temperatures de la superfície són capaços d'augmentar en resposta al flux de calor, minimitzant així la diferència de temperatura entre el gas i la paret en la carrera d'expansió quan és possible la major conversió d'energia tèrmica en treball mecànic. La combinació de baixa capacitat calorífica i conductivitat tèrmica és també essencial per permetre aquest augment de temperatura durant la combustió i el refredament de la superfície durant l'expansió i l'escapament per no perjudicar així el rendiment volumètric del motor durant la carrera d'admissió i minimitzar el treball de compressió realitzat en el següent cicle.

En aquesta tesi s'han desenvolupat models tèrmics i termodinàmics per predir els efectes de les propietats dels materials en les parets i caracteritzar els efectes de la transferència de calor en diferents parts del cicle sobre el treball indicat, el rendiment volumètric, l'energia en els gasos d'escapament i les temperatures del gas per un motor de combustió interna alternatiu. També s'ha avaluat l'impacte d'aquests materials en el knock en motors de combustió d'encesa provocada, ja que les proves experimentals d'aquesta tesi es van realitzar en un motor d'aquestes característiques.

Durant la investigació es van avaluar materials aïllants convencionals per comprendre l'estat actual d'aquesta tècnica i per adquirir també experiència en

l'anàlisi de materials aïllants amb oscil·lació de temperatura. Desafortunadament, els efectes de la permeabilitat a través de la porositat del material en el recobriment convencional, l'absorció de combustible i la relació de compressió van tendir a ocultar els efectes de l'oscil·lació de la temperatura i la reducció de la transferència de calor a través de les parets. Així doncs, es va analitzar l'impacte individual de cada un d'aquests mecanismes i la seva influència en el rendiment del motor per així definir un nou material amb les característiques necessàries que milloressin el aïllant d'oscil·lació de temperatura.

Finalment, a partir dels estudis d'aquesta fase d'anàlisi, es va crear un nou material i es va aplicar a la superfície del pistó i a la superfície interna de les vàlvules d'admissió i d'escapament. Les dades de motor es van prendre amb aquests components recoberts del nou material aïllant amb oscil·lació de temperatura i es van comparar amb les dades de referència del mateix motor on no es va utilitzar recobriment. Encara que algunes el material va resistir en la majoria d'assajos experimentals, l'anàlisi de les dades suggereix que no estaven completament segellats i patien les mateixes pèrdues de permeabilitat que afectaven a l'aïllament convencional. Aquesta investigació demostra que cal un desenvolupament addicional per arribar a una solució robusta i eficaç en els motors de combustió interna alternatius que minimitzi la transferència de calor a través les parets de la cambra de combustió mitjançant materials aïllants amb oscil·lació de la temperatura. L'èxit dels materials aïllants amb oscil·lació de temperatura requereix una molt baixa conductivitat tèrmica, capacitat calorífica i un gruix d'aïllament apropiat, així com un segell elàstic de qualsevol volum porós dintre del revestiment per evitar pèrdues addicionals de calor i de combustible al llarg del cicle.

Abstract

In-cylinder thermal barrier materials have been thoroughly investigated for their potential improvements in thermal efficiency in reciprocating internal combustion engines. These materials show improvements both directly in indicated work and indirectly through reduced demand on the cooling system. Many experimental and analytical sources have shown reductions in heat losses to the combustion chamber walls, but converting the additional thermal energy to indicated work has proven more difficult. Gains in indicated work over the expansion stroke could be made, but these were negated by increased compression work and reduced volumetric efficiency due to charge heating. Typically, the only improvements in brake work would come from the pumping loop in turbocharged engines, or from additional exhaust energy extraction through turbine-compounding devices.

The concept of inter-cycle wall-temperature-swing holds promise to reap the benefits of insulation during combustion and expansion, while not suffering the penalties incurred with hotter walls during intake and compression. The combination of low volumetric heat capacity and low thermal conductivity would allow the combustion chamber surface temperature to quickly respond to the gas temperature throughout combustion. Surface temperatures are capable of rising in response to the spike in heat flux, thereby minimizing the temperature difference between the gas and wall early in the expansion stroke when the greatest conversion of thermal energy to mechanical work is possible. The combination of low heat capacity and thermal conductivity is essential in allowing this temperature increase during combustion, and in enabling the surface to cool during expansion and exhaust to avoid harmfully affecting engine volumetric efficiency during the intake stroke and minimizing compression work performed on the next stroke.

In this thesis, thermal and thermodynamic models are constructed in an attempt to predict the effects of material properties in the walls, and to characterize the effects of heat transfer at different portions of the cycle on indicated work, volumetric efficiency, exhaust energy and gas temperatures of a reciprocating internal combustion engine. The expected impact on combustion knock in spark-ignited engines was also considered, as this combustion mode was the basis for the experimental engine testing performed.

Conventional insulating materials were evaluated to benchmark the current state-of-the-art, and to gain experience in the analysis of materials with temperature-swing capability. Unfortunately, the effects of permeable porosity within the conventional coating on heat losses, fuel absorption and compression ratio tended to mask the effects of temperature swing. The individual impact of each of these loss mechanisms

on engine performance was analyzed, and the experience helped to further refine the necessary traits of a successful temperature-swing material

Finally, from the learnings of this analysis phase, a novel material was created and applied to the piston surface, intake valve faces, and exhaust valve faces. Engine data was taken with these coated components and compared to an un-coated baseline. While some of the test pieces physically survived the testing, analysis of the data suggests that they were not fully sealed and suffered from the same permeability losses that affected the conventional insulation. Further development is necessary to arrive at a robust, effective solution for minimizing heat transfer through wall temperature swing in reciprocating internal combustion engines. The success of temperature-swing thermal barrier materials requires very low thermal conductivity, heat capacity, and appropriate insulation thickness, as well as resilient sealing of any porous volume within the coating to avoid additional heat and fuel energy losses throughout the cycle.

To my wife Helen and son Paul, who are my inspiration for reaching further…

Acknowledgements

I would like to acknowledge all of the guidance and support offered by my co-workers Paul Najt, Russell Durrett, Orgun Guralp, Arun Solomon, Vicent Domenech-Llopis, and the rest of the SI and CI groups at GM Research. You have been invaluable to the completion of this thesis, as well as my personal and professional development.

Without the efforts of Ronald Otto, Gerald Malta, Karon Allen, William Osad, and the GM R&D Technical Operations teams, it would have been impossible to acquire the experimental data necessary for this body of work. Thank you for your tireless efforts.

I am indebted to my advisor, Dr. Raúl Payri, for his continuous work in keeping me focused on the thesis program goals, providing essential editorial feedback, and for assisting with all of the administrative aspects regarding the degree. Raúl, you have provided irreplaceable clarity throughout the entire process.

My parents and brother have provided me with a strong foundation, supplying the stability, determination, creativity, and mental fortitude that has allowed me to get as far as I have.

Finally, I have to thank my loving wife, Helen, for supporting me throughout this endeavor. None of this would have been possible without you. Furthermore, you provide the motivation to reach further and strive for more in order to make a better life together with our new son, Paul. From one challenge to another; “Every new beginning comes from some other beginnings’ end.” (Semisonic, 1998)

Contents

Abstract

Acknowledgements

Contents ..... **i**

List of Figures ..... **iv**

List of Tables ..... **vi**

Nomenclature ..... **vii**

1. Introduction **1**

1.1. General Context 1
1.2. Motivation 1
1.3. Methodology 2
1.3.1 Literature Review Overview 3
1.3.2 Requirements for Industrialization 7
1.3.3 Wall Temperature Modeling 8
1.3.4 Investigation of Desired Properties 8
1.3.5 Experimental and Analytic Investigations 8
1.3.6 Novel Thermal Barrier Material Development 9
1.4. Thesis Outline 9

2. Literature Review **11**

2.1. Introduction 11
2.2. Heat Transfer Background 11
2.3. Measurement and Estimation of In-Cylinder Heat Transfer 12
2.4. Spark-Ignited Combustion Background 15
2.5. Conventional Insulation in Literature 22
2.6. Temperature-Swing Insulation in Literature 31

3. Experimental Apparatus and Methods 37

3.1. Introduction 37
3.2. Material Properties Measurement 37
3.2.1 Thermal Diffusivity 37
3.2.2 Heat Capacity 38
3.3. Experimental Engine and Test Facilities 39
3.4. Experimental Methodology 41
3.5. Experimental Data Analysis 43
3.5.1 Initial Calculations 43
3.5.2 Crevice/Porosity Model 45
3.5.3 In-Cylinder Properties 46
3.5.4 Heat Transfer Estimation 49
3.5.5 Heat Release Calculation 50
3.5.6 Energy Closure 51
3.5.7 Knock Amplitude 53
3.6. Heat Flux Probe 53
3.6.1 Probe Construction and Operation 54
3.6.2 Conversion to Temperature and Heat Flux 55

4. Computational Methods 57

4.1. Introduction 57
4.2. 0D/1D Engine Thermodynamic Model 57
4.2.1 Model Description 57
4.2.2 Calibration to Experimental Data 58
4.3. 2D Thermal Wall Model 59
4.3.1 General Model Formulation 59
4.3.2 Optimal Finite-Element Organization 64
4.3.3 Component Temperature Initialization & Solution 68
4.3.4 Wall Temperature Model Validation 69
4.3.5 Model Calibration with Experimental Data 70
4.3.6 Discussion of Thermal Wall Model 74
4.4. Coupling Thermodynamic & Thermal Models 75

4.5. Coupling Experimental Data Analysis & Thermal Model 76
4.6. Summary and Conclusions 77

5. Analytical Material Properties Investigations 79

5.1. Introduction 79
5.2. Fixed Thermodynamic Conditions 79
5.2.1 Model Formulation 80
5.2.2 Analysis & Results 80
5.3. Variable Thermodynamic Conditions 86
5.3.1 Simple Engine Geometry 86
5.3.2 Realistic Engine Geometries 91
5.4. Summary and Conclusions 94

6. Conventional Materials: Experimental Investigations 97

6.1. Introduction 97
6.2. Conventional Insulating Materials 97
6.3. Test Plan 99
6.4. Analysis and Results 100
6.4.1 Experimental Results 100
6.4.2 Simulated Performance 109
6.5. Summary and Conclusions 114

7. Novel Materials: Development and Testing 117

7.1. Introduction 117
7.2. Material Requirements 117
7.3. Material Structure and Application 118
7.4. Measured Properties 121
7.5. Experimental Results 122
7.6. Summary and Conclusions 127

8. Conclusions and Future Directions 129

8.1. Summary and Conclusions 129
8.2. Future Work and Directions 131

9. Works Cited 133

List of Figures

Figure 1-1: Material Thermal Properties and Estimated Temperature Swings 5

Figure 3-1: Thermal Diffusivity Measurement Technique 37

Figure 3-2: Combustion Chamber Schematic for Single-Cylinder Experimental Engine (Contoured Piston) 39

Figure 3-3: Combustion Chamber Temperature Calculation Regimes 47

Figure 3-4: Cylinder Mass and Valve Flow Calculation at 2000 RPM, 20 mg/cycle Fueling Point 48

Figure 3-5: Energy Accounting and Closure in Data Analysis Program 52

Figure 3-6: Knock Frequency Filtering and Amplitude Calculation 53

Figure 3-7: Heat Flux Sensor Construction, from (Hoffman, 2012) 54

Figure 3-8: Heat Flux Probe Cold Junction and Amplification 55

Figure 4-1: Thermodynamic Model vs Experimental Pressure and Temperature Comparison 58

Figure 4-2: Thermodynamic Model vs Experimental Convection Coefficient and Total Heat Loss Comparison 59

Figure 4-3: Piston and Bore 2D Component, Path and Layer Depiction 62

Figure 4-4: Valves and Head 2D Component, Path and Layer Depiction 63

Figure 4-5: Surface Temperature Compensation Results vs. Node-as-Surface Temperature Assumption 64

Figure 4-6: Analytical Solution of the Decay of Temperature Swing with Depth in Continuous Material 65

Figure 4-7: Optimized 1-Dimensional Finite Element Mesh for Layered Materials .. 66

Figure 4-8: Heat Transfer Within and Between Paths in a Component 67

Figure 4-9: Validation of Wall Temperature Model with Commercially Available Software 70

Figure 4-10: Thermal Model Calibration to Conditionally Averaged Crank-Angle-Resolved, Cycle-Averaged, and Spatially Averaged Piston and Head Measurements 71

Figure 4-11: Intake and Exhaust Valve Calibration, using Spatially and Temporally Averaged Surface Temperatures 74

Figure 5-1: Surface Temperature Swing for Various Hypothetical Materials at 100% $Depth_{1\%}$ 80

Figure 5-2: Thermal Resistance of Coating Layer and Heat Flux during Intake Stroke 82

Figure 5-3: Effects of Coating Thickness on Temperature Profile throughout Wall Thickness, on Temperature Swing, Intake Stroke Heating and Expansion Stroke Heat Losses 83

Figure 5-4: Coating Thickness Effects on Surface Temperature Profile, Effects of Material Thermal Properties on Expansion Heat Flux at 25% $Depth_{1\%}$ Coating Thickness 85

Figure 5-5: Surface Temperatures and Total Heat Transfer Rates at 2000 RPM, 60 mg Fueling Point 88

Figure 5-6: Difference in Heat Transfer Rate and Gas Temperature between Cases and Baseline 89

Figure 5-7: Logarithmic P-V and Difference in Instantaneous Indicated Piston Power from Baseline 90

Figure 5-8: Surface Temperatures and Total Heat Transfer Rates for Complete Engine Geometry 92

Figure 5-9: Piston Surface Temperatures and Total Heat Transfer Rates for All Points 93

Figure 5-10: Differences in Energies, NSFC and Volumetric Efficiency for All Points from Baseline 94

Figure 6-1: Crystalline Structure of a sample of Anisotropic BNT Material, from (Applied Thin Films Inc., 2011) 98

Figure 6-2: BNT-Coated Pistons Prior to Installation in Experimental Engine 99

Figure 6-3: Reduction in Compression Ratio and Increase in Clearance Volume with Coating Thickness....100

Figure 6-4: Cumulative Energy Distribution of BNT-Coated Pistons at Three Loads, 2000 RPM....102

Figure 6-5: Predicted Piston Surface and Porosity Temperatures....104

Figure 6-6: Piston Convective and Porosity Heat Losses....105

Figure 6-7: Coating Effects on Engine Performance....106

Figure 6-8: Piston BNT Coating Appearance Post-Testing....106

Figure 6-9: 1000μm Coating Physical Degradation at 31 mg Fueling....108

Figure 6-10: Difference in Gas Temperature, Knock Amplitude, and Combustion Efficiency at 31mg Fueling....109

Figure 6-11: Individual Effects of 230μm Coating on Heat Loss and Indicated Power at 21 mg/cycle Fueling....111

Figure 6-12: Difference in Expansion plus Porosity Heat Transfer from Un-coated Baseline....113

Figure 6-13: Difference in Indicated Piston Work from Un-coated Baseline....114

Figure 7-1: Predicted Properties and Assumptions for Highly Porous Materials....119

Figure 7-2: Effects of Sealing Layer over Hypothetical Material #1 on Surface Temperature Swing....120

Figure 7-3: Effects of Sealing Layer on Intake Heat Transfer and Surface Temp over Variable Thickness Insulation....121

Figure 7-4: Novel Insulating Coating Structure with Sealing Layer, Nickel-Coated Microspheres, and Sintered Microsphere Insulating Structure....122

Figure 7-5: Coated Intake Valves, Before and After In-Cylinder Firing Conditions.123

Figure 7-6: Experimental Results from Baseline, Insulated Intake, and Insulated Exhaust Hardware Sets....124

Figure 7-7: Valve Face Temperatures for Baseline and Insulated Engine Builds at 10 and 30mg Fueling Rates....127

List of Tables

Table 3-1: Engine Geometry 39

Table 3-2: Experimental Engine Operating Conditions 42

Table 5-1: Hypothetical Material Thermal Properties 81

Table 5-2: Analytical Engine Operating Points 86

Table 5-3: Simple Engine Geometry Wall Layers 87

Nomenclature

Nomenclature for equations and discussions throughout this document, and units that they are most commonly used in, are presented below.

A	Area [m^2]
BD1090	Burn Duration from 10% fuel energy released to 90% fuel energy released
BDC	Bottom Dead Center
BNT	Barium Neodymium Titanate, anisotropic insulating material
C	Constant [varies]
CA50	Crank Angle at which 50% of the fuel energy has been released – likewise CA10 and CA90 are the angles at which 10% and 90% of fuel energy is released [deg]
CI	Compression-Ignition
CR	Compression Ratio
c	Specific Heat Capacity [kJ/kg-°K]
DI	Direct-Injection
$depth_{1\%}$	Critical thermal depth with a material at which point the temperature swing has decayed to 1% of its surface value [m]
EGR	Exhaust Gas Residuals (i-internal, e-external) [%]
EVO, EVC	Exhaust Valve Opening, Exhaust Valve Closing
f	Frequency [Hz]
HCCI	Homogeneous Charge Compression Ignition
HRR	Heat Release Rate [J/deg]
HPSN	Hot-Pressed Silicon Nitride
h	Convection Coefficient [W/m^2-°K]
IVO, IVC	Intake Valve Opening, Intake Valve Closing

k	Thermal Conductivity [W/m-°K]
L	length [m]
LHV	Lower Heating Value of a fuel [MW/kg]
M	Molecular Mass [g/mol]
MEP	Mean Effective Pressure (leading character: B-Brake, I-Indicated, N-Net, P-Pumping) [kPa]
MFB	Mass Fraction Burned [%]
MGZ	Magnesium Zirconate
MW	Molecular Weight [g/mol]
m	Mass [kg]
n	Number of Moles [mol]
n_c	Number of Revolutions per Cycle [rev/cyc]
P	Pressure [kPa]
PSZ	Plasma-Sprayed Zirconia
Q	Heat Transfer Rate [J/s]
R	Universal Gas Constant = 8.31446 [J/°K-mol]
$\bar{\bar{R}}$	Specific Gas Constant [J/°K-kg]
Re	Reynolds Number [-]
r	Thermal Resistance [°K-m/W]
S_{eng}	Engine Speed [RPM]
SFC	Specific Fuel Consumption (leading character: B-Brake, I-Indicated, N-Net) [g/kW-hr]
SI	Spark-Ignition, Spark Ignited
T	Temperature [°K]

TBM	Thermal Barrier Material
TDC_f	Top Dead Center, firing stroke
TDC_g	Top Dead Center, gas-exchange
t	Time [s]
V	Volume [l]
VE	Volumetric Efficiency [%]
v	Velocity [m/s]
YSZ	Yttria-Stabilized Zirconia
α	Energy Closure Multiplier [-]
γ	Ratio of Specific Heat at Constant Pressure to Specific Heat at Constant Volume [-]
ε	Radiation Emissivity [-]
κ	Thermal Diffusivity [m^2/s]
ρ	Density [kg/m^3]
σ	Stefan-Boltzmann Constant = 5.67 [$W/m^2\text{-}°K^4$]
ω	Dimensionless Rotational Speed [-]

1. Introduction

1.1. General Context

There is constant pressure on the internal combustion engine as used for vehicle propulsion to convert hydrocarbon-based fuel to useful work more efficiently and with fewer harmful emissions than ever before. Increasing emissions and fuel consumption standards across the world are driving engine and vehicle manufacturers to improve overall vehicle efficiency and environmental impact as much as possible, while the competitive nature of the market ensures that solutions must be very cost-effective.

1.2. Motivation

Two of the megatrends in engine design are the moves to downsize and to downspeed light-duty engines, effectively spinning a smaller engine more slowly at a higher specific load to minimize pumping and frictional losses in everyday usage. The limits to these trends are generally related to high in-cylinder temperatures and pressures, low-load torque capacity dictated by the boosting device used, engine knock and fuel enrichment in gasoline engines, and increased emissions and high-speed load potential for diesel engines. In this environment, in-cylinder thermal management could prove to be a very important tool for further improving the efficiency and environmental friendliness of the internal combustion engine.

The objective of this study is to evaluate the impacts of the spatial location and materials properties of selectively applied in-cylinder thermal barrier materials on heat transfer, homogeneous spark-ignition combustion characteristics, exhaust energy, and engine performance. Over the range of speeds and loads encountered in passenger vehicle use, approximately 30% of the fuel energy leaves the cylinder through heat transfer to the combustion chamber walls, and another 5-10% through the exhaust port walls. This energy is transferred to the coolant at a relatively low temperature, and thus has low availability for reclamation. Preventing this energy loss from the hot combustion gasses allows the opportunity to improve the useful crank work that the gas performs directly, as well as to improve the function of devices such as turbochargers, exhaust compounding devices, and aftertreatment catalysts that rely on exhaust energy to function. The need for engine cooling drives further vehicle-level losses such as larger coolant pumps, higher coolant pressures

and flows, and larger heat exchangers with greater aerodynamic drag. In addition, thermal barriers can be used for component thermal protection to enable greater specific output and further downsizing and downspeeding efforts. Conventional insulators and novel thermal barrier materials with varying levels of porosity were investigated to determine their impact; specifically due to the effects of increasing air content on thermal conductivity and volumetric heat capacity. The motivation is to experimentally and analytically characterize a range of materials with varying levels of intra-cycle surface temperature swing to reduce the temperature differential between the gas and wall that drives heat transfer. Temperature swing properties are desirable in an in-cylinder insulation material to prevent heat loss when the combustion gasses have the potential to do the most work, while reducing the impacts of this insulation on engine breathing.

1.3. Methodology

The scope of work is centered on the combination of single-cylinder engine experimentation with thermal and thermodynamic engine modeling including the change in thermal boundary conditions throughout the engine cycle to capture the effects of temperature swing on the engine performance. Novel, low thermal conductivity and capacity materials were developed to attempt to create a large wall temperature swing on the surface of various components. Multiple hardware sets and material combinations were used to experimentally determine which heat paths out of the combustion chamber could be most effectively redirected to piston work or to the exhaust, as well as the consequences of doing so. A fast-response heat flux probe mounted in the cylinder head was used to directly measure differences in temperature and heat transfer through the head. This measurement was used with the high-speed cylinder pressure and other traditional experimental engine measurements to calibrate a 0D thermodynamic model with a simplified 2D cylinder, piston, head and valve thermal model to capture the effects of insulation and wall temperature swing properties on the engine cycle.

Together, the engine experiments and simulation results were used to better understand the interplays between engine performance and thermal environment as materials are changed. By tuning the 0D engine thermodynamic model to match the single-cylinder engine experiments, it was possible to more comprehensively assess the impact of thermal barrier materials on all heat loss paths in a consistent and comprehensive manner not possible with single location heat flux measurements. A simplified two-dimensional thermal model of the engine was developed for use with the experimental data and 0D engine simulations. The purpose of this model was to accurately predict the wall temperatures and inter-cycle temperature swing of the various materials using common spatially-averaged heat transfer correlations. Predicted wall temperatures were coupled with experimental data analysis and

engine model simulations to further understand the effects of these materials on engine performance.

Conventional thermal barrier materials were tested to evaluate the effects of currently available materials and coatings. Many of these coatings exist for component thermal protection or insulation in other environments, such as turbine engines, industrial processing and ceramics manufacturing. However, all of these environments focus strongly on steady-state insulation performance, or have much a lower thermal cycling frequency than a reciprocating internal combustion engine. Therefore, they are not developed with low heat capacity to enable fast surface temperature swings on the timescales encountered in a reciprocating engine cycle. Novel insulating materials that target very low heat capacity were conceptualized, developed and tested to measure their impact on engine performance. These materials were applied to the piston top surface, intake valve faces, and exhaust valve faces to separately evaluate their impact in different locations under the unique conditions that exist at each location.

Each hardware set was tested in a single cylinder experimental engine operated with stoichiometric spark-ignited (SI) combustion at three engine loads and two speeds covering much of a typical light-duty operating range, with combustion phasing sweeps at each point. In this way, a wide range of gas temperatures and thermal loadings were explored in order to offer greater insight into the performance of the hardware sets over the entire engine operating map. The impact of material properties and insulation locations on spark-knock and autoignition phenomenon was also assessed.

1.3.1 Literature Review Overview

In-cylinder insulation has been investigated in earnest beginning with the efforts of Cummins and TACOM to improve military diesel engine performance, smoke levels, flexible fuel capability, and to reduce cooling requirements (Kamo & Bryzik, 1978) (Bryzik & Kamo, 1983) (Sudhakar, 1984) (Hoag, Brands, & Bryzik, 1985). This work was driven by military considerations for heavy duty diesel engines used in trucks, tanks, and other armored vehicles. The primary motivation was to eliminate the cooling system from the engine, which would consequently reduce the complexity, volume and weight of the powertrain while eliminating the parasitic loss of the cooling pump. The lack of a cooling system would reduce a vehicle's vulnerability in combat situations by eliminating a large, exposed heat exchanger that is critical to operation, as well as ease maintenance and supply chain efforts. Potential improvements in efficiency and power would bring further benefits, which are magnified in a military environment due to the logistics required to supply fuel and maintenance parts. These engines were not actually adiabatic, but the goals of the

program were to reduce the net heat transfer to near zero. As such, the term "Adiabatic Engine" was applied to these efforts.

Many of the early attempts used monolithic ceramics (Woschni, Spindler, & Kolesa, 1987) (Havstad, Garwin, & Wade, 1986) such as silicon carbide (Timoney & Flynn, 1983), partially-stabilized zirconia (Morel, Fort, & Blumberg, 1985), and silicon nitride (Furuhama & Enomoto, 1987), as well as the removal of coolant (Sudhakar, 1984) and plasma-sprayed zirconia (Bryzik & Kamo, 1983). A significant reduction in heat transfer was reported by most of these sources, but any improvements in brake output required an energy recovery device in the exhaust such as a turbocharger or turbine compounding system. Naturally aspirated results generally showed no benefit to piston work; all of the energy redirected by the insulation appeared in the exhaust. Volumetric efficiency (VE) was negatively impacted by between 3 – 10% depending on the level of insulation, forcing lower load or richer in-cylinder conditions. Turbochargers could recover some of the excess energy in the exhaust to overcome the VE penalty and to provide a benefit in brake work, but that benefit was derived mostly from the pumping loop. Turbocompounding continued this trend further, allowing the recovery of more work at high loads back to the crankshaft.

Some authors (Woschni, Spindler, & Kolesa, 1987) (Furuhama & Enomoto, 1987) reported an increase in heat transfer with increased insulation during combustion and expansion, if not overall. The proposed hypothesis for this behavior was that the thermal boundary layer had shrunk with hotter walls, which allowed hotter gas closer where it could lose more heat. Other explanations were offered, such as increases in surface roughness, permeability, and changes in in-cylinder flow that increased the heat transfer coefficient or area sufficiently to overcome the insulation.

It was recognized relatively early that simply increasing the wall temperature to achieve zero net heat transfer would not result in significant engine performance gains due to the reduction in volumetric efficiency and increase in compression work. (Wallace, Way, & Vollmert, 1979) analytically investigated the difference between an isothermal wall temperature that results in no net heat transfer throughout the cycle and instantaneously adiabatic conditions, and discovered a large difference in indicated efficiency and air delivery ratio between these cases. Modeling studies derived from this analysis (Way & Wallace, 1979) highlighted the benefits of an insulating wall of sufficiently low heat capacity such that its surface temperature tracked the gas temperature throughout the cycle, approximating the instantaneously adiabatic case. This enabled large reductions in the peak heat transfer rate while allowing the wall temperature to fall with the gas temperature during the intake and compression strokes to avoid detrimentally affecting VE. Work required for compression was reduced, enabling a brake benefit even with naturally aspirated engines. Further experimental studies with air-gap-insulation (Wallace, Kao,

Alexander, Cole, & Tarabad, 1983) showed that the presence of metal mass over the air gap negated the temperature swing properties of the air gap, and emphasized the importance of the properties of the wall surface. Other researchers confirmed the same basic findings, emphasizing the importance of wall temperature swing in insulation performance (Morel, Keribar, & Blumberg, 1985) (Miyairi, 1988) (Assanis & Badillo, 1987) (Kamo, Assanis, & Bryzik, 1989).

There has been considerable recent activity to minimize heat losses and improve engine efficiency through in-cylinder temperature-swing insulation (Kosaka, et al., 2013) (Kogo, et al., 2016) (Wakisaka, et al., 2016) (Kumar & Nagarajan, 2012) (Hoffman, Lawler, Guralp, Najt, & Filipi, 2015). The capability for surface temperature swing is dictated in part by the intrinsic material properties of the material in contact with the gas. Figure 1-1 depicts the thermal properties of a variety of materials, overlaid by lines representing the surface temperature swing predicted by (Kosaka, et al., 2013). The surface temperature swing is dependent on the material properties, but is also a strong function of engine operating parameters such as load, combustion phasing, engine speed, and any others that affect the gas temperature, heat transfer coefficient, and time for heat transfer. Reductions in either the volumetric heat capacity or the thermal conductivity will result in greater levels of temperature swing.

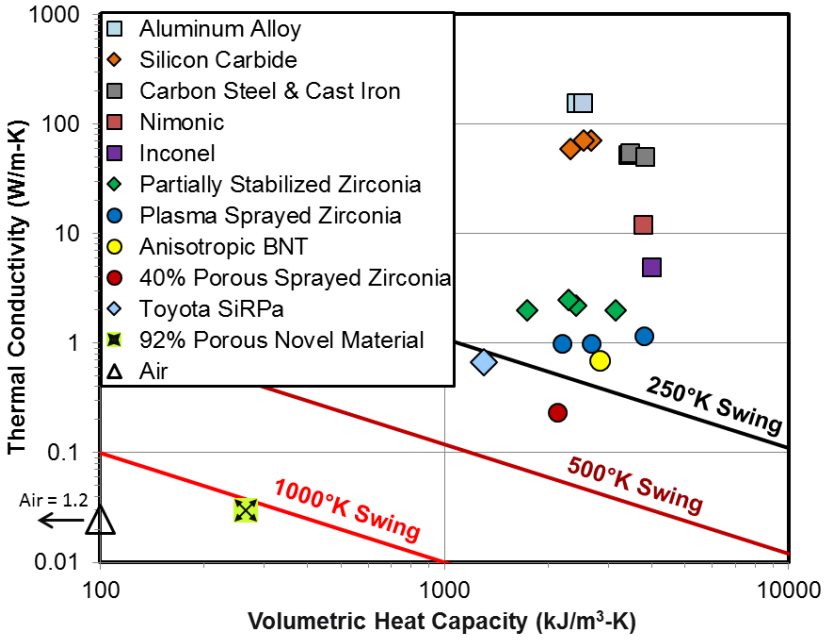

Figure 1-1: Material Thermal Properties and Estimated Temperature Swings

The relevant material properties from various references are also plotted in Figure 1-1, grouped by material type and application method. The metals typically used for engine construction as well as the bulk ceramics examined exhibit a range of thermal

conductivity over two orders of magnitude, but all have relatively similar thermal capacities. In comparison, some of the sprayed materials as well as Silica-Reinforced Porous Anodized Al (SiRPa) show a reduction in both volumetric heat capacity and conductivity, increasing the expected temperature swing through both metrics. Measurements have been taken that confirm predictions of wall temperature swing for some low-heat-capacity materials (Aoki, et al., 2015) (Fukui, et al., 2016).

$$\Delta T \sim \frac{1}{\sqrt{\rho \times c \times k}} \qquad \text{Equation 1-1}$$

In general, the surface temperature swing will be related to the material properties through the relation proposed by (Assanis & Badillo, 1987) in Equation 1-1. The volumetric heat capacity (ρ×c) of a bulk material is a function of the composition (specific heat capacity, mass basis - c), and of the density of the bulk material (ρ). The effective thermal conductivity (k) is dependent on the material structure, types of elemental bonds, and larger-scale geometric features such as the effective cross-section perpendicular to conduction and path length in the direction of conduction. A reduction in bulk density through the introduction of voids in the solid material will both directly affect the volumetric heat capacity as well as the conductivity by decreasing the cross-section of solid material. Since air has a volumetric heat capacity of approximately $1/1000^{th}$ and a thermal conductivity of $1/100^{th}$ of any of the solid materials shown, the addition of air into a bulk material through porosity can greatly improve the thermal properties necessary for temperature swing. Porosity introduced by spray application of ceramics (plasma-sprayed zirconia, anisotropic BNT) or engineered into the structure (SiRPa, Novel Materials) can have a much larger impact on both the thermal conductivity and heat capacity due to the void volume. Therefore, highly porous materials are expected to demonstrate much larger temperature swings than conventional materials.

Considerably more studies were performed on in-cylinder insulation for diesel compression-ignition (CI) engines than on spark-ignition (SI), homogeneous premixed gasoline engines for many reasons besides the military considerations mentioned previously. Fuel consumption was becoming increasingly important throughout the oil crises of 1973 and 1979, which spurred a general shift towards more efficient diesel engines for all types of transportation around the time in-cylinder insulation studies were gaining momentum. Additionally, hotter wall temperatures were expected to help CI engine fuel tolerance by reducing the ignition delay and mitigating the premixed combustion spike that results from the build-up of fuel energy in-cylinder during the early portion of the injection prior to compression-driven auto-ignition.

The push to remove tetraethyl lead (TEL) from passenger vehicle gasoline sources began in the early 1970's in the United States of America because of the negative health effects of lead on humans, the environment, and to enable the use of catalytic converters to lower harmful exhaust emissions of passenger vehicles. The removal of TEL from gasoline lowered the fuel's octane rating, which forced the reduction of SI engine compression ratios and reduced performance and fuel economy to avoid knock. Knock is generally defined as the thermally driven pre-ignition or autoignition of a premixed fuel-air mixture in-cylinder, which results in very rapid combustion accompanied by an audible pinging or rattling noise that can be mechanically destructive to the engine, breaking rings, ring-lands in pistons, and melting the pistons and valves themselves. Reducing the heat rejection of gasoline engines was expected to promote knocking due to higher in-cylinder temperatures. All of the contemporaneous methods to prevent knock resulted in lower SI engine efficiency and performance, which further encouraged the study of low heat rejection diesel CI engines over gasoline SI engines.

Homogeneous SI combustion was chosen as the combustion mode in this research for a number of reasons. First, the author deemed it was desirable to reduce or eliminate the effects of insulation on very important stratified CI combustion phenomena, such as ignition delay, diffusion flame jet impingement and mixing at the insulation material surface, and increased radiation heat transfer in comparison to SI combustion. Second, the SI combustion chamber enabled a simpler geometry for prototype insulation layers to be created on; namely the flat piston surface and flat valve faces dictated by the current method of prototype insulation construction. These surfaces together comprise over half of the combustion chamber surface area near TDC. Third, SI combustion conditions could provide a more easily survivable environment for the prototype insulation through reduced cylinder pressures and temperature gradients across the insulation surface. Fourth, there were far fewer experimental analyses of the effects of in-cylinder insulation on SI combustion phenomenon, such as auto-ignition, that are increasingly relevant to downsized, downsped engine operation encountered in the vehicle fleet in the United States.

1.3.2 Requirements for Industrialization

The greatest hurdles for industrialization of a thermal barrier coating are durability and cost/benefit analysis. Most reasonable expectations of modern powertrains is the need to last for at least 150,000 miles and 15 years, if not longer. Falling short of these requirements will result in customer dissatisfaction, a negative impact on future sales, warranty claims, and the potential for legal repercussions from government entities and private consumers. The likelihood of thermal barrier failure and the resultant increase in fuel consumption, emissions, or engine damage must be sufficiently low to meet production requirements. Additionally, the cost of including

these coatings must be weighed with respect to the performance benefits to make a sound business case for their inclusion. As a research project, the potential benefits and durability of any potential thermal barrier material must be addressed.

1.3.3 Wall Temperature Modeling

A method for accurately predicting the bulk wall temperature and surface temperature swing of the engine components in contact with gas in the combustion chamber was necessary. This model must incorporate the geometries and material properties of the engine components as well as thermal loads representative of an internal combustion engine. A finite-element implicitly solved two-dimensional model with variable element meshing, flexible geometries, temperature-dependent material properties, and inter-component heat transfer was written in MATLAB m-code for this purpose. An iterative solution was found for wall temperature, heat losses, and other engine parameters with existing thermodynamic cycle software and with experimental data analysis code. This method was used to verify the function of the MATLAB model against predictions from commercial thermal FEA software. The individual heat transfer coefficients between components and to temperature sinks were then calibrated to experimental data or literature values to allow the model to estimate the effects seen in the experimental data, and to predict the effects in hypothetical, modelled cases. The wall temperature model could be run independently or coupled with data analysis results or thermodynamic model predictions.

1.3.4 Investigation of Desired Properties

It was necessary to explore the characteristics of the thermal barrier materials that are desirable, and to define the trade-offs that could be expected. The wall temperature model was used in conjunction with a fixed in-cylinder gas temperature and heat transfer as predicted by the existing thermodynamic model. A simplistic component geometry was used to speed the solution. This analysis helped to guide further work and the selection of experimental materials and geometries.

1.3.5 Experimental and Analytic Investigations

Conventional insulating materials as well as the novel material mentioned above were experimentally evaluated in a single-cylinder research engine. The materials were used separately on the piston, intake valve faces, and exhaust valve faces to determine the individual contributions of each of these components independently. Coupled thermodynamic and thermal modeling was performed alongside these experiments to provide further insights. Insulation in the exhaust port was also investigated to determine the impacts in this location. Limited durability testing on

the prototype components was performed to help guide further development and better define the necessary material properties.

1.3.6 Novel Thermal Barrier Material Development

A novel thermal barrier with exceptionally low equivalent heat capacity and thermal conductivity was conceptualized and developed into prototype engine parts. This barrier structure incorporates over 90% by volume of semi-closed-cell porosity to achieve the desired average material properties while incorporating a sealing layer to remain impermeable to combustion gas. The very high level of porosity was necessary to achieve the effective material properties necessary to enable substantial surface temperature swing, while the sealing was integral in preventing additional heat losses. The novel thermal barrier was designed to withstand high material temperatures that it is likely to encounter in operation. Equivalent material properties were independently tested to confirm that the desired properties were being achieved, and to guide further development.

1.4. Thesis Outline

The thesis is divided into eight chapters spanning the breadth of relevant knowledge, background and foundation of the thesis topic, new results and analysis on the topic, conclusions from these unique learnings, and recommendations for future research. Considerable novel analytic and experimental results have contributed to the final results of this thesis, and further work will be guided by these learnings. The first two chapters cover the introduction and literature review, summing up the general state of knowledge at the time of thesis submission. The third and fourth chapters introduce the experimental apparatus, analysis routines, and the formulation and description of the analytical tools used. The fifth chapter establishes the potential benefits of temperature-swing coatings, investigating the sources of improvement especially in comparison to conventional insulation, and defines the requirements to achieve the benefits of temperature-swing materials without the detriments of conventional insulation. The sixth chapter delineates the experimental results using an “off-the-shelf” solution for thermal insulation, highlighting the successes and pitfalls of current technology, and helping to further refine the requirements of future novel materials. The seventh chapter outlines the process of defining the requirements, formulating a solution, producing experimental parts, and testing them for applicability to the problem. Finally, a summary of the thesis is presented.

2. Literature Review

2.1. Introduction

The balance of energy within the highly transient environment of a reciprocating internal combustion engine is dependent on many things, and thus can be very difficult to characterize and predict. Heat transfer phenomena resulting from compression, the release of combustion energy, and gas exchange have large effects on how internal combustion engines are designed and operated, and how they perform. Heat transfer between the combustion gas and the engine structure is inextricably linked to structure temperatures and combustion attributes which ultimately determine the engine's efficiency and exhaust energy characteristics.

2.2. Heat Transfer Background

Heat transfer is an energy-exchange process driven by a difference in temperature between two objects or within a single object. There are three forms of heat transfer that concern internal combustion engines: convection, conduction, and radiation. Convection is the transfer of energy between two separate bodies or fluids, characterized by Equation 2-1.

$$\boldsymbol{Q_{hot-cold} = h \times A \times (T_{hot} - T_{cold})} \qquad \textbf{Equation 2-1}$$

The area in contact between the two bodies "*A*" directly affects the heat transfer rate, as does the difference in temperature. A convection coefficient "*h*" is necessary to account for many other global and local effects such as bulk relative motion, roughness, turbulence, localized phase-changes and temperature differences from the average, and boundary layers, among others. Convection is the dominant form of heat transfer from the combustion gas to the chamber walls, piston, valve faces and liner. It also is the means through which engine components exchange thermal energy, and how the engine structure sheds that energy to the coolant, oil, and environment.

Conduction occurs due to temperature differences within a continuous material, and is described by Equation 2-2 for one-dimensional flow.

$$\boldsymbol{Q_{hot-cold} = \frac{k \times A}{d_{hot-cold}} \times (T_{hot} - T_{cold})} \qquad \textbf{Equation 2-2}$$

The thermal conductivity "*k*" is a property of the material's bond structure, elemental composition, and micro-scale geometry. "*A*" is the macro-scale cross-section through which heat can travel and "*d*" is the distance within the material between the hot and cold points. Generally, conduction is prevalent in solid materials where physical mixing is impossible such as engine structural components, or in stagnant fluid or gaseous materials with minimal mixing such as settling tanks and reservoirs.

The third type of heat transfer important to internal combustion engines is radiation heat transfer. This is the only form of heat transfer discussed herein that is not directly proportional to the difference in temperature. As shown in Equation 2-3, the difference is between the temperatures to the fourth power. Additionally, radiation is dependent on the emissivity or reflectivity of the surfaces involved, which is captured by the emissivity constant, and by the exposed area of the two bodies in consideration (view factor). Specific geometric relationships for the view factor related to soot particles and various engine components have been neglected from the basic equation below for simplicity and clarity.

$$\boldsymbol{Q_{hot-cold} = \varepsilon \times \sigma \times A \times \left(T_{hot}^4 - T_{cold}^4\right)} \qquad \textbf{Equation 2-3}$$

Due to the difference in the temperature to the fourth power, radiation only has an appreciable effect with very large temperature differences. The emissivity "ε" is a scale from 0 to 1, with a value of 1 representing the emissivity of an ideal "black-body" and 0 representing perfect reflection. "σ" is the Stefan-Boltzmann constant, and "*A*" is the limiting surface area. Radiation is most important in rich combustion zones where soot can be formed by incomplete combustion since the resulting soot will have similar temperature to the combusting mixture and is very similar to the ideal "black-body" in emissivity. Locally rich homogeneous mixtures as well as mixing-controlled combustion processes such as stratified-injection SI combustion and diesel CI will all exhibit appreciable radiation heat transfer.

The focus of the work presented herein is on homogeneous globally slightly-lean SI combustion in part to simplify the heat transfer problem, allowing the effects of radiation to be neglected. Therefore, convection from the in-cylinder gas to the combustion chamber wall, between engine components, and to thermal sinks, and conduction within components are the only forms of heat transfer considered throughout this work.

2.3. Measurement and Estimation of In-Cylinder Heat Transfer

Measurement of in-cylinder heat transfer has been attempted for over half of a century with some of the earliest work performed by (Nusselt, 1928), and developed

into the more common formulations for describing the convection coefficient between the in-cylinder gas and combustion chamber walls by (Overbye, Bennethum, Uyehara, & Myers, 1961), (Annand, 1963), (Woschni, 1967), and (Hohenberg, 1979). All of these studies relied on thermocouples capable of responding quickly enough to capture temperature variations throughout the engine cycle, mounted on the combustion chamber surface at a wide variety of locations. This necessitates thermocouple junctions with very low total thermal inertia, and therefore very low mass. Vapor deposition of a very thin metal layer, usually in an inert environment or vacuum to prevent oxidation and impurities, is typically the process used to achieve a low mass thermocouple junction. In many cases, one junction would be positioned at the surface, and a second thermocouple embedded at a known depth into an engine component or an insert that is affixed to the combustion chamber. These two thermocouples form a heat flux pair that can be used to calculate the 1-dimensional heat flux from the surface thermocouple to the embedded thermocouple, assuming that the distance and material properties between them are known.

Many varieties of heat flux probes utilize this general configuration, although the specifics of their design can vary widely. Considerable work has been spent on understanding the trade-offs in probe design and on minimizing disturbance to the thermal environment surrounding the probe (Furuhama & Enomoto, 1987) (Assanis & Badillo, 1989). In general, heat flux is primarily one-dimensional perpendicular to the combustion chamber surface within the first few millimeters of wall thickness, so closely clustered thermocouples at varying depths from the surface can safely assume that heat flows one-dimensionally. The thermocouple junction must be very thin to minimize its mass in order to respond to the wall's temperature swing, but must have a relatively large cross-sectional area across the surface to allow heat to bleed off of the junction into the surrounding material and prevent undue influence of the thermocouple element material properties on the resulting measurement. Similarly, the element wires themselves must be very thin to minimize their thermal inertia to avoid biasing the measurement and local thermal environment. The surrounding material must be very similar to the material of the component that the probe is inserted in to mimic the un-modified conditions that would exist at the probe location.

The time-averaged heat flux can be easily calculated from the average of the two temperatures, but this value lacks the resolution to identify specific heat transfer trends with different portions of the cycle. The transient heat flux throughout the cycle requires the solution of the unsteady 1-dimensional heat transfer equation as proposed by (Alkidas, 1980) using a Fourier series for solution of the derivative. Once the heat flux is calculated and both the gas and wall temperatures are known, formulations for the heat transfer coefficient can be proposed.

The convection coefficient is highly dependent upon the gas velocity and turbulence near the walls, and most correlations rely on combinations of the Nusselt or Reynolds numbers to represent these conditions on a global level. The seminal work by Woschni on in-cylinder convection (Woschni, 1967) forms the basis for most modeling efforts due to its formulation primarily from first principles and relative simplicity to apply to experimental data and modeling results. It is a globally averaged model which uses the mean gas temperature and pressure to evaluate the convection coefficient through assumptions about how gas properties and velocities vary with pressure and temperature. Many other formulations (Nusselt, 1928) (Annand, 1963) (Hohenberg, 1979) follow similar reasoning. A basic relationship between the Reynolds and Nusselt numbers was used in those references to derive the basic form of the convection coefficient in terms of physical parameters from a measured or modeled engine, shown in Equation 2-4.

$$\boldsymbol{h = C \times L_{char}^{m-1} \times P^{m} \times v_{gas}^{m} \times T^{0.75-1.62m}} \qquad \textbf{Equation 2-4}$$

In this equation, "*L*" is the characteristic length and is generally taken as the cylinder bore, "*P*" and "*T*" are the instantaneous bulk gas pressure and temperature, respectively, and v_{gas} is the average gas speed at the wall. "*C*" is a fitting constant used to adjust predictions to match experimental data. "*m*" is an exponential constant relating the Nusselt and Reynolds numbers, and is generally taken to be approximately 0.8. Other sources provide justification for varying the exponents independently based on experimental evidence (Hohenberg, 1979). The gas velocity term is further broken down and estimated according to Equation 2-5.

$$\boldsymbol{v_{gas} = C_1 \times \overline{v}_{piston} + C_2 \times \frac{V_{displ}}{V_{IVC}} \times \frac{P - P_{motor}}{P_{IVC}} \times T_{IVC} + C_3 \times \omega_{swirl}} \qquad \textbf{Equation 2-5}$$

As can be seen in the equation, the average gas speed term has three components to it. The first is due exclusively to the mean piston speed driving compression, expansion, and gas exchange. The second term captures the pressure amplification due to combustion over the motoring compression pressure, and represents the velocity imparted by the flame compressing the unburned mixture and traversing the combustion chamber. The third term, proposed in a subsequent publication (Sihling & Woschni, 1979), captures the bulk rotational gas velocity imparted by the intake port design. The coefficients "C_1" and "C_3" were proposed to have higher values during the gas exchange than the closed-cycle revolutions to account for the intake and exhaust flow velocities and how they decay during compression. For the present research, the closed-cycle constants were adopted for the entire cycle to avoid discontinuities in heat transfer due to the switching, and the global convection coefficient multiplier was adjusted to account for this change.

The above equations and reasoning provide a solid foundation for the prediction of heat transfer within an engine, but many other factors can have a significant effect. In-cylinder heat transfer is a fairly delicate balance, dependent on gas and wall temperatures, in-cylinder flows, and anything else that could affect the thermal boundary layer. In fact, multiple authors attributed a reduction in the thermal boundary layer due to elevated wall temperatures to a measured increase in heat transfer over an uninsulated wall (Woschni, Spindler, & Kolesa, 1987) (Furuhama & Enomoto, 1987), although this increase could be due to increased surface roughness, permeable porosity losses, or simply experimental error. However, autoignition in the form of combustion knock or intentional HCCI both affect the formation and thickness of the boundary layer, and thus heat transfer. Both of these phenomena will be discussed in greater depth in the next section. In general, intentional HCCI is aimed at low-load operation where autoignition rates can be controlled and a high-temperature flame-front is avoided, which reduces heat transfer due to the reduction in peak burned gas temperatures and combustion-induced velocities (Chang, et al., 2004). Unintentional autoignition, such as spark-knock, occurs at high load and is incited by conventional spark-ignited flame propagation. Therefore, most of the conventional heat loss mechanisms are in play in addition to unburned gas autoignition near the cylinder walls and the sonic ringing that it induces, which combine to destroy the thermal boundary layer and increase heat transfer losses by 50 to 400%, depending on severity and measurement technique (Rassweiler & Withrow, 1935) (Lu, Ezekoye, Iiyama, & Greif, 1989) (Syrimis, Shigahara, & Assanis, 1996) (Mutzke, Scott, Stone, & Williams, 2016).

On a finer scale, even the roughness of in-cylinder surfaces can influence the heat transfer through a number of mechanisms. Increased roughness does increase the surface area on a microscopic scale, which directly impacts the overall heat transfer. Greater roughness will also increase the turbulence near the surface in the presence of bulk gas flows such as tumble or swirl, which effectively increases the local gas velocity and therefore reduces the thermal boundary layer through elevated mixing levels. Finally, increased roughness can result in more unburned fuel adhesion to the surface through spray impingement and inertia-induced separation. These effects are noted in different finishes on metallic engine components (Tsutsumi, Nomura, & Nakamura, 1990), and in permeable porous surfaces such as combustion chamber deposits (Anderson & Prakash, 1985) or thermal barrier materials (Assanis, Wiese, Schwarz, & Bryzik, 1991) (Wakisaka, et al., 2016).

2.4. Spark-Ignited Combustion Background

SI combustion is defined as a mode of combustion where a flammable mixture of fuel and air is prepared around the spark plug. Electrical discharge from the spark plug is used to ignite a portion of the mixture, and flame propagation is used to consume the

rest of the fuel throughout the combustion chamber. Homogeneous SI is achieved through pre-mixing of the fuel and air prior to entering the combustion chamber, as achieved by carburetors or port-fuel-injection. A close approximation to homogeneous SI can also be achieved with direct-fuel-injection systems that deliver fuel into the combustion chamber directly, through fuel injection timing, fuel rail pressure, and injector design to maximize vaporization and mixing. The intent is to evenly distribute the fuel and air to create a consistent mixture throughout the entire combustion chamber. Alternatively, stratified SI combustion aims to create a carefully controlled gradient of fuel concentration throughout the combustion chamber. Generally, this is done to provide a richer, more easily ignitable and energy dense mixture around the spark plug at the time of ignition while maintaining an overall lean mixture in the rest of the combustion chamber for improved fuel efficiency through a reduction in intake throttling and compression/expansion gas properties. This can be achieved through precise control of direct-fuel-injection and fuel spray targeting (Zhao, 2002) (Ando, 2009) (Fansler, 2015), or through separate fuel and air mixing channels within a pre-chamber such as the Honda CVCC design and the Mahle Jet Ignition concept (Bunce & Blaxill, 2016), among others. This body of work will focus on homogeneous SI combustion, achieved through direct injection coinciding with the intake stroke during the period of fastest piston motion.

Conventional SI combustion is generally understood as having four primary stages, as thoroughly documented and analyzed by many authors (Rassweiler & Withrow, 1935) (Rassweiler & Withrow, 1938) (Nakanishi, Hirano, Inoue, & Ohigashi, 1975) (Nakamura, et al., 1978) (zur Loye & Bracco, 1987) (Bozza, Gimelli, Merola, & Vaglieco, 2005) and subsequently consolidated by (Heywood, 1988) and others. It must be recognized that the body of knowledge necessary to draw our current understanding of these processes is much more vast than can be cited here, and the specific references presented are ones that the author found particularly helpful. The four stages are ignition & kernel development, laminar flame expansion, turbulent combustion, and wall-quenching. Each of these will be discussed individually with emphasis on the role that heat transfer can play. Additionally, abnormal and desirable autoignition as seen in SI engines, manifested by knock and HCCI respectively, will be discussed.

The first stage of SI combustion is the ignition event and flame kernel development. Once a combustible mixture of vaporized fuel and air is inducted into the cylinder and compressed by the piston, the ignition system discharges stored energy through the spark plug and a plasma channel between the cathode and anode briefly forms. This spark plasma ignites the mixture within the spark gap, forming a small flame kernel that attempts to begin propagating outwards. Exothermic energy from combustion in the flame kernel must be enough to overcome heat losses to the spark plug electrodes, body, cylinder head and surrounding gas; otherwise the flame will quench,

resulting in a misfire. Practically, for a given fuel with set activation energy and lower heating value, this means that the in-cylinder conditions at the time of spark must support a laminar flame speed high enough to consume sufficient fuel to counter heat loss to the spark plug and engine structure. The addition of excess air or exhaust gas residual (EGR) dilution, or ignition timing that results in a spark discharge into a low pressure, low temperature mixture, are a few examples that could result in insufficient laminar flame speed and thus misfire. Bulk mixture motion can, to a certain extent, assist in flame kernel growth by bringing more unburned mixture into contact with the kernel. Too much mixture motion can work to quench the flame kernel, as not enough energy is released to surpass the activation energy of large masses of combustible mixture that get forced into the kernel (Nakamura, et al., 1978). The flame kernel and early development tends to be the stage of combustion responsible for most of the natural cycle-to-cycle variation in individual combustion events, as small differences in flow structure, temperature, and mixture concentration around the spark plug can have large effects on the rate at which the kernel grows (Nakanishi, Hirano, Inoue, & Ohigashi, 1975). Subsequently, these differences carry through to the rest of the combustion event, especially once the piston reverses direction and begins expanding the mixture, cooling the bulk temperature.

As the flame kernel grows, it transitions to the laminar development stage of combustion. At this second stage, consumption of unburned mixture is roughly equivalent to the rate at which a laminar flame would propagate in still conditions. Generally, this stage occurs at the time at which between 1% and 6-10% of the combustible mass within the cylinder has burned (Mass Fraction Burned – MFB), and before the flame radius has grown enough that flame wrinkling can significantly contribute to the unburned mass consumption rate. At this point, the flame exists within one turbulent eddy, or spans only a small group of eddies. Factors affecting the laminar flame speed have a large effect at this stage, as does bulk mixture motion such as swirl or tumble that can help to spread the flame kernel and bring more unburned mass into contact with the flame (Nakamura, et al., 1978). The flame is generally strong enough at this point that it is unlikely to be overwhelmed by in-cylinder gas motion, and has grown to the point where heat losses to the spark plug and cylinder head represent a very small fraction of the energy released by combustion. It is possible therefore for increased in-cylinder flow to delay early spark kernel development stage, yet speed the laminar and subsequent stages for a net reduction in combustion duration, especially during the period between 10% and 90% MFB (Nakanishi, Hirano, Inoue, & Ohigashi, 1975).

The effects of turbulence dominate the rate at which a flame consumes unburned mass in an SI engine beyond approximately 10% MFB. At this point, the flame diameter surpasses the integral turbulent length scale (representative of an average

eddy size) and turbulent velocities begin to spread the burning mass through the combustion chamber from eddy to eddy more quickly than the laminar velocity can. The laminar velocity still dictates the rate at which mass within individual eddies is consumed, but the flame front is propagated outwards from the source of ignition through mass transfer driven by turbulent velocities along the edges of eddies. As the flame grows considerably beyond the integral length scale and continues to envelop eddies, this visually manifests itself as a "wrinkling" of the flame front. The wrinkling increases the flame front area, resulting in a multiplicative enhancement of the unburned mass consumption rate. Therefore, the turbulent burning velocity is typically expressed as a function of the laminar flame speed, and is dependent on all of the variables that affect the laminar flame speed. Increased turbulence, as encountered with greater in-cylinder flow and increased engine speed, will increase the effective turbulent flame speed and thus total burning velocity (zur Loye & Bracco, 1987).

Ultimately, as the flame front reaches the edge of the combustion chamber, the available unburned mixture is limited, and wall effects slow and then stop the burning rate. The relatively cold surface of the combustion chamber and the thermal gradient induced in the gas are contacted by the wrinkled flame gradually, and force the turbulent flame to "de-wrinkle" while slowing the laminar flame speed due to lower gas temperature. Throughout most of the combustion chamber, the flame will die out at the wall quickly as unburned fuel is depleted and heat losses to the wall increase. In corners or narrow sections of the combustion chamber such as between the piston and bore over the top sealing ring or in squish regions near TDC, heat losses to the wall can be sufficient to quench the flame before it can consume the fuel left in these corners and crevices, leading to unburned hydrocarbon emissions.

As combustion is occurring, the pressure, temperature, and number of molecules per unit mass are all changing. Generally, the combustion chamber is small enough that the pressure equilibrates quickly enough that it can be assumed to be constant throughout the volume. Some very large industrial engines can experience significant pressure gradients as the engine bore is large enough and the engine speed slow enough that pressure waves traveling at the speed of sound will introduce measurement errors on a crank-angle basis. These effects are negligible in engines used for personal or commercial road transportation. Likewise, the speed at which compression occurs via combustion or volume changes is much slower than the speed of sound for normal combustion modes, and thus pressure differences across the chamber can be ignored under these conditions. The gas temperature after combustion is on the order of 2000°K hotter than the temperature of the unburned gas, which induces a large density gradient across the combustion chamber. This will force the unburned gas away from the spark plug and towards the combustion chamber wall while compressing it and heating it through compression. These are the

processes that can lead to unintentional autoignition, otherwise known as knocking due to the characteristic rapping, ringing sound that is produced through acoustic excitation of the engine structure.

Autoignition in the most pure form is a chemical process that occurs when a flammable mixture is heated, even without a source of ignition such as the spark plug. Essentially, the larger hydrocarbon molecules will begin to decompose at elevated temperatures, producing smaller hydrocarbons and radicals that promote further reactions. Once a critical concentration of radicals is achieved, bulk reaction of the fuel and air can commence, resulting in a very sudden combustion without a centralized location. Typically this is described by taking the integral of an Arrhenius equation describing fuel reaction rate over time, such that the temperature history of the unburned gas is captured (Livengood & Wu, 1955), or by solving reduced sets of chemical equilibrium equations at each timestep of an engine simulation (Hu & Keck, 1987). Temperature and fuel concentration gradients will introduce a smearing factor to the autoignition behavior, resulting in a cascading heat release that is slower than pure autoignition but still faster than typical flame propagation (Najt & Foster, 1983).

Unintended autoignition (knock) can occur in the unburned fuel-air mixture in SI engines, especially when the unburned gas is further heated by high fueling rates, large amounts of hot exhaust residual gas or partially reacted hydrocarbons from the previous cycle, a high geometric compression ratio, and hot intake air or cylinder walls. Knock typically defines a limit on compression ratio and specific output especially at low speeds where the piston dwells near TDC for longer, providing more time for autoignition. Due to the break-down of thermal gradients near the walls, heat transfer increases by between 50% and 400% with the occurrence and severity of knock (Rassweiler & Withrow, 1935) (Lu, Ezekoye, Iiyama, & Greif, 1989) (Syrimis, Shigahara, & Assanis, 1996) (Mutzke, Scott, Stone, & Williams, 2016), further heating the walls near the end-gas and encouraging knock in subsequent cycles. In this way engine knock can quickly get more severe, resulting in physical damage to engine components due to the high pressures and high wall temperatures induced. Unintended autoignition of the end-gas due to pressure and temperature effects causing distributed regions that reach the point of combustion form the most common type of abnormal combustion typically described as knock. Other forms, such as pre-ignition from an unintended ignition source such as lubricating oil and combustion chamber deposits, or destructive detonation wherein a strong pressure wave creates local compression, driving combustion at sonic speeds, also fall under the general description of “knock”, but will not be treated in this work (McKenzie & Cheng, 2016).

Traditionally, in-cylinder insulation has been expected to hurt an engine's knocking behavior because of increased wall temperatures. Increased intake air temperatures and coolant temperatures both have a detrimental effect on the combustion phasing at which knock occurs (Imaoka, Shouji, Inoue, & Noda, 2016) (Brussovansky, Heywood, & Keck, 1992). Despite this, some studies have shown no difference (Assanis & Mathur, 1990) or a performance benefit (Nakic, Assanis, & White, 1994) when using in-cylinder thermal insulation.

One of the main contributions to the thermal environment of the end-gas that promotes knock are combustion chamber deposits, which form over portions of the chamber surface and act as a semi-porous insulating layer, where it acts to heat the unburned end-gas during combustion, promoting knock. Additionally, the permeable porosity of deposits can act to store partially burned hydrocarbons from one cycle to the next where they can act to initiate knock in the end gas (Brussovansky, Heywood, & Keck, 1992). These deposits are the result of hydrocarbons from a variety of sources accumulating over many cycles. They can be formed by any of the mechanisms that can generate soot, rich combustion byproducts, incomplete combustion of lubrication oil from the bore wall, as well as through the precipitation of unburned hydrocarbons to the relatively cold combustion chamber walls as the flame approaches the walls, cools and quenches. The source of the deposit and temperature of the wall upon which it forms both have a large impact on the resulting deposit morphology, thermal and physical properties (Choate & Edwards, 1993) (Kalghatgi, Combustion Chamber Deposits in Spark-Ignition Engines: A Literature Review, 1995) (Kalghatgi, An Experimental Study of Combustion Chamber Deposits and Their Effects in a Spark-Ignition Engine, 1995). The measured thermal properties of combustion chamber deposits can be similar to plasma-sprayed zirconia coatings, and would enable them to experience some degree of surface temperature swing throughout the engine cycle (Anderson & Prakash, 1985).

Eventually, deposit accumulation slows and thickness stabilizes due to increased temperatures at the surface of the deposit that balance the precipitation and burn-off rates (Wood & Anderson, 1993). It has been shown that increased wall temperature through insulating coatings can prevent deposit build-up if the surface temperature stays above approximately 320°C, which actually improved the engine's knock performance as well (Nakic, Assanis, & White, 1994). Despite the insulating properties of deposits, they often will not reduce heat transfer as significantly as expected due to their permeable porosity, which acts to increase the surface area and decrease the thermal boundary layer within the porosity (LaVigne, Anderson, & Prakash, 1986).

Autoignition can be intentionally incited in an internal combustion engine as well. Compression-ignition (CI), or "Diesel" combustion, essentially begins as chemical

autoignition, with the rate controlled by a very steep fuel concentration gradient induced by mixing of the injected fuel when the piston is near TDC after compression. Fuel injection rate, timing, vaporization and mixing are the dominant processes that control the rate at which combustion occurs, since the fuel requires some oxygen in the compressed air to react with. Typically, as fuel is injected into a hot, high-pressure environment, the first packets of fuel will mix and heat until they reach their point of autoignition, creating a flame which propagates along the fuel jet as a function of injection rate and the speed at which air is entrained in the fuel spray (Heywood, 1988).

In the context of homogeneous SI engines, intentional autoignition is of interest as a way of enabling lean combustion to remove throttling losses and improve the gas mixture's thermodynamic compression and expansion properties without creating large quantities of oxides of nitrogen that typically accompany lean flame-propagation throughout a homogeneous mixture. (Onishi, Jo, Shoda, Do, & Kato, 1979) (Najt & Foster, 1983) (Thring, 1989). This form of combustion is generally known as homogeneous charge compression ignition (HCCI), with practical variants that involve some form of flame propagation to initiate autoignition such as spark-assisted compression ignition (SACI) or partially-premixed charge compression ignition (PCCI).

HCCI and its variants all rely on a sensitive, chemically and thermally driven process in the unburned compressed fuel-air mixture to provide an appropriately phased and duration-controlled combustion event, despite the wide variety of factors that could influence the mixture concentration and thermal environment (Dec & Sjoberg, 2003). The engine's coolant temperature, and by extension the combustion chamber wall and inlet port temperatures, have a large impact the in-cylinder thermal stratification that affects HCCI combustion phasing (Sjoberg, Dec, Babajimopoulos, & Assanis, 2004) (Chang, Lavoie, Babajimopoulos, Filipi, & Assanis, 2007). By extension, the combustion chamber surface temperature, including deposits and thermal history, also play a large, variable role in HCCI combustion, since their effects will change based on the operating history of the engine and the wall's thermal inertia and deposit formation or erosion (Guralp, et al., 2006) (Hoffman, Lawler, Guralp, Najt, & Filipi, 2015). In-cylinder insulation with low thermal inertia and high surface temperature during combustion and expansion could potentially help to mitigate these effects by quickly responding to changes in engine speed and load, masking the underlying metal's thermal inertia, as well as preventing deposit formation on the insulated surfaces.

2.5. Conventional Insulation in Literature

Some of the earliest modeling of the performance of the low heat rejection heavy duty diesel engine was conducted by (Kamo & Bryzik, 1978) as a part of the Cummins/TACOM Adiabatic Engine program. This simulation utilized glass ceramic properties as insulation applied to in-cylinder components. Insulating all in-cylinder surfaces and the exhaust ports had the potential to reduce heat rejection from the gas to the combustion chamber walls by 79%. The naturally aspirated model showed minimal BSFC improvement over the conventional engine since it had no path to recover thermal energy redirected from the engine structure to the exhaust, but suffered a 20% reduction in peak power due to worse volumetric efficiency. A turbocharged, aftercooled variant of the model was able to maintain peak output and improve BSFC after adding insulation by 3% due to better turbocharger efficiency which provided higher intake pressure from lower exhaust manifold pressure, improving engine pumping. Turbocompounding the turbocharged engine further improved the respective improvement with insulation due to greater utilization of the energy redirected into the exhaust. Peak power improved by 15% while BSFC improved by 8%. Adding a Rankine cycle to the turbocharged or turbocompounded engine made further improvements due to even greater exhaust energy utilization.

Further work by (Bryzik & Kamo, 1983) tested a prototype of the heavy-duty adiabatic turbocharged and turbocompounded diesel engine in a 5-ton truck, and demonstrated a peak thermal efficiency of 48% for the engine alone. This engine used conventional iron heads, liners, and pistons which had their combustion-chamber surfaces coated with plasma-sprayed zirconia (PSZ). PSZ demonstrated the temperature capability, thermal conductivity, strength, and coefficient of thermal expansion (CTE) necessary to achieve the target of 70% reduction in heat rejection. Simulations showed that the PSZ would increase the average wall temperature over iron by approximately 33°C for every 0.5mm of coating thickness, and increase the maximum temperature swing from 28°C for iron to almost 85°C for any of the PSZ coating thicknesses. The adiabatic engine's high thermal efficiency combined with the improvements in aerodynamics and weight reduction gained by removing the cooling system produced approximately 50% lower fuel consumption than the original vehicle over 3000 miles of on-road testing with no mechanical failures. Work was continuing on monolithic zirconia inserts for the pistons and cylinder heads, as well as friction reduction techniques to overcome the difficulties of using traditional lubricating oils with extremely high wall temperatures.

Experimental results by (Sudhakar, 1984) and (Moore & Hoehne, 1986) further supported the Cummins program by comparing engine data between a cooled engine and the same engine with coolant drained and water pump removed. An improvement in brake efficiency of 1.7% due to reduced heat losses was observed,

and an additional 0.7% due to removal of the water pump and 1% due to changes in combustion from hotter walls. Volumetric efficiency suffered by 3%. The addition of a 1.25mm plasma-sprayed zirconia coating on the piston top surface (Moore & Hoehne, 1986) actually hurt brake efficiency by approximately 2%. Less heat was rejected to the coolant and oil with the insulated pistons, and volumetric efficiency was reduced by 1.5%. It was suspected that a reduction in clearance volume and inconsistent sprayed thickness contributed to the loss of efficiency for the piston. Insulation of the cylinder heads had very little impact on engine performance or heat load distribution. This is not unexpected due to the small percentage of cylinder head area exposed to the combustion chamber; additionally the uncoated exhaust ports and valve faces still provided a large heat transfer path from the gas to the coolant in the head.

(Hoag, Brands, & Bryzik, 1985) continued the Cummins/TACOM adiabatic engine program with more detailed modeling efforts. They added insulation in stages and selectively varied the heat transfer during different parts of the cycle to understand the effects on engine operation in order to better match analytical and experimental results. Insulation slightly increased the work required by compression but had little effect on the work provided by expansion, leading to a slight loss in the gross indicated energy. Most of the improvements from reduced heat rejection were achieved in the pumping loop, where the turbocharger was forced to deliver the same air mass but at higher intake pressure due to reduced volumetric efficiency. At fixed turbocharger efficiency, the exhaust pressure did not have to increase because the exhaust temperature was higher, leading to the pumping improvement. Turbo-compounding increased these benefits on a brake basis directly by delivering the extracted energy back to the crankshaft.

Finite-element heat transfer models of the piston and cylinder liner were built to study their effects on engine performance. Re-introducing cooling to just the liner recovered almost half of the lost volumetric efficiency and further improved BSFC by 1% while minimally impacting the exhaust temperature. This result was in agreement with other work by (Morel, Keribar, Blumberg, & Fort, 1986), (Wade, Havstad, Ounsted, Trinkler, & Garwin, 1984), and others, but would require keeping a cooling system for the engine, which was not desired. Surface temperatures of the liner near the top ring with a fully insulated engine reached almost 560°C at the modelled condition, which is significantly higher than could be tolerated by available lubricants. Removal of the liner insulation reduces the temperature to a peak of 390°C, which is closer to the cooled temperature of 170°C but could still be problematic.

(Frame, 1983) experimentally evaluated many conventional and specially-formulated lubricant oils for use in the TACOM Adiabatic Engine program. The testing

was performed using a single cylinder engine with an iron liner that could be run without cooling, or with heating elements active to control the wall temperature within the range expected for the adiabatic engine. The engine was run for 49 hours with each formulation, or until failure or significant oil consumption or degradation occurred. Over 30 formulations were tested, but none of them performed acceptably. In general, the failure modes were oxidation which thickened the oil to the point of pump starvation and created corrosive products in the lube, volatility which increased consumption & oil thickening, and engine deposits which caused ring sticking and poor sealing. In order to use conventional piston rotating assembly lubrication techniques, it was concluded that the liner and piston-side surface temperatures need to remain similar to those encountered in fully-cooled engines.

The possibility of omitting lubrication for the piston-bore interface through the use of silicon carbide (SiC) was investigated by (Timoney & Flynn, 1983). Silicon carbide was chosen due to its high-temperature strength and low coefficient of thermal expansion, although it has very high thermal conductivity in comparison to many other monolithic ceramics. Firing tests showed that refined SiC piston and liner designs had very low friction and no detectable blow-by in the opposed-piston, 2-stroke diesel configuration tested, despite requiring no lubrication. Friction levels with the SiC piston and SiC liner were comparable to those of just the engine rotating assembly without pistons installed. Further work by (Flynn & MacBeth, 1986) showed that the friction of the unlubricated SiC piston and liner was approximately half that of the conventional lubricated metal piston, rings, and liner. Piston seizing and ceramic fracturing presented many difficulties throughout testing.

Many others from major industrial and educational institutions were involved in the simulation and experimentation of low heat rejection engines in the same vein as the papers discussed above outside of the TACOM/Cummins Adiabatic Engine program. (Yoshimitsu, Toyama, Sato, & Yamaguchi, 1982) and (Toyama, Yoshimitsu, Nishiyama, Shimauchi, & Nakagaki, 1983) modeled, developed monolithic ceramic, air-gap insulated, and ceramic spray insulated parts for, and experimentally verified performance improvements in large six-cylinder turbocharged and turbo-compounded diesel engines. Their modeling predicted approximately 7% improvement for a turbocharged engine and up to 20% for a turbocharged and turbo-compounded engine, with another 1% improvement for removal of the cooling fan & related accessories. Experimentally, they encountered combustion problems in the insulated engine that initially limited performance improvements. Further improvements to the engine insulation, turbocharger, compounding turbine and geartrain resulted in an 11% improvement in brake efficiency over the cooled engine due to insulation and turbomachine improvements alone, with an additional 2% brake improvement due to friction reduction from higher temperature, lower viscosity oil, and 2% improvement due to removal of the engine cooling system.

Ceramic coatings for wear and scuffing on the cylinder liner were necessary, and ceramic coatings for insulation of the piston and other components were preferred over monolithic blocks due to structural integrity concerns of large ceramic monoliths. Lubrication issues were still present, as excessive bore wear and top ring carbon buildups were still noted in testing.

(Wallace, Way, & Vollmert, 1979) analytically investigated the difference between an isothermal wall temperature high enough to eliminate net heat transfer over the cycle and instantaneously adiabatic conditions, and discovered a large difference in indicated efficiency and air delivery ratio between these cases. While the adiabatic assumption was clearly unrealistic, the exercise demonstrated the difference between adjusting the instantaneous heat transfer coefficient (to 0 in this case) versus increasing the steady wall temperature to accomplish the same net goals. The isothermal condition showed no significant improvement in thermal efficiency with a large detriment in volumetric efficiency, while the adiabatic condition showed up to 15% improvement in thermal efficiency and volumetric efficiency similar to the un-insulated baseline condition. Continuing this reasoning further, a variety of insulation methods were investigated in an attempt to deviate from the isothermal condition to promote large swings in wall temperature. The insulation methods included bulk silicon nitride, which represented a typical monolithic ceramic exhibiting lower thermal conductivity, as well as two idealized insulating structures. The silicon nitride showed a reduction in heat transfer of approximately 50% without a significant increase in thermal efficiency, and was still essentially isothermal with respect to the gas temperature. The first idealized structure consisted of a highly conducting, infinitely thin surface layer suspended over a stagnant air gap, intended to represent a honeycomb-style or other air-gap-insulated, minimally supported mechanical structure. This structure exhibited surface temperature swings very similar to the gas temperature, and therefore approximated the adiabatic condition. The second idealized structure consisted of a 0.01 mm copper sheet laid over a perfect insulator, in an effort to evaluate the surface layer effects on the air-gap insulation concept. This analysis showed that while the net heat transfer was eliminated, the heat capacity of this very thin copper wall was high enough to damp out most of the temperature swing effects and negate the thermal efficiency benefits. Further improvements from any form of insulation were seen when turbocompounding was added to the engine (Way & Wallace, 1979).

Insulation through a designed air gap in the piston crown was further explored by (Wallace, Kao, Alexander, Cole, & Tarabad, 1983) experimentally and analytically. The experimental findings showed substantial redirection of energy to the exhaust and a significant reduction in volumetric efficiency for a single-cylinder naturally aspirated diesel test engine. Further simulation, including compounding studies, show benefits of 2 – 6% improvement in brake efficiency for turbocharged, 6 – 12% for

turbocharged and turbo-compounded engines, and up to 15% for two-stroke engines. At a given intake pressure, the volumetric efficiency was reduced by almost 20%. It was emphasized that improvements in performance of highly insulated engines rely heavily on efficient turbomachinery (Wallace, Kao, Tarabad, Alexander, & Cole, 1984).

(Siegla & Amann, 1984) performed simulations of the performance of a smaller, passenger-car-based indirect-injection diesel engine with thermal insulation. This study included part-load simulations to better cover the range of operation of engines in passenger vehicles and to take advantage of the proportionally higher heat losses at lower brake loads. They found that there were no performance benefits with insulation to a naturally aspirated engine, as the lower volumetric efficiency caused richer operation at a given load. The richer operation extended the combustion duration, negatively impacting thermal efficiency. In addition, the lower volumetric efficiency reduced the maximum load when naturally aspirated, which would necessitate a larger engine to meet the same performance targets and therefore would increase the friction losses at all loads.

(Cole & Alkidas, 1985) at General Motors Research experimented with an air-gap insulated piston in a specially designed indirect-injection single cylinder diesel engine with separate instrumentation for the pre-chamber and main chamber, as well as separate cooling paths for the pre-chamber, intake side of the head, exhaust side of the head, and the liner. Heat rejection rates measured at each cooling path showed up to a 17% decrease in heat rejected through the liner accompanied by a slight increase in the heat rejected through the exhaust port, for a total of 7% heat loss reduction with the insulated piston. VE was noted to have declined by only 2%, while BSFC improved slightly at light loads. This improvement was likely due to slightly improved combustion efficiency, seen by the reduction in unburned hydrocarbons and carbon monoxide at these lean air-fuel ratios.

Monolithic ceramic inserts for the piston bowl, head surface, and liner above the top ring reversal for a direct-injection diesel engine were investigated by (Havstad, Garwin, & Wade, 1986) for Ford Research. Large amounts of analysis was devoted to the structurally sound design of ceramic components captured and held in compression by aluminum and iron castings for durability. Experimental evaluation revealed that monolithic ceramic inserts reduced heat losses by 25%, compared to 20% for plasma-sprayed insulation. This reduction in heat loss resulted in up to a 9.1% improvement in ISFC for the monolithic inserts and a 7.4% improvement for the sprayed components. These improvements were noted at low loads and speeds, with diminishing returns as speed and load increased.

Investigations at Volkswagen by (Walzer, Heinrich, & Langer, 1985) showed minimal efficiency or thermal performance benefits in a small diesel engine with ceramic

components in-cylinder. This work was more focused on thermal protection and reduced cooling in specific parts of the engine. They noted that cold-start performance did improve through a reduction in the ignition delay due to faster piston bowl surface heating. The use of ceramics was also investigated for wear on sliding valvetrain parts, for mass reduction and high-temperature strength for a turbine rotor, and as a diesel particulate filter medium.

(Morel, Fort, & Blumberg, 1985) conducted a thorough analytical evaluation of the effects of insulation on the performance of a large commercial turbocharged and turbocompounded diesel engine. The engine structure was modeled with a thermal network that included heat transfer separately from the burned and unburned gas zones to the wall through convection and radiation, conduction between engine components, heat addition due to friction, and intra-cycle wall temperature calculation to capture the various heat transfer paths of energy from the gas to the coolant and oil. Insulation was sequentially added to various engine components in the order in which they contributed to the total heat transfer until the entire combustion chamber was covered in a layer of bulk partially-stabilized zirconia (PSZ). The piston was responsible for approximately half of the un-insulated baseline heat loss, and insulation of the piston produced more than half of the total improvement in thermal efficiency and exhaust temperature, as well as half of the reduction in heat transfer and volumetric efficiency that would be seen by full chamber insulation. Notably, insulation of the liner did not show any improvement in brake efficiency as only a small fraction of the liner was exposed during the period of greatest heat transfer. Instead, liner insulation served to primarily redirect heat flows from the coolant to the oil by preventing the piston from losing as much heat to the liner. Similarly, insulating the valve heads did not show any improvement since their primary heat loss path was through the valve seats to the cylinder head, which had already increased in temperature due to its own insulation.

One of the earliest modeling studies on the effects of reduced heat transfer on SI operation was performed by (Watts & Heywood, 1980). This study used a prescribed heat release rate, so increases in wall temperature did not affect the combustion process, however they would affect the thermal and volumetric efficiency predictions. The wall temperature was solved in a steady-state manner, so swings in surface temperature throughout the cycle were not comprehended. Due to the limitations mentioned, this study did not differ much from the previous diesel studies, and it showed similar reductions in volumetric efficiency and minimal thermal efficiency improvement for a naturally aspirated engine. In fact, since peak output was reduced, friction was a larger percentage of the losses, and brake efficiency actually declined.

Experimental work with thin-film, fast response thermocouples was performed by (Furuhama & Enomoto, 1987) to evaluate the effects of ceramic piston inserts in both

gasoline and diesel engines over conventional aluminum pistons. Insulation was applied in the form of a 4.5mm hot-pressed silicon nitride (HPSN) disk affixed to the top of a shorter piston with a 0.3mm air gap between them. The air gap was included to provide an additional thermal resistance and allow the temperature of the HPSN disk to rise considerably over that of the aluminum. The HPSN average surface temperature was measured to be 200°C hotter than the aluminum, with a temperature fluctuation throughout the cycle of 48°C vs. 9°C for the aluminum. Surprisingly, despite the higher surface temperatures, the calculated peak instantaneous heat loss and entire heat loss during the combustion and expansion stroke was measured to be higher with the HSPN piston insert, while the gross average heat loss was reduced by roughly 50% through the piston. The authors attribute this to a dependence of the convective heat transfer coefficient on the wall temperature as well as the gas temperature. The HPSN insert piston did show a greater amount of heat transfer from the wall back to the gas during exhaust, intake and compression befitting its higher surface temperature. Overall, the net averaged heat loss throughout the cycle for the HPSN piston insert was roughly 50% of that for the aluminum piston. Similar experiments were performed on a diesel engine with aluminum pistons, with an HPSN insert in the bottom of the bowl and a sintered silicon nitride disk affixed to the piston top. These results also showed an increase in the peak and average heat loss during the combustion and expansion stroke, but a lower cycle-averaged heat loss calculated by the thermocouples due to negative heat flow from the walls to the gas during the other three strokes. However, the magnitude of the differences when adding insulation were considerably less than for the gasoline engine. The authors hypothesized that the heat transfer boundary layer becomes thinner when the wall temperature is increased, which actually allows combustion to occur closer to the wall where it can drive a greater amount of heat transfer despite the higher wall temperature. This stands in stark contrast to previous modeling and experimental results performed by others.

(Woschni, Spindler, & Kolesa, 1987) experienced similar results to Furuhama when experimenting with an air-gap insulated piston in a direct-injected diesel engine. The effective thermal conductivity of the Nimonic 80A shell and air gap was calculated to be equivalent to a 5mm thick layer of ZrO_2. This increased the measured surface temperature by up to 400°C when compared to an aluminum piston at the same load. Heat release analysis showed that the net heat release profile is largely the same shape for both pistons, but cumulatively added to approximately 5% less energy by the end of the cycle. This difference was attributed to an increase in heat transfer despite the hotter wall for the same reasons as stated above: that the heat transfer boundary layer shrunk and combustion occurred closer to the wall, which increased the coefficient of convection. This hypothesis was tested by varying the temperature of a fast-response thermocouple by regulating the cooling air provided to it. The rate of temperature rise during combustion was considerably higher when the surface

temperature of the probe was at 750°C instead of 380°C, which was calculated to be a 300% increase in the peak convective heat transfer coefficient. Due to this increase, BSFC increased by 6%. Further simulation was performed using a modified heat transfer coefficient equation that captured the effects seen in experiments. A turbocharged, turbocompounded diesel engine showed a significant detriment to BSFC at high load and low speed, with a small improvement to BSFC at low loads due to the excess air and resulting cooler surface temperatures.

Hydrocarbons, CO, and particulate emissions in the exhaust were all noted to be the same or lower in insulated diesel engines by many authors (Bryzik & Kamo, 1983) (Sudhakar, 1984) (Toyama, Yoshimitsu, Nishiyama, Shimauchi, & Nakagaki, 1983) (Walzer, Heinrich, & Langer, 1985) (Cole & Alkidas, 1985) (Assanis, Wiese, Schwarz, & Bryzik, 1991). The largest contributors to HC and CO emissions are the relatively cool crevice volumes and over-lean areas of the combustion chamber. As the wall temperatures increase, the crevice volumes will be warmer, which will make them less dense and incapable of "protecting" as much unburned mass from the main combustion event to be released later. The unburned and global in-cylinder temperatures increase with the wall temperature as well, which will minimize lean quenching in the overly lean areas of the chamber. In-cylinder insulation has been shown to reduce HC and CO emissions considerably depending on the way in which changes in combustion were compensated for, in different engines with varying levels of insulation and operating conditions.

The formation of soot and particulates in diesel engines is largely controlled by the mixing process and thermal environment. Since the ignition delay of diesel combustion is shortened as temperature increases, the fuel does not have time to mix as thoroughly prior to combustion, leading to a greater stratification of the local air-fuel ratio. Greater fuel mass combusting at richer-than-stoichiometric local conditions will produce greater amounts of soot. However if the global gas temperature is warmer throughout expansion, then the soot has more time to oxidize in-cylinder before quenching which could lead to lower net soot emissions at EVO. Many low-heat-rejection engine experiments were performed with considerably hotter liner temperatures than the lubricating oil could tolerate, resulting in increased oil consumption through reduced viscosity and in-cylinder vaporization. Higher oil consumption will directly have a large impact on soot emissions, especially because the piston does not expose much of the liner until later in the cycle when gas temperatures have fallen. Literature reveals a spread in the analytical and experimental trends concerning soot and in-cylinder insulation. (Siegla & Amann, 1984) predicted an increase in soot emissions with lower heat rejection, possibly due to increased soot formation rates that are not countered by increased oxidation later in the cycle. It is conceivable that the separation into a relatively richer, hotter prechamber and cooler, higher oxygen content main chamber in Siegla's simulations

biased the net soot balance towards the generation mechanism, while soot oxidation was relatively suppressed by lower main chamber temperatures. Experimental measurements by (Bryzik & Kamo, 1983) and (Toyama, Yoshimitsu, Nishiyama, Shimauchi, & Nakagaki, 1983) showed a large reduction in particulates, which could be in contrast to Siegla's predictions due to the larger, direct-injection diesels containing a single undivided combustion chamber. After re-optimization of combustion in a heavy duty diesel engine, (Serrano, Arnau, Martin, Hernandez, & Lombard, 2015) demonstrated that insulation of the piston surface or exhaust manifold could reduce soot and either NO_x or fuel consumption, but not both simultaneously. (Assanis, Wiese, Schwarz, & Bryzik, 1991) showed small changes to soot and particulates in an SI engine in either direction, indicating that the effects of insulation on soot formation and oxidation was a balance that could easily be skewed in either direction by specifics in engine design, insulation, and combustion.

The findings concerning NO_x emissions were more mixed. In general, due to the high-temperature formation kinetics of NO and NO_2, higher in-cylinder temperatures would be expected to produce greater amounts of total NO_x. The insulated chamber's shorter ignition delay could also result in less fuel penetration and poorer air utilization, which could cause fuel and temperature stratification leading to higher peak temperatures and thus greater NO_x formation. However, shorter ignition delay will result in a greater percentage of the fuel mass consumed by diffusion burning which typically produces less NO_x due to the lower combustion temperatures in lean regions with an excess of oxygen, but hotter temperatures in rich regions where NO_x is prevented from forming due to a lack of oxygen. Many of these factors are highly dependent on injector and chamber design and the resulting fuel-air mixing, making broad trends in literature unclear. (Bryzik & Kamo, 1983) found that the NO_x generated at a specific injection timing did increase, but the BSFC vs NO_x tradeoff improved due to the reduction in ignition delay and rate of improvement in BSFC from turbocompounding. These findings were further confirmed throughout the TACOM/Cummins adiabatic engine program (Sudhakar, 1984). (Siegla & Amann, 1984) speculated that the higher heat transfer due to compression of the air into the prechamber in their study would exacerbate the formation of NO_x more than in the quiescent, direct-injection combustion chamber used in most heavy duty diesels, which was confirmed by an increase in NO measured with a pre-chamber diesel (Cole & Alkidas, 1985). (Morel, Fort, & Blumberg, 1985) and (Morel, Keribar, Blumberg, & Fort, 1986) predicted small increases in NO_x with insulation, despite utilizing a direct-injection combustion system.

The effects of radiation heat transfer in diesel engines is also of importance when analyzing low heat rejection engine designs that attempt to reduce the convective heat transfer through reduced difference in gas and wall temperature. Radiation from an object is dependent on the object's temperature to the fourth power, emissivity

coefficient, and surface area, while net radiation (including reverse from the surroundings to the object) also comprehends the surrounding temperature to the fourth power. This basic relationship is shown in Equation 2-3. Radiation is strongest from soot and other combustion particulates that resemble "black bodies", which have an emissivity coefficient close to unity. (Siegla & Amann, 1984) note radiation becomes much more prominent in insulated engines, up to 25% of the total heat loss from 10%. They state that hotter wall temperatures will not have an impact on radiation, which for practical purposes is true since the radiation from the gas to the walls is only dependent on gas temperature. Radiation from the walls back to the gas will increase, but the amount is negligible at realistic wall temperatures in comparison to the gas temperature. (Morel, Fort, & Blumberg, 1985) calculate that in a "superinsulated" engine with effectively no net convective heat transfer, the only net source of heat transfer from gas to wall is radiation, supplemented by friction energy from the sliding piston. In comparison, radiation in Morel's baseline uninsulated engine accounted for 17% of the total heat transfer.

The general trends of 0-5% efficiency gains in modelling results for naturally aspirated and turbocharged engines, 5-10% efficiency gains for compounded engines, and 5-10% reduction in volumetric efficiency were echoed by numerous other authors (Thring, 1986) (Dickey, 1989) (Cheng, Wong, & Gao, 1989) (Shabir, Authars, Ganesan, Karthik, & Madhan, 2010). Experimental results rarely showed as much benefit, if any, in efficiency due to a variety of reasons. Some authors showed increases in heat losses with insulation, whether due to increased surface area and roughness with a coating (Wakisaka, et al., 2016), or potentially because of a dependence of the convection coefficient on the wall temperature as well (Furuhama & Enomoto, 1987), physically manifested as a thinner thermal boundary layer between the hot core of the gas and the wall (Woschni, Spindler, & Kolesa, 1987). In many cases, combustion was altered through richer operation, changes in heat release timing and rate, and heat losses not captured by the modeling. Permeability effects could have factored into the experimental results, increasing heat losses and potentially increasing surface wetting by the fuel, further affecting combustion (Serrano, Arnau, Martin, Hernandez, & Lombard, 2015). Not all of these effects could be countered through re-optimization of combustion to account for insulation.

2.6. Temperature-Swing Insulation in Literature

By the late 1980s, a consensus seemed to be forming that the cyclical swing in wall temperature needed to be considered when discussing the potential for in-cylinder insulation to increase performance in internal combustion engines. This consideration is necessary especially in materials that contain low volumetric heat capacity which would allow fast changes in temperature, and low thermal conductivity which would enable a reduction in overall heat transfer and an increase

in surface temperature during combustion and expansion. In both analytical (Wallace, Way, & Vollmert, 1979) (Morel, Fort, & Blumberg, 1985) (Anderson & Prakash, 1985) (Kosaka, et al., 2013) and experimental (Furuhama & Enomoto, 1987) (Harder & Anderson, 1988) (Aoki, et al., 2015) (Kawaguchi, et al., 2016) studies, a non-negligible swing in surface temperature throughout the engine cycle was observed with increasing insulation. This poses unique possibilities and challenges over the concept of a steady, elevated temperature and was fundamentally different from the net-zero heat transfer model with respect to the processes occurring in-cylinder.

The investigation by (Wallace, Way, & Vollmert, 1979) described previously had calculated wall temperate swings for a variety of insulation structures. A concept for an air-gap-insulated structure designed to allow the wall temperature to closely track the gas temperature was simulated in ideal form, and it was hypothesized that this would effectively enable true adiabatic operation with minimal instantaneous heat transfer at any point in the cycle. Simulation showed that true adiabatic operation could result in up to a 10% indicated thermal efficiency improvement, while operation with isothermal walls and reduced net heat transfer did not give any improvement to indicated efficiency.

Further analysis of the effects of temperature swing phenomena were performed by (Morel, Fort, & Blumberg, 1985), in which a “superinsulated” engine was modeled with sufficiently low thermal conductivity that the net heat transfer out of the gas was essentially zero. It was noted that this was different than a thermodynamically adiabatic state, as there was still instantaneous heat transfer between the gas and walls; only the integrated heat transfer over the cycle was zero. When the heat generated by friction was included in the wall temperature calculation, the total net heat transfer from the walls to the gas was actually negative. The concept of “pumped heat” was introduced by these authors in another paper (Morel, Keribar, & Blumberg, 1985), which referred to thermal energy that is “pumped” into the chamber walls and stored there during periods of high heat transfer. This thermal energy is later released when the gas temperature drops below the wall temperature, which occurs for most of the cycle in the “superinsulated” engine. This “pumped heat” can still be a loss mechanism even though the energy is ultimately returned to the gas, as it removes energy from the gas at the time when it can do the most work, such as during combustion near TDC prior to the bulk of expansion, and reintroduces it to the gas when it can do less work, such as at the end of expansion or during the intake stroke. To demonstrate the difference in “pumped heat” with similar thermal resistance, the engine was modeled with plasma-sprayed zirconia (noted as ZPS in the source, to differentiate from “partially-stabilized zirconia”, but referred to as “PSZ” within this document) with approximately ¼ the thermal conductivity, ¼ the thickness, and ½ the volumetric heat capacity of the bulk partially-stabilized zirconia mentioned previously. Despite equal thermal resistance, the PSZ rejected slightly less heat and

had slightly lower thermal efficiency due to less "pumped heat" which resulted in a greater wall temperature swing throughout the cycle when compared to the bulk zirconia. The PSZ had approximately 120°C higher maximum wall temperature during combustion, which kept some additional thermal energy in the gas where it could perform indicated work during the expansion stroke. Accordingly, the time-averaged wall temperature for PSZ was 20°C lower, which reduced heat transfer from the walls back to the gas during the rest of the cycle. When the PSZ is compared to the "superinsulated" engine, the PSZ prevents approximately 50% of the heat transfer while improving thermal efficiency over the "superinsulated" engine by 60%, demonstrating a more efficient use of the redirected energy.

Continued work by (Morel, Keribar, Blumberg, & Fort, 1986) focused on the effects of insulation on a heavy-duty turbocharged diesel engine across multiple speeds, loads, and engine configurations. In general, intercooling and minimal liner insulation is much more desirable from a power and emissions perspective, while omitting the intercooler and thoroughly insulating the liner produces slightly more efficiency and reduces the ignition delay but at the expense of volumetric efficiency and power potential. Rankine cycle bottoming and turbocompounding both improve the total benefits of insulation over turbocharging, in addition to the heat recovery benefits they provide over the conventionally cooled engine. A smaller turbocharged DI diesel engine for automotive use was investigated as well. This automotive engine had higher in-cylinder air motion and a higher surface-to-volume ratio, both of which will increase heat losses from the gas to the coolant over the large, more quiescent heavy duty DI diesel engine. Accordingly, the percentage improvement in thermal efficiency with insulation of the automotive engine was approximately double that of the heavy duty engine, while the reduction in volumetric efficiency approximately doubled as well. In the automotive engine, liner insulation did not provide any efficiency increase; it only hurt the volumetric efficiency and thus power potential. The heavy duty turbocharged and intercooled engine was predicted to have brake efficiency improvements from insulation alone of approximately 5% over the baseline, while the automotive turbocharged and intercooled engine benefitted from insulation by 10 – 12% over baseline.

The concept of "pumped heat" was further refined into the Retained Heat Conversion Efficiency (RHCE), which is the difference in brake thermal efficiency of the insulated engine and the cooled engine divided by the difference in heat transfer energy between the insulated and cooled engine. Predictably, a turbocompounded turbocharged engine will have a higher RHCE than a turbocharged engine since the turbocompounding device offers greater opportunity to extract the energy preserved by insulation from the hot exhaust gas. Differences between Morel's results and those of previous studies were analyzed and said to be dependent primarily on differences in the heat transfer and wall temperature models used.

(Morel, Keribar, & Blumberg, 1985) analytically varied both the thermal conductivity and volumetric heat capacity plot of a hypothetical insulating material. This study found that thermal conductivity was the primary driver for reduced net heat transfer, but lower heat capacity increased the temperature swing throughout the cycle, and thus reduced the "pumped heat". The surface temperature is able to swing more when the heat capacity is lower because a given amount of energy will raise the surface temperature more, as the surface has lower thermal inertia. When the surface temperature swings to a greater extent, it more closely follows the gas temperature, decreasing the driver for convective heat transfer and preventing more heat loss near TDC when the additional energy has the opportunity to do more work because more of the expansion stroke remains to extract it. Contrarily, a high, constant wall temperature may prevent just as much net heat transfer over the cycle, but since the temperature is constant instead of swinging, greater instantaneous heat transfer will occur during combustion near TDC. That energy will be stored in the walls during the expansion stroke and returned to the gas once the gas temperature has dropped in the exhaust and intake strokes. The returned energy is less useful during these strokes since no expansion remains to extract that energy. It was found that greater "pumped heat" through greater wall temperature swing mitigated the reduction in volumetric efficiency & improved the thermal efficiency of the engine due to the timing of heat loss as described above. However, higher temperature swings would increase the thermal stress and fatigue in the surface material and cause higher peak temperatures which could lead to problems with component strength and melting, as well as exacerbate the existing lubrication problems in low heat rejection engines. Similar results finding that increased temperature swing improved the heat rejection/engine efficiency trade-off without the severe effects on engine breathing were confirmed through separate investigations by a variety of sources (Miyairi, 1988) (Assanis & Badillo, 1987) (Assanis & Mathur, 1990). The importance of keeping the coatings thin to allow a controlled amount of heat loss from the coating backside was identified as necessary to allow the wall temperature to drop to the level of the uninsulated wall during the intake stroke to avoid a volumetric efficiency detriment (Kamo, Assanis, & Bryzik, 1989) (Wong, Bauer, Kamo, Bryzik, & Reid, 1995).

More recent investigations into the potential of temperature-swing materials to reduce heat transfer and improve efficiency have been conducted by (Kosaka, et al., 2013) at Toyota Research & Development. They analytically swept a wide range of intrinsic material thermal properties, and evaluated two hypothetical materials with heat capacities of 0.3 and 0.1 W/m-K and thermal conductivities of 800 and 100 kJ/m^3-K, respectively, in greater depth. Kosaka found that at coating thicknesses of up to 100μm, the net heat transfer can be reduced by up to 8% with a 2% indicated efficiency improvement for the higher set of properties. The lower set of properties resulted in a 22% reduction in heat transfer for a total indicated efficiency improvement of 4.5%, both with no detriment to intake air heating. Both of these

materials exhibited enough temperature swing to allow the reduction in heat transfer while still dropping below the un-insulated wall temperature during the intake stroke, eliminating the historical insulation trade-off. Thicker coatings did not enable greater temperature swing, since the swing only permeates into the coating a specific distance dictated by the frequency of the driving heat transfer and the thermal properties of the material. Any additional material thickness will increase the total heat insulation through conduction, but this only has the effect of increasing the average surface temperature of the coating, not the swing, to the detriment of the volumetric efficiency. Further reductions in heat capacity and thermal conductivity will increase the temperature swing and improve overall performance. Kosaka et. al. surmised that large amounts of trapped porosity must be included in the material to drive down the density and volumetric heat capacity. Structures composed of hollow spheres in a zirconia binder were tested and showed a much faster temperature response to a cooling air jet, although the environment and timescale that this was tested in was not very similar to an internal combustion engine.

The application of various temperature-swing materials to in-cylinder experimental components was performed by (Wakisaka, et al., 2016) at Toyota. A material comprised of hollow glass bubbles in a ceramic binder was tested on the piston and showed a reduction in heat transfer of 10% during initial tests, but degradation over time was attributed to thermal damage. An alternate thermal barrier material comprised of a porous specially anodized aluminum was also tested in open-pore and silica-sealed forms, called SiRPA (Silica-Reinforced Porous Anodized aluminum). The open-pore material reduced heat transfer by 5%, with an additional 3% reduction from sealing the pores with silica. The sealing layer prevented intrusion into the pores by the hot gas, which reduces the effectiveness and increases the surface area of the coating. The surface temperature swing was measured using laser-induced phosphorescence, and had increased significantly over the metal walls. Negative interactions between the coating surface roughness and fuel spray were found in the diesel bowl area where fuel sprays interacted with the bowl wall, which led to the adoption of the coating on the squish-region of the piston only. This application led to a brake efficiency improvement in a production engine of 1.9% (Kogo, et al., 2016). Wall temperature swing for the SiRPA material and a surface with similar thermal properties was measured through various techniques, and found to be in the 200 - 250°C range for the operating conditions (Fukui, et al., 2016). The effective convection coefficient was found to stay the same despite the wall temperature swing due to an increase in the gas kinematic viscosity but a decreased turbulent velocity near the wall, resulting in similar levels of molecular dissipation and heat transfer, which preserves the thermal boundary layer near the wall (Aoki, et al., 2015).

The use of thermal barrier materials to promote wall temperature swing in an HCCI engine environment have been investigated by (Hoffman, 2012) (Hoffman, Lawler,

Guralp, Najt, & Filipi, 2015) (Powell, O'Donnell, Hoffman, & Filipi, 2016) (O'Donnell, Powell, Hoffman, Jordan, & Filipi, 2016). Application of a magnesium zirconate (MGZ) or yttria-stabilized zirconia (YSZ) coating to the piston top surface advanced the HCCI combustion phasing, which increased combustion efficiency and lowered unburned hydrocarbon and CO levels, resulting in a benefit to gross indicated thermal efficiency. The advanced combustion phasing enabled by the use of in-cylinder insulation accounted for some of the performance benefits that otherwise would not have been possible without additional heating of the intake. When combustion phasing was held constant with cooled EGR, reduced benefits in combustion and thermal efficiency were observed due purely to the altered thermal environment and reduction in heat loss due to the coating. For the MGZ coatings, appreciable porosity was measured through line-of-sight radiation heat flux for thin coatings, and was noted to increase the fuel pooling in HCCI operation within the piston bowl, which led to greater mixture stratification and extended combustion duration.

3. Experimental Apparatus and Methods

3.1. Introduction

Experimental testing included material property measurement outside of the engine, and performance of the materials when installed into a single-cylinder research engine. Measurement of the relevant thermal material properties was necessary to verify manufacturer claims or simulated predictions, especially with unique materials. Engine testing was performed to evaluate the material performance and impact on engine efficiency, breathing, combustion and heat losses. A description of the processing routines used for analysis of heat release rate, observed heat losses, and heat flux from a fast-response thermocouple pair from experimental data is also included.

3.2. Material Properties Measurement

It is critical to measure the thermal properties of the materials in use to predict their temperatures and performance in the engine. The thermal diffusivity and heat capacity of insulating materials used in experimental testing were measured using the following techniques. Measurements were taken over the range of 50 to 300°C to evaluate the trends with temperature, and repeated at least 3 times to ensure reproducibility and build confidence in the measurements.

3.2.1 Thermal Diffusivity

The thermal diffusivity of the materials tested were measured using a TPS 2500S thermal constants analyzer according to ISO/DIS 22007-2.2 standards. Diffusivity was measured over the range of 50 to 300°C at 50°C increments to give a better indication of the performance of materials over a range of temperatures. A hot-disk sensor was used, which is a <0.5 mm thin spiral integrated sensor and heating element that is inserted between two identical samples and clamped in place to ensure consistent heat transfer between the sensor and the

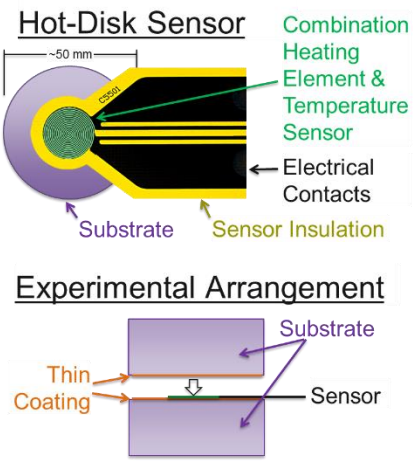

Figure 3-1: Thermal Diffusivity Measurement Technique

samples. When prototype materials and coatings were measured, multiple combinations of individual samples were measured to determine good average values of diffusivity, and to evaluate the spread of diffusivity between different individual samples.

The sensor itself is comprised of an integrated heating coil and a highly accurate thermistor positioned at the center of two substrates held or clamped together. The heating coil is used to deliver a known amount of thermal energy to the sample, and the rate of temperature rise at the thermistor is recorded. The rate of temperature rise and delay between heating and temperature rise are used to calculate the diffusivity of the sample. Calibration against known pure samples is used to account for the conductivity of the sensor itself, and other effects related to manufacturing and testing variability.

This technique can be used for solid materials and for thin films, using different sets of assumptions. In a solid material, the assumption is that the energy is conducted away from the heating element into the substrates uniformly in all directions. Thin film testing, used for coatings applied over a substrate, calculates the properties of the thin coating while compensating for the change in thermal diffusivity as the heating energy reaches the solid substrate. To perform this compensation, the diffusivity of the substrate and the thickness of the coating must be known for accurate results. The substrate must also be thick enough that the heat does not encounter the uncoated side before it reaches the sensor in the center. This technique and the assumption for thin coatings are only valid for isotropic materials, at least on the scale of 1-2mm or the distance between the heating coil and the sensor element.

3.2.2 Heat Capacity

The heat capacity (c) was measured independently of the diffusivity (κ) using differential scanning calorimetry for the material samples in order to calculate the thermal conductivity (k) individually according to Equation 3-1. An STA 449 F1 Jupiter calorimeter was used to provide these measurements at 50°C increments from 50 to 300°C. This measurement records the difference in heat flows between the sample and a known reference as a function of temperature, at each temperature point, to calculate the heat capacity of the sample in accordance with ASTM E1269-11.

$$\boldsymbol{\kappa = \frac{k}{\rho \times c}} \qquad \textbf{Equation 3-1}$$

3.3. Experimental Engine and Test Facilities

The experiments performed in this work were carried out in a direct-injected single cylinder gasoline engine with a geometry and piston top surface as shown in Table 3-1. The first build of the engine had a combustion chamber geometry shown in Figure 3-2 similar to production designs, including a contoured piston top designed to work with the pent-roof head, spark plug and centrally located gasoline direct injector locations. This build was used to test conventional, commercially available thermal barrier materials in preparation for the novel materials being developed.

Table 3-1: Engine Geometry

	First Build	Second Build
Bore	86 mm	86 mm
Stroke	94.6 mm	94.6 mm
Comp. Ratio	12.0	11.0
Piston Top Surface	Contoured	Flat
Intake Duration	260°	260°
Exhaust Duration	230°	230°

The second build of the engine was predominantly the same as the first build, but with the adoption of a flat-top piston (not shown). This was done to facilitate the production of prototype parts with the novel thermal barrier materials. The compression ratio was reduced due to the change in piston shape; the rest of the combustion chamber and engine geometry was unchanged.

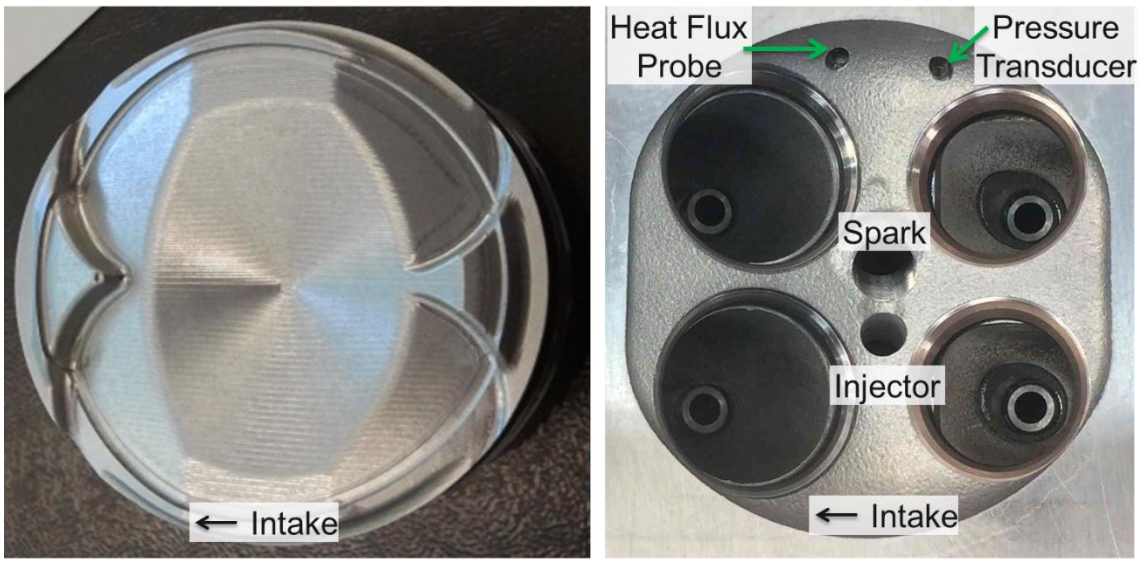

Figure 3-2: Combustion Chamber Schematic for Single-Cylinder Experimental Engine (Contoured Piston)

The total trapped mass, and especially the fuel mass, must be accurately tracked to arrive at sensible conclusions. Precise control of the intake air was achieved through the use of a critical air supply system, which consists of a number of calibrated orifices and a regulated, high-pressure manifold that achieves choked (critical) flow through the orifices. Since the gas volumetric velocity through a choked orifice is constant, mass flow is regulated by changing the upstream pressure to increase the gas density. Multiple orifices are employed and switched between to allow control over a wide range of flows given a limited supply pressure and the need for the flow to remain critical. The air supplied to this system was dried, and the air temperature in the intake manifold was controlled with immersion and tank skin heaters. Exhaust pressure was maintained through a backpressure valve and PID controller for constant boundary conditions to the engine.

Fuel volumetric flow was measured directly and simultaneously with both a Max Machinery and a Pierburg high-precision piston flow meter of differing designs to provide redundancy and confidence in the measurements. Fuel density was calculated at both meters using the nominal density and the fuel temperature at each meter. For some tests, the density at one of the meters was directly measured to provide confidence in the corrected values. The measured fuel mass flow rate was calculated from the volumetric flow rate and the density for each meter, and compared to the fuel mass estimated from various air-fuel ratios and the air mass flow rate. Air-fuel ratio is calculated using both a carbon-balance and an oxygen-balance from the measured exhaust concentrations of unburned hydrocarbons, CO, CO_2, O_2, and oxides of nitrogen (NO_x) (Stivender, 1971) (General Motors Engine Test Code Committee, 1994). Additionally, the air-fuel ratio is estimated using a wide-range exhaust O2 sensor produced by NGK, Bosch and others for use in production vehicles.

Fuel was supplied to the engine through a direct injector of production design, supplied by a high-pressure production-style fuel pump with precise control over the fuel pressure and temperature in the range of 12 – 20 MPa. Fuel was always injected during the middle of the intake stroke around the period of maximum piston speed starting at 290° $bTDC_f$ to provide a homogeneous mixture, so effects due to the details of the fuel injector spray pattern, penetration, and mixing were minimized. The fuel itself was a tightly controlled research fuel designed to replicate a 10% ethanol blended gasoline with 87 average octane rating. Full-authority control over the fuel injection timing and duration, as well as the spark timing, spark dwell, and cam phasing, was provided by a custom set-point controller.

Exhaust gas emissions were measured by a Horiba MEXA-series bench, with separate analyzers for unburned hydrocarbons, carbon monoxide in multiple ranges, carbon dioxide, and oxides of nitrogen. Species in the exhaust can continue to react, and can

fall out of suspension in the exhaust gas between the time at which the exhaust valve is opened and when they are sampled by the emissions analyzers. However, reactions tend to be accelerated at higher temperatures and pressures, so the drop in pressure and temperature upon entering the exhaust will slow reaction rates. Additionally, cold wall temperatures of the exhaust system will encourage larger molecules like hydrocarbon chains to condense on the walls and not reach the emissions analyzers, skewing the results. As a precaution, temperatures along the exhaust system were monitored and emissions sampling lines were heated to mitigate hydrocarbon condensation. Smoke numbers were recorded for all points to attempt to minimize sources of radiation and improve the homogeneity of the fuel distribution with an AVL 415S smoke meter. The average of three smoke meter readings was taken as the measurement.

Low-speed data, such as temperatures from most thermocouples, intake and exhaust pressures, flow rates, and other parameters that are expected to be steady over the course of a steady-state operating point, were recorded continuously at a rate of approximately 2 hz. A 30-second average was taken and stored for all of the low-speed parameters at each point, and the standard deviation was recorded for certain measurements such as the fuel flow rates to ensure that there wasn't significant variation over the measurement period. High-speed data was taken from the crank angle encoder, in-cylinder pressure transducer, and the heat flux probe at every $1/10^{th}$ crank angle degree. For most data points, this was down-sampled to every 1 crank angle degree in analysis to decrease processing time and storage space of the results. The pressure transducer used was a Kistler 6125A with a flame shield to minimize thermal shock, and the heat flux probe was of the MedTherm fast-response vapor-deposited junction, coaxial design discussed in greater detail below. It was mounted in the periphery of the cylinder head between the intake and exhaust valves, flush with the cylinder head surface. Heat flux measurements were primarily used to ensure that the measured heat flux was predominantly the same between different hardware configurations; no attempt was made to compare the measured and predicted heat fluxes due to the spacial averaging that is implicit in Woschni's correlations, but which does not occur in the single point measurement of the heat flux probe.

3.4. Experimental Methodology

Ensuring the accuracy and precision of the recorded data is paramount to producing trustworthy results, especially when potential differences are slight. Therefore, motoring and firing control points were taken every time the engine spun up from rest, and a motoring control point was taken at the conclusion of each individual variable sweep. These points were constantly monitored to ensure that the engine and all instrumentation was operating correctly and repeatably, and any unexpected

deviations were immediately investigated, providing data integrity and reducing time wasted. Additionally, because these investigations required the engine to be disassembled and reassembled for the hardware to be changed, baseline hardware configurations were repeated regularly throughout testing at logical intervals. This gave assurance that the engine performance was repeatable, and allowed an assessment of the variability due to slight differences in tolerances, timings, and alignments that result from rebuilding the engine.

The experimental testing presented herein consists of a set of ignition timing sweeps recorded at three load points at 2000 RPM, shown in Table 3-2. These load points are defined by the fueling rates of 10, 20, and 30 mg/cycle, which aligned with roughly 3 bar, 6 bar, and 9 bar IMEP to evenly cover the operation of a naturally aspirated SI engine. This range of loads is lower than some used in the analytical investigations, primarily because the experimental testing on the single-cylinder engine is limited in load due to material thermal constraints of the piston and exhaust valves. Testing of options for additional component cooling would not have been possible in the time available for experimentation. Due to a calculation error, the actual fueling rate used in the experiments with the conventional insulating materials study was approximately 5% higher than the target fueling. This error was corrected prior to recording the data for the novel insulating materials, resulting in a slight disparity in the fueling rate between these datasets. However, comparisons between these independent sets of data are minimized, so the analysis and conclusions are not compromised. Fuel injection timing for each load was adjusted to minimize the smoke number (less than 0.05 was deemed acceptable), limited to the range in which the intake valve was open, in an effort to find the point of best mixing. This was performed with the 1000 µm BNT-coated piston, as this component had the highest measured smoke numbers. Each set of experimental measurements was repeated on a hardware set until repeatability or hardware degradation was confirmed.

Table 3-2: Experimental Engine Operating Conditions

Fueling Rate	10 mg/cycle	20 mg/cycle	30 mg/cycle
Fuel Injection Timing	290° $bTDC_f$	220° $bTDC_f$	250° $bTDC_f$
Fuel Injection Pressure	20 MPa	20 MPa	20 MPa
Engine Speed	2000 RPM	2000 RPM	2000 RPM
Intake Pressure	47 kPa	79 kPa	95 kPa
Exhaust Pressure	100 kPa	100 kPa	100 kPa
Exhaust Air/Fuel Ratio	15.5:1	15.5:1	15.5:1
Target CA50	2.5° $aTDC_f$	8.5° $aTDC_f$	19.0° $aTDC_f$
Approx. Spark Timing	46° $bTDC_f$	26° $bTDC_f$	13° $bTDC_f$
Approx. IMEP	3.3 bar	6.6 bar	9.3 bar
Approx. NMEP	2.7 bar	6.4 bar	9.2 bar

3.5. Experimental Data Analysis

It is critical when working with experimental data to be intimately familiar with the data analysis techniques, models, and assumptions made to arrive at a result. The details of the data analysis programs used throughout the generation of the results presented herein are described below.

3.5.1 Initial Calculations

The technique for measuring the in-cylinder pressure requires the continuous integration of very small amounts of electrical charge, and is therefore highly susceptible to any slight electrical losses and noise in the wiring between the pressure transducer and the amplifier. Additionally, thermal shock from combustion and mechanical vibration from valve closing events all affect the transducer output and total summation of the pressure signal over the course of a cycle. To mitigate these sources of error, the pressure signal is pegged to a more robust known pressure during the open portion of the cycle for each cycle. This is performed by averaging the in-cylinder pressure over 10 crank angle degrees surrounding piston BDC during the intake stroke, and adjusting the entire cylinder pressure curve for the current cycle by the difference between this averaged in-cylinder pressure and the intake pressure measured through the low-speed data acquisition system. The in-cylinder pressure average is performed at piston BDC since the change in cylinder volume during this period is smallest, minimizing flow through the intake valves and thus pressure differences between the cylinder and the intake system. Flow and pressure differences can still exist due to intake flow inertia and gas heating or cooling in-cylinder, but errors due to these sources are small and repeatable, affecting all data at an operating condition equally.

The total chemical energy entering the cylinder is assumed to be contained by the fuel, and is calculated from the fuel mass per cycle after confirming that the fuel mass passed all of the consistency checks mentioned in Section 3.3. The fuel's lower heating value (LHV), hydrogen-to-carbon, and oxygen-to-carbon ratios were obtained by independently testing the fuel. Chemical energy can also enter the combustion chamber through un-burned or partially burned fuel in the external exhaust gas recirculation (eEGR) flow or the internal exhaust gas residual (iEGR) mass, as well as through combustion of lubrication oil scraped from the cylinder walls, but these sources are assumed to be negligible.

The total chemical energy present in-cylinder is not completely released due to incomplete combustion. The combustion efficiency is defined as the percentage of the fuel energy that is released during combustion in-cylinder, and is calculated from the concentrations of incomplete combustion species measured in the exhaust stream.

The equation for combustion efficiency used is from the GM test code (General Motors Engine Test Code Committee, 1994), and is presented below.

$$\boldsymbol{Comb\ Eff = 100 - \frac{100}{CO_{wet\%} + CO_{2,wet\%} + 3 \times HC_{3,wet\%}} \times \left(\frac{254 \times CO_{wet\%} + 217.1 \times H_{2,wet\%}}{LHV_{fuel} / MW_{fuel}} + 3 \times HC_{3,wet\%} \right)}$$

Equation 3-2

Emissions concentrations are all corrected to a wet percentage. Hydrocarbons are measured on a C_3 basis (assuming the average hydrocarbon molecule has three carbon atoms). Hydrogen (H_2) concentration is calculated from the difference in hydrogen in the fuel consumed and in the combination of combustion products and the water removed by the emissions bench.

The fresh (un-burned) mass entering the engine is comprised of the measured fuel flow and air flow rates. Although the engine has a direct-injection fuel system, the fuel was always delivered during the intake stroke. Therefore no specific estimation of fuel delivery rate and timing was included; the fuel was assumed to be well-mixed with the air during the intake process. Incoming mass to the engine is the fresh mass, plus the external EGR that is added as a diluent to the intake. The eEGR rate is measured by sampling the intake for CO_2 concentration, and calculating the eEGR percentage to air based on the CO_2 in fresh air and measured in the exhaust stream. All of the work presented herein did not use eEGR, making the incoming mass equal to the fresh mass.

The engine's iEGR fraction was estimated using the method presented by (Yun & Mirsky, 1974), shown in Equation 3-3 below.

$$\boldsymbol{iEGR\ fraction = \frac{V_{EVC}}{V_{EVO}} \times \left(\frac{P_{EVC}}{P_{EVO}} \right)^{\frac{1}{\gamma}}}$$

Equation 3-3

Essentially this equation states that the residual fraction is a function of the gas pressure and cylinder volume at exhaust valve opening and closing, and the ratio of specific heats of the exhaust gas. The ratio of specific heats is estimated as the polytropic expansion coefficient during the end of expansion because the in-cylinder gas temperature required to calculate the specific heat capacity relies on the residual fraction to be estimated first. The residual fraction is the mass of iEGR divided by the total cylinder mass at IVC. This calculation is performed for each cycle based on the in-cylinder pressure data at P_{EVO}, and the average exhaust pressure for P_{EVC} to minimize effects of thermal shock and valve-closing noise on the cylinder pressure transducer, as well as pressure dynamics between the exhaust and intake systems. Since the air flow and fuel flow are known, and there is no eEGR used in the data presented herein, the total cylinder mass at IVC can be calculated from the known masses with Equation 3-4.

$$m_{IVC} = m_{incoming} \times \frac{1}{1 - Residual\ Fraction}$$ Equation 3-4

Molecular weights of all the various components are also tracked, and a mass-averaged molecular weight for the entire mixture for the closed portion of the cycle is calculated from the components.

3.5.2 Crevice/Porosity Model

Once the intake valve was closed, the mass at IVC was assumed to be trapped in-cylinder until EVO. The only path for mass flow during this time was through the crevice volumes and ring gaps between the piston and bore. The crevice flow model proposed by (Namazian & Heywood, 1982) was adopted and modified for this purpose. This model was envisioned as a series of sub-volumes connected to each other through small orifices, eventually connected to an infinite (constant pressure) volume representing the crankcase. The gas contained within all of the crevice volumes was assumed to be the same composition as the combustion chamber gas for the purposes of this analysis, fitting with the homogeneous operation of the engine. All of the gas within the crevice volumes was assumed to be at the wall temperature, which forced any gas entering the crevice to instantaneously transfer energy to the walls in order to satisfy this assumption. Mass leaving a crevice volume (whether back to the combustion chamber, to another crevice volume, or to the crankcase) did not represent a further heat transfer between the gas and the wall since all walls were at the same temperature. Gas flows between orifices were calculated based on the difference in pressure between adjacent volumes, orifice size (ring gap and thickness), wall temperature, speed of sound within the gas, and gas compressibility factor.

Modifications to the crevice model were made to suit the needs of the experimental data and the author's hypothesis that some of the coatings tested were porous, permeable and had significant volume that was open to the combustion chamber. The top crevice volume, which typically represented the area between the piston and the bore wall above the top ring, was repurposed to simulate the sub-volume within the porous coating. Therefore the top crevice volume over the first ring was assumed to be a part of the combustion chamber volume and was not treated separately. This porosity volume was assumed to be connected to the combustion chamber with no restriction. Therefore, it was at the same pressure as the combustion chamber, and mass flows were calculated based on the difference in density derived from the difference in temperature between the combustion chamber and the walls. No additional sub-volumes or orifices were modeled, so mass trapped in-cylinder could only exist in the combustion chamber or in the porosity volume. The wall temperature was allowed to change throughout the cycle, which forced the gas within the porosity to change temperature as well. This introduced a second source of heat transfer

between the wall and gas derived from this change in temperature and the heat capacity of the gas. The total heat transfer attributed to porosity was the heat lost from mass entering the porosity volume plus the change in temperature of mass already in the porosity volume due to wall temperature swing, described in Section 3.5.4.

3.5.3 In-Cylinder Properties

The average gas temperature within the combustion chamber is calculated in a variety of ways for different portions of the cycle. The basis of the temperature calculation is a single-zone model, with adaptations to conserve mass and energy with the addition of the porosity sub-volume. While the end result does have two zones, it is not a typical two-zone model where the burned and unburned mixture are separately tracked. This level of additional precision was not deemed necessary since the in-cylinder thermal convection coefficient correlations only use a single-zone, mass-averaged temperature. Specific tracking of burned-zone volume and flame-wetted areas of each component would be possible, but would be adding considerable complexity that would not be verified through measurements for this combustion system. Additionally, to adequately capture the spacial effects that could be predicted by a conventional two-zone model, the engine thermal model would need to be refined considerably further to reflect the actual engine geometry more accurately. Ultimately, a single-zone combustion chamber model, plus the porosity sub-volume, was deemed acceptable for the general level of precision desired of the results.

Three distinct regimes are used for the calculation of the combustion chamber temperature. They are the closed-cycle portion using the ideal gas law, the exhaust event which uses an adaptation of the iEGR estimation equation by (Yun & Mirsky, 1974) presented above, and the intake event which specifies a “blending rate” based on the cylinder volume and valve events. Each of these regimes is shown in Figure 3-3 for a representative test condition, and are discussed independently below. Special care has been taken to preserve continuity from one cycle to the next as these events often span multiple 720 degree periods, although some level of discontinuity must be accepted due to the cylinder pressure pegging.

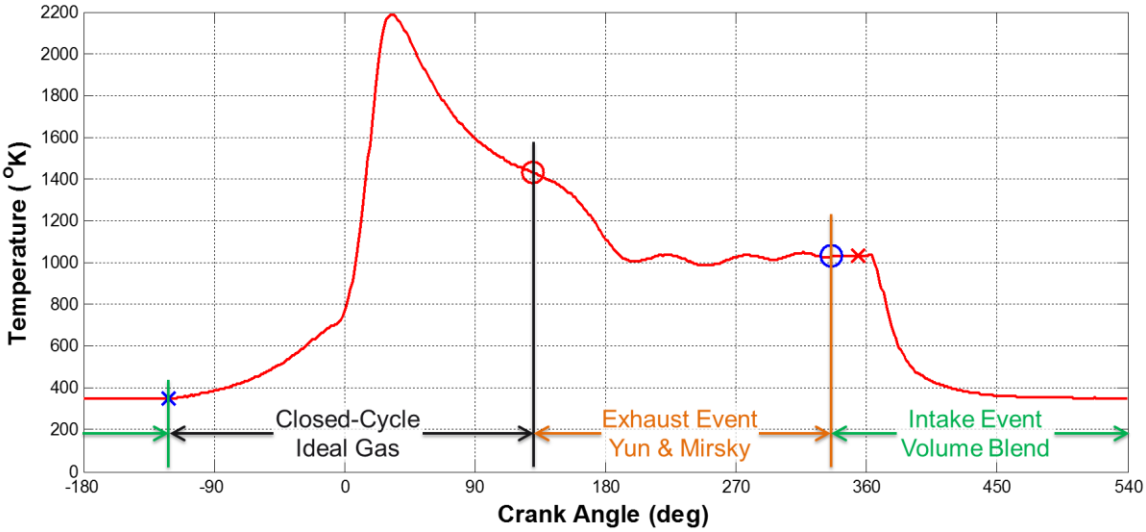

Figure 3-3: Combustion Chamber Temperature Calculation Regimes

The combustion chamber temperature is calculated for the closed portion of the cycle from the cylinder pressure and mass using the ideal gas law shown in Equation 3-5.

$$PV = nRT = m\bar{R}T \qquad \text{Equation 3-5}$$

This calculation only uses the mass present in the combustion chamber and the volume of the combustion chamber, excluding the porosity volume. The mass-averaged temperature of the combination of combustion chamber and porosity volumes is the same as the temperature calculated using the combined combustion chamber and porosity volumes and masses, proving conservation of energy and mass.

Once the exhaust valve opens, shown by the red circle in Figure 3-3, temperature is estimated using an adaptation of the Yun and Mirsky iEGR estimation equation. By substituting the ideal gas law into Equation 3-3, taking the EVC state to represent each measurement point during the exhaust event in the combustion chamber ("$_{cc}$"), and re-arranging the equation to solve for the temperature at each state, the following equation is arrived at.

$$T_{cc} = T_{EVO} \times \left(\frac{P_{EVO}}{P}\right)^{\frac{1}{\gamma}-1} \qquad \text{Equation 3-6}$$

The ratio of specific heats is represented by the polytropic expansion coefficient here as well, for consistency with the residual mass estimation equation. This equation captures the drop in combustion chamber temperature due to blow-down, and then maintains a roughly constant temperature until the end of the exhaust event regime.

Mass-averaged temperature during the intake event is more complicated to estimate, since it depends on the flow rates and temperatures of the exhaust and intake during

the overlap period, and can be affected by intake or exhaust flow "short-circuiting" through the engine to the opposite manifold without mixing. This process was simplified by relying on the measured pressure during the intake and the primary driver of the intake process, which is the expansion of the cylinder volume.

A normalized volume curve from exhaust temperature at IVO to temperature at IVC (calculated from trapped mass and pressure) is constructed based on the cylinder volume during the intake stroke. Essentially, the cylinder volume during this time is normalized to this range, with the temperature held constant at T_{IVO} between IVO and minimum volume, and at T_{IVC} between maximum volume and IVC. These regions are at constant temperature since it is assumed that exhaust is being pushed into the intake and exhaust systems between IVO and TDC, and that the mixture of fresh charge and residual is being pushed back into the intake system between BDC and IVC. Neither of these events should significantly affect the in-cylinder temperature unless very large amounts of short-circuiting are occurring due to large amounts of valve event overlap. Mass-averaged temperature in-cylinder is calculated using the cylinder pressure and the change in this volume curve from its minimum, with the assumption that any change in mass is from the intake system and is therefore at intake temperature. A normalized curve was used to ensure that the cylinder mass at EVC and IVC was the same as predicted by residual calculations and incoming mass measurements.

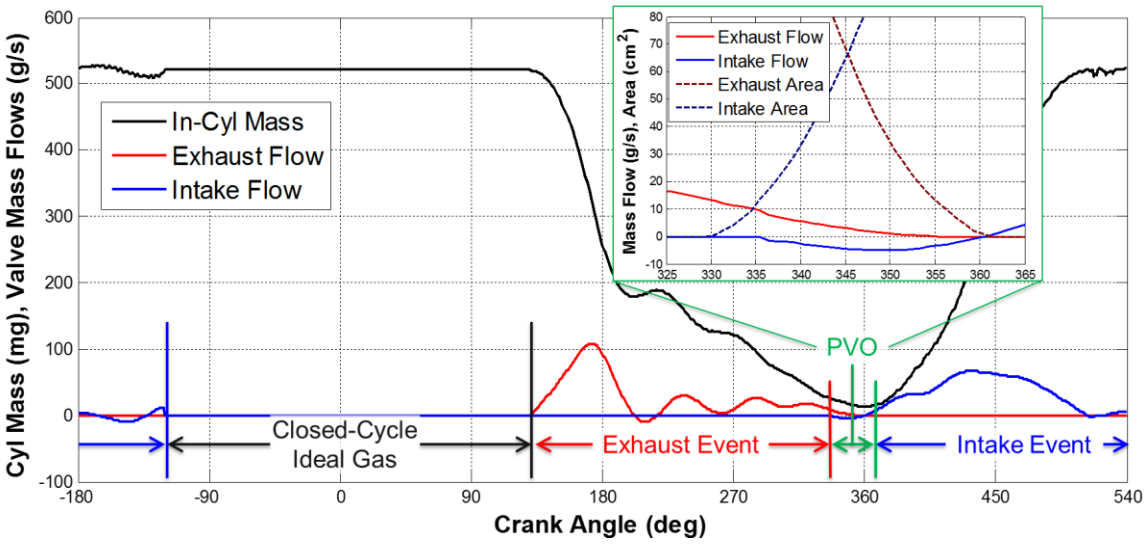

Figure 3-4: Cylinder Mass and Valve Flow Calculation at 2000 RPM, 20 mg/cycle Fueling Point

The in-cylinder mass can be calculated using the ideal gas law once the combustion chamber temperature has been estimated, because the estimates for temperature during open portions of the cycle account for mass transfer. Mass flows through the valves are then solved for based on the change in cylinder mass. During the positive

valve overlap (PVO) region when intake and exhaust valves are simultaneously open, the mass flows are weighted by the relative difference in intake, cylinder, and exhaust pressure and by the total valve flow area including discharge coefficients to maintain the calculated change in cylinder mass. This method attempts to capture cross-flows from one manifold to the other, with some negative intake flow shown in the inset in Figure 3-4 at this throttled operating point. Overall, the mass flows calculated capture blow-down events and flow fluctuations driven by pressure waves in the measured data.

$$\boldsymbol{\gamma = a + b \times T = (1.392) + \left(-7.83 \times 10^{-5}\right) \times T} \qquad \textbf{Equation 3-7}$$

The specific heats and the ratio between them are estimated directly from the combustion chamber gas temperature. A simple linear correlation shown in Equation 3-7 of the form proposed by (Gatowski, et al., 1984) is used, with the temperature dependent coefficient as -7.83e-5 to better capture the gas properties over the range typically experienced by throttled, near-stoichiometric gasoline engines. This is a large simplification of the complex contributions of temperature and mixture composition as combustion occurs, but it avoids the need to iteratively solve the heat release rate and chemical equilibrium equations to estimate composition to achieve convergence while providing reasonable accuracy.

3.5.4 Heat Transfer Estimation

Heat transfer between the gas and the walls is the sum of convection and porosity heat losses. Effects due to radiation are neglected for this analysis because homogeneous, slightly lean SI combustion is used, which minimizes the formation of soot and other black bodies that are the source of most radiation. Additionally, homogeneous combustion will have lower peak temperatures than stratified combustion at a constant specific load since locally rich pockets that combust at a higher adiabatic flame temperature will not be present. Radiation is dependent on the temperature to the fourth power, so the difference between homogeneous and stratified combustion will be magnified. Energy closure during the closed portion of the cycle is employed to capture any additional losses that are not explicitly calculated.

A formulation of Woschni's seminal convection coefficient approximation (Woschni, 1967) (Sihling & Woschni, 1979) is used to estimate the convection between the gas and the wall as discussed in the literature review. Many models exist for estimating convection in internal combustion engines, but this form of Woschni's equations was chosen due to the amount of historical work and data collected and analyzed with it that could be compared to. The general form of the equation is maintained, but the coefficients held constant regardless of whether the cycle is open or closed. Instead,

a single set of coefficients is used to maintain a continuous formula to avoid driving wall temperature discontinuities based solely on the change in coefficient. The equations for this formulation of the convection coefficient are presented below.

$$v_{gas} = 2.28 \times \overline{v}_{piston} + 0.308 \times \omega_{swirl} + 0.00324 \times \frac{V_{displ}}{V_{IVC}} \times \frac{P - P_{motor}}{P_{IVC}} \times T_{IVC}$$

Equation 3-8

$$h_{conv} = 3.26 \times L^{-0.2} \times P^{0.8} \times T_{cc}^{-0.53} \times v_{gas}^{0.8}$$

Equation 3-9

$$\dot{Q}_{conv} = h_{conv} \times A \times (T_{cc} - T_{wall}) = \sum_1^n h_{conv} \times A_i \times (T_{cc} - T_{wall,i})$$

Equation 3-10

The term v_{gas} is meant to capture the local velocity of the gas across the wall, and is a function of the mean piston speed, the amount of in-cylinder motion generated by the intake process (represented by the swirl coefficient, c_{swirl}), and a term representing the flame front estimated by the difference in combustion chamber pressure vs a hypothetical motored pressure calculated from isenthalpic compression and expansion from a reference point. In general, reference conditions are taken to be at IVC when the closed-cycle calculations begin. The gas velocity, combustion chamber pressure (P), and combustion chamber temperature (T_{cc}) are all raised to powers deriving from the correlations back to the Reynolds and Nusselt numbers in-cylinder, and the leading multiplier of 3.26 is a constant required to correct the cycle-averaged heat transfer predicted with this formulation back to the range empirically experienced in similar homogeneous SI engines. The total convective heat transfer rate is solved as the sum of individual heat transfer between the combustion chamber and each engine component (indexed by "*i*" in Equation 3-10), using those components' area-averaged surface temperatures and total area instantaneously exposed to the combustion gas.

In addition to convection, heat is transferred between the gas and walls due to the assumptions of the crevice model used to capture the permeable porosity effects. Heat transfer due to porosity has two components. The first is due to mass entering the porosity volume instantaneously assuming the wall temperature, and the second derives from the change in wall temperature throughout the cycle forcing the gas to change in temperature as well, which requires heat transfer to or from the crevice wall. The total heat transfer rate due to the porosity is captured in Equation 3-11.

$$\dot{Q}_{por} = \frac{\Delta m_{por,in}}{\Delta t} \times \Delta t \times c_v \times (T_{cc} - T_{porosity}) + m_{porosity} \times c_v \times \frac{\Delta T_{por}}{\Delta t}$$

Equation 3-11

3.5.5 Heat Release Calculation

The net heat released into the gas during the closed portion of the cycle is estimated by the change in cylinder pressure beyond what would be expected without

combustion using the first law of thermodynamics. The rate of heat addition must comprehend that both the pressure and the volume are instantaneously changing, and that energy is being added and removed from the gas through mechanical work. The net heat release rate (HRR_{net}) equation is formulated from the equations for internal energy and mechanical work, and is transformed into Equation 3-12 using the ideal gas law and relationships between the universal gas constant, the specific heat capacity at constant volume, the specific heat capacity at constant pressure, and the ratio of specific heats.

$$\boldsymbol{HRR_{net}} = \frac{\boldsymbol{\gamma}}{\boldsymbol{\gamma-1}} \times \boldsymbol{P} \times \frac{\boldsymbol{\Delta V_{cc}}}{\boldsymbol{\Delta crank\ ang}} + \frac{\boldsymbol{1}}{\boldsymbol{\gamma-1}} \times \boldsymbol{V_{cc}} \times \frac{\boldsymbol{\Delta P_{cc}}}{\boldsymbol{\Delta crank\ ang}} \qquad \textbf{Equation 3-12}$$

The ratio of specific heats used here is the instantaneous ratio calculated from the temperature. The heat release rate calculated by this equation is the energy released per crank angle degree, as that is the derivative taken of the volume and pressure. A 2nd order Butterworth filter was applied to the pressure derivative to smooth out noise in the signal without shifting the data.

The net HRR is the energy that is observed as appearing in the cylinder pressure measurement, comprehending energy extracted through mechanical work. However, energy is simultaneously being lost from the combustion chamber control volume through heat transfer, which is not captured in the HRR_{net}. Therefore, the gross heat release rate (HRR_{gross}) representing the total rate at which chemical energy in the fuel is converted into pressure and temperature within the cylinder must be calculated as the sum of the HRR_{net} and the total heat loss from convection and porosity.

3.5.6 Energy Closure

If the gross HRR captures the total rate at which fuel chemical energy is released, then the average cumulative heat release rate should equal the total chemical energy available in the fuel, less the chemical energy contained in species measured in the exhaust. Energy closure between the combustion efficiency and the cumulative gross heat release, normalized by the total fuel energy, is achieved by scaling the convective heat transfer through the use of the energy closure multiplier α. Energy closure is evaluated just prior to EVO during the closed portion of the cycle, when the only changes to the energy within the combustion chamber control and porosity control volume are the fuel chemical energy released, work extraction (comprehended in the HRR_{net}) and heat losses through convection and porosity. The energy closure multiplier is carried throughout the open portion of the cycle, affecting total convective heat transfer rates for data taken at this condition. This multiplier is calculated as a single number for all of the cycles recorded at a point, since the latency of emissions within the exhaust system and the emissions analysis speed in calculating species concentrations are too slow to calculate the combustion efficiency

for individual cycles. This results in individual cycles that have a gross cumulative heat release greater or less than the fuel energy available, which is possible due to potential variations in fuel mass injected in each cycle, variations in combustion between cycles, the effects of unburned fuel from previous cycles in the residual gas of the current cycle, and errors in in-cylinder pressure measurement. Ultimately, the energy closure multiplier was envisioned to correct the convection coefficient for conditions when prediction is imperfect, but it will also capture any other un-accounted-for sources of measurement or prediction error during the closed portion of the cycle. Due to this, the energy closure multiplier can be used as a measure of how well all of the interactions in-cylinder are comparing to baseline results at a specific operating point, or how well the expected results of the models and assumptions in the data analysis program agree.

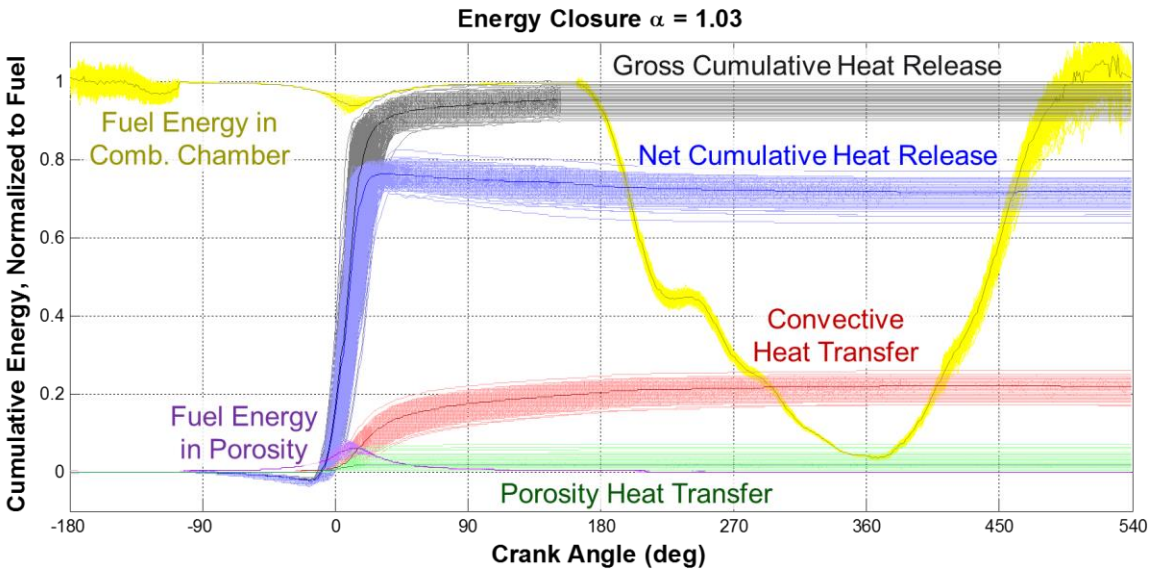

Figure 3-5: Energy Accounting and Closure in Data Analysis Program

A sample of the results of the entire data analysis program including energy closure is shown above in Figure 3-5. These results were obtained with a permeable, porous coating to illustrate the energy accounting from all sources that occurs within the data analysis program, and is the same 2000 RPM, 0.6 bar intake pressure operating condition used earlier. The darker lines represent the ensemble average of all recorded cycles, while lighter colored ranges are generated by plotting each cycle of the 300 total recorded. The convective heat transfer is scaled such that the gross cumulative heat release just prior to EVO equals the combustion efficiency multiplied by the energy within the total amount of fuel injected. The fuel energy available in the combustion chamber is shown for reference, and is calculated from the mass in the combustion chamber, accounting for mass transfer to the porosity volume. If all assumptions are met then the gross cumulative heat release should never exceed the fuel energy in the combustion chamber, but it is the total fuel mass injected multiplied

by the LHV and the combustion efficiency that determines the amount that the gross cumulative heat release is corrected to. Theoretically, over time running at steady state, the porosity volume would collect a certain mixture of unburned fuel and air mixture and maintain it between cycles, so that the total fuel injected would be available in the combustion chamber.

3.5.7 Knock Amplitude

The knock amplitude was calculated as a metric to capture the severity of autoignition events. This metric is the greatest individual absolute value of a knock peak or trough during expansion over the filtered pressure trace in any of the cycles recorded during a measurement, and reflects the worst knocking event recorded at that operating condition. Filtering is performed utilizing the bore diameter and estimations of the speed of sound to specifically eliminate the frequencies at which knock would be apparent in the "Filtered Pressure" trace, without introducing a lag and minimizing sensitivity to strong SI combustion. The "Knock Pressure" trace is then calculated as the difference between the two, and the knock amplitude is the greatest absolute-value in the knock pressure.

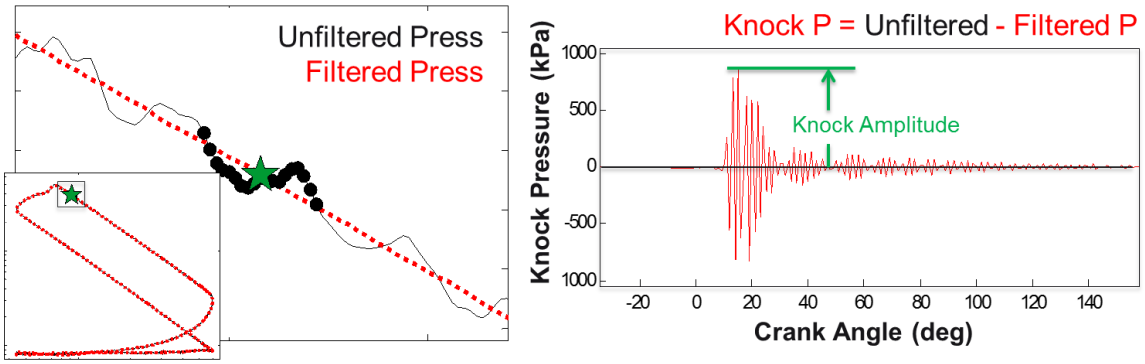

Figure 3-6: Knock Frequency Filtering and Amplitude Calculation

3.6. Heat Flux Probe

A heat flux probe was used throughout the experimental engine testing. Fundamentally, the heat flux probe is a pair of two fast-response thermocouples, with one mounted on the probe face and the other mounted at a known depth. Assuming 1-dimensional heat transfer through the probe and knowing the material properties of the probe, it is therefore possible to calculate the heat flux between the two thermocouples at each crank angle. The probe was mounted in the cylinder head next to the high-speed pressure transducer as shown in Figure 3-2 with the front surface flush with the combustion chamber, between the intake and exhaust valves in the periphery of the chamber. Typically, the probe recorded peak heat flux rates when

70% to 80% of the combustible mass had been consumed, dependent upon combustion phasing and load.

The primary purpose of the heat flux probe was in confirming the repeatability of the in-cylinder thermal environment between points and hardware sets. SI combustion is fundamentally a travelling flame front that sweeps through the flammable mass and across the combustion chamber surface; therefore the heat flux recorded at different points along the chamber surface will be significantly different. The assembly of an average heat flux profile for the gas that encompasses the entire surface would require many individual probes in all of the engine components, which was impractical for this study. Therefore, comparison of the calculated heat flux from the probe to the average heat flux calculated through Woschni's equations and energy closure is impossible.

3.6.1 Probe Construction and Operation

Construction of the Medtherm heat flux probe is described in Figure 3-7. The probe consists of a pair of co-axial fast-response J-type thermocouples, with the junction created by a very thin vapor-deposited layer that spans the two thermocouple elements. The first junction, referred to as the surface thermocouple, is located at the end of the heat flux probe exposed to the combustion chamber gasses. The second junction is located within the probe at a depth of 4mm from the surface, and is referred to as the backside thermocouple. This displacement allows for the calculation of the one-dimensional heat flux through the probe.

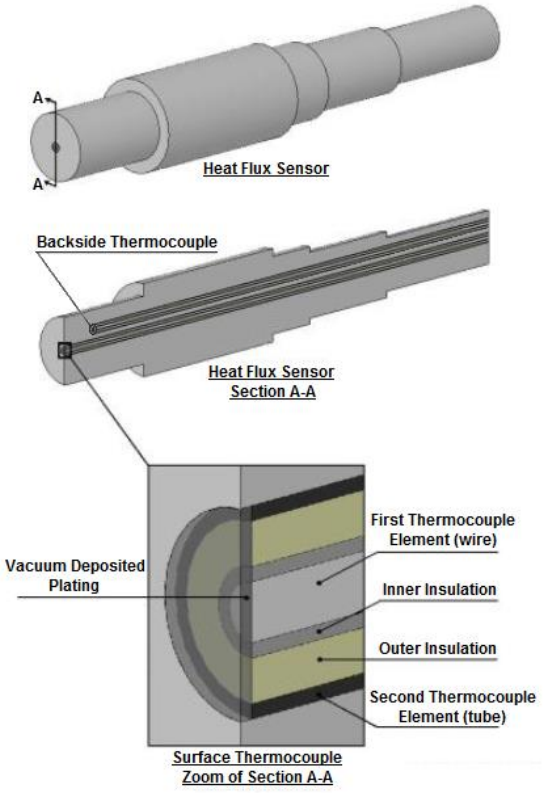

Figure 3-7: Heat Flux Sensor Construction, from (Hoffman, 2012)

As noted previously, the heat flux probe is a point measurement at a specific location on the chamber surface. Since the combustion mode is spatially very inhomogeneous, the heat flux experienced by the probe cannot represent the average heat flux from the gas to the wall. The surface temperature with the probe is different than the temperature that would occur without the presence of the probe due to the material properties of the thermocouple elements of Iron and Constantan (a Copper-Nickel alloy), although the effects of adding the probe

can be minimized as shown in literature. Additionally, the thermal response of these elements will affect the magnitude of temperature swing that they experience and record, tending to slightly amplify the temperature swing. Small differences in the peak temperature can translate into much larger errors in the calculated heat flux, so caution must be taken when analyzing the heat flux profiles. Deposit formation can occur on the surface of the heat flux probe as well, which tends to mute and delay the temperature swing profile, affecting the calculated heat flux. In the experimental testing presented here, the heat flux probe was cleaned once a week, or more often if the peak heat flux rate was noted to be lagging at control points. The engine was operated at a lambda equivalence ratio of 1.1, which was determined to reduce the deposit formation rate by providing a more oxidizing environment after combustion to aid deposit burn-off.

3.6.2 Conversion to Temperature and Heat Flux

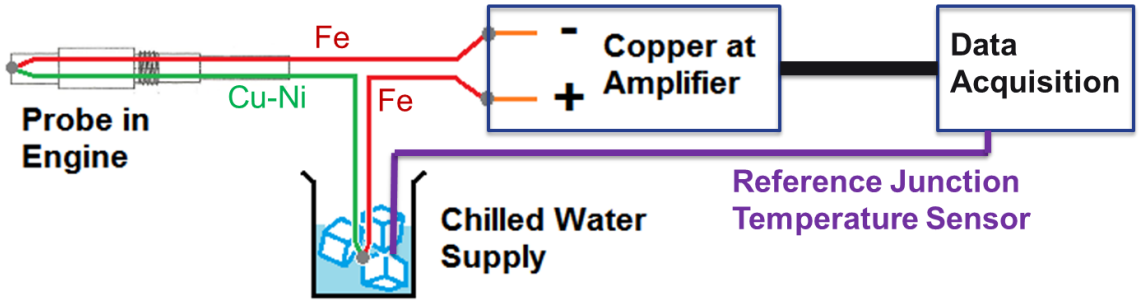

Figure 3-8: Heat Flux Probe Cold Junction and Amplification

The surface thermocouple of the heat flux probe has a response rate on the order of 1 microsecond due to the low mass of the thin, vapor-deposited junction layer. In order to capture the high-speed thermocouple response, an analog cold junction was set up as shown in Figure 3-8. A second J-type thermocouple was installed into a stable thermal mass cooled by chilled water to form a reference junction with its constantan leg connected to the constantan leg of the surface thermocouple. This setup ensures that the only dissimilar metal junctions that exist at unknown temperature are the iron to copper junctions at the amplifier. The effects of these junctions cancel each other out since they are aligned in opposite directions to current flow through the circuit and are assumed to be at the same temperature. Therefore, the voltage measured at the amplifier is the difference between the voltage generated by the heat flux probe thermocouple and the voltage generated by the reference junction thermocouple. The reference junction temperature is independently measured and recorded in the data acquisition system, which allows calculation of the probe surface temperature. This setup was duplicated for the

backside thermocouple using a second reference junction thermocouple and amplifier channel, but was not depicted in Figure 3-8 for clarity.

An AVL MicroIFEM Multipurpose 2M1 two-channel instrumentation amplifier was used for precise, repeatable thermocouple amplification with no frequency filtering at 500X gain. It was zeroed each morning prior to warming up the engine to account for signal drift over time. The cylinder head was assumed to be isothermal after sitting overnight, and the coolant temperature measured next to the heat flux probe was taken as a surrogate for the heat flux probe thermocouple temperatures. A target voltage at the high-speed data acquisition was calculated using this temperature and the reference junction temperature. A linearly estimated J-type thermocouple voltage calibration constant of 0.051mV/°C was valid over the narrow calibration range of 0 to 30°C for purposes of calibration, and the amplifier gain was required to complete the target voltage calculation. The actual measured voltage was compared to this target, and the zero offset on the amplifier was adjusted to align the actual with the target.

Temperature was calculated for the surface and backside thermocouples from the measured voltage in multiple steps. First, the reference junction voltage was calculated using the independent reference junction temperature measurement, and was subtracted from the high-speed measured voltage. The depth of the backside thermocouple within the probe assured that any transient heat flux throughout the cycle had been damped out by thermal inertia before reaching the backside thermocouple, thus it would not change temperature throughout the cycle. Noise on both the surface and backside thermocouple signals induced by the spark plug, injector, and other electrical sources could therefore be measured as the divergence of the backside voltage from the median (not mean) recorded voltage. Using the mean voltage for this correction would bias the results based on the duration and offset of the noise, which could occur over a fairly long portion of the cycle when induced by the injection or spark event. This would lead to a systematic error in the correction, which would affect the heat transfer rate calculated from the heat flux probe. Cancellation of this noise could then be applied to the surface thermocouple, producing a cleaner signal but without the delay or smoothing that typical filtering can introduce. The voltage was then converted into temperature using linear interpolation with a standard J-type thermocouple table (Omega, 2016).

Once the surface and backside thermocouple temperatures were known, average and transient heat fluxes were calculated using the methods described by (Alkidas, 1980). The heat transfer shape and total rate were monitored between datasets and engine builds to ensure similarity between operating points with different hardware sets.

4. Computational Methods

4.1. Introduction

When modeling physical systems, it is important to attempt to capture the physical processes in play while avoiding over-complication or a level of detail that is not supported by the experimental data or other modeling assumptions. Otherwise, much effort and computational time can be spent in pursuit of precision in one aspect that is overshadowed by experimental or analytical uncertainty in another aspect. With this in mind, the following models were created, utilized, and calibrated to observed data to enable meaningful analysis of the results presented in later sections.

4.2. 0D/1D Engine Thermodynamic Model

4.2.1 Model Description

GT-Power, a 0-dimensional commercially available engine thermodynamic model, was used to simulate the single-cylinder engine and extend the learnings available through experimentation. The combustion chamber model treats the gas as burned and unburned zones, with mass moving from unburned to burned zones as prescribed by a fuel mass burned curve. Composite gas properties are solved for based on the concentrations of basic molecules such as N_2, O_2, CO_2, CO, H_2O, H_2, and fuel (with user-specified chemical composition). Concentrations of these molecules in the gas and fuel sources are specified, with perfect mixing assumed within sub-volumes and the cylinder itself. Gaseous mixture concentrations in-cylinder are solved for during combustion by solving equilibrium reactions to achieve the prescribed fuel mass burned rate, which is derived from the experimental analysis. The resulting heat release curve was calculated from the chemical equilibrium solution, and the input fuel mass burned rate was corrected to achieve the same heat release rate in the thermodynamic model and the experimental data. This model could calculate a burned and unburned zone temperature, and flame-wetted areas on each component. For comparison to experimental data, the burned and unburned temperatures were forced to be the same (the bulk-gas temperature) to ensure that the heat transfer rates would be calculated in the same way. Predictive studies used individual zone temperatures and the calculated flame-wetted areas. This difference affected the shape of the heat transfer rate, but the total cycle-averaged heat transfer energy from the gas was within 5% of otherwise identical single-zone analyses.

Flow to and from the engine was modeled as a series of sealed pipes and volumes to capture wave dynamics in the manifolds and ports. The geometry of the model was made to match the physical engine as closely as possible up until large settling tanks for the intake and exhaust systems. These tanks were modeled as end-environments at constant pressure and temperature that effectively acted as sources and sinks for the gas. The intake pressure from the end-environment was controlled to provide specified air flow and the fuel mass injected was specified to ensure that the total mass flow was consistent with experiments or held constant for analytical studies.

4.2.2 Calibration to Experimental Data

The thermodynamic model described above was built and calibrated to experimental data taken and used throughout this work. The calibration was focused on duplicating the in-cylinder conditions and heat losses of the un-insulated engine configuration, so that all of the effects of adding in-cylinder insulation could be compared to expected trends.

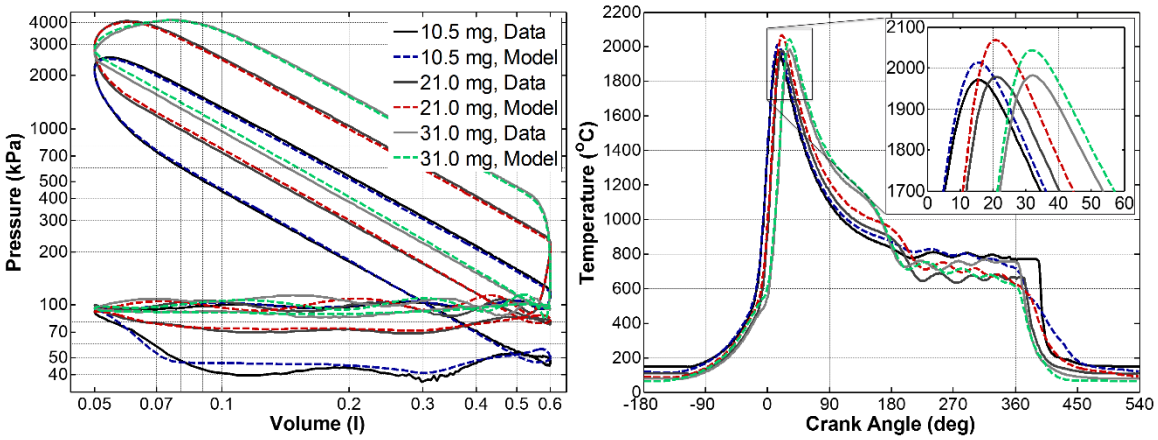

Figure 4-1: Thermodynamic Model vs Experimental Pressure and Temperature Comparison

Boundary conditions such as environment pressures and temperatures, engine geometry and speed, fueling rate, valve profiles, discharge coefficients and timings, and properties of the fuel were all specified to match the experimental testing. The air to fuel ratio (AFR) in the model's exhaust was controlled to match the experiment by varying the intake pressure provided by the intake end-environment. The experimental normalized heat release profile and combustion efficiency were imposed directly on the model to dictate the conversion of chemical energy to thermal energy, with a correction applied to account for the thermodynamic software's fuel-mass-burned to cumulative-heat-release-rate calculations. The energy closure multiplier for convection from experimental data for each point was applied to convection in the model to capture inadequacies in the Woschni estimations with speed, load, and combustion phasing. These multipliers were 0.92 at the 10.5 mg

fueling point, 1.19 at 21.0 mg, and 1.54 at 31.0 mg. The highest load point has the highest multiplier primarily due to the retarded combustion phasing used to avoid knock.

The resulting agreement between experimental data from an un-insulated engine and the thermodynamic model can be seen in Figure 4-1. Although it is difficult to discern, the intake and exhaust pulsations are captured reasonably well at these three loads, as are the gas temperatures during gas exchange. The closed-cycle pressures and temperatures also match well, with slight differences in the compression slope and peak temperatures.

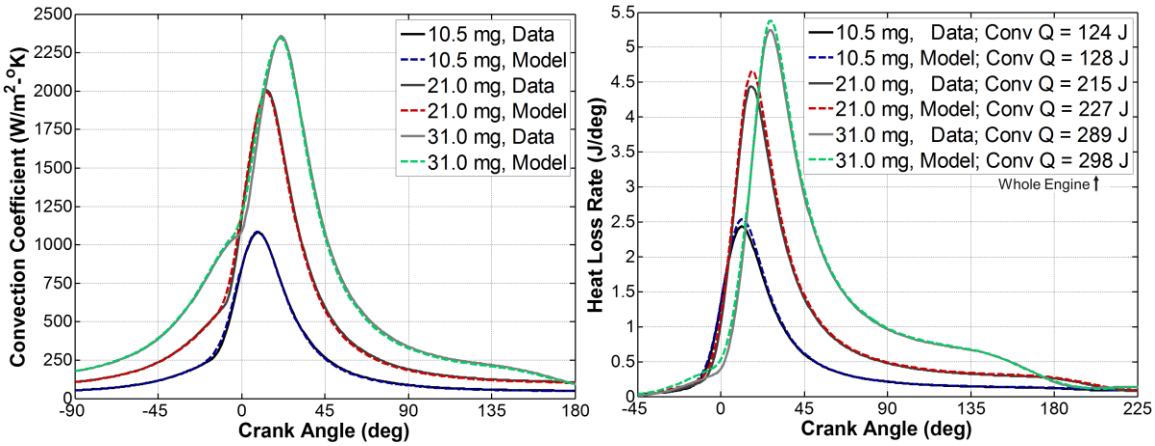

Figure 4-2: Thermodynamic Model vs Experimental Convection Coefficient and Total Heat Loss Comparison

The close agreement between the model and data pressures, temperatures, mass flows, and general operation led to accurate calculations of the convection coefficient and the total heat loss rate from the gas. Total heat loss for each plotted case is shown in the legend of the right plot in Figure 4-2, with agreement in all cases of less than 5%. The thermal model discussed in the next section was used for both the experimental data and thermodynamic model results to calculate component surface temperatures used for the heat loss calculation.

4.3. 2D Thermal Wall Model

4.3.1 General Model Formulation

A 2-dimensional implicit thermal finite-element model was written in MATLAB scripting language to interface with the engine thermodynamic model and the experimental data analysis. The purpose of this model was to be able to predict the instantaneous surface temperatures of the engine components based on the material properties, component structure, engine operating conditions, and boundary conditions. Implicit (backwards-difference) methods were used to ensure model

stability while maintaining freedom of timestep lengths and finite element size. The engine was assumed to be radially symmetric, neglecting details such as the piston wrist-pin structure, possible siamese-bore details, and specific valve positioning in the head. This level of simplification was deemed acceptable since the combustion chamber temperature and heat transfer model in the data analysis and thermodynamic simulation were fundamentally zero-dimensional (single-zone), and the resulting surface temperatures were being used to predict bulk heat transfer trends. This simplification enables a much smaller, faster model that is easier to program and run. Similarly, maximum precision was desired at the wall's combustion surface where heat transfer is primarily 1-dimensional away from the gas, so geometric details perpendicular to this dimension were simplified to minimize complexity and speed solution of the model. Single-zone combustion gas temperature and heat transfer coefficient as predicted by a convection model (Woschni, 1967) were taken as the thermal source, while the temperatures and heat transfer coefficients to thermal sinks for each component were calibrated based on experimental data and values in literature. Temperature-dependent material properties were taken from literature or experimentally measured, and were linearly interpolated for each element using the node temperature at each timestep throughout the engine cycle.

The general form of the heat transfer equations used was one-dimensional, so that links could be made between any two finite elements. Geometric considerations such as intermittent contact, radial axis orientation, and partially masked cross-sectional areas were accounted for in the specification of connecting areas, distances, and each element's volume. The classical heat transfer equation containing conduction and convection terms, formulated for an implicit finite difference solution with individual elements containing a centroid node for which the thermal properties are calculated, is shown in Equation 4-1.

$$\rho_i V_i c_i \frac{(T_i^{t+1} - T_i^t)}{dt} = h_{ij} A_{ij} \left(T_j^{t+1} - T_i^{t+1}\right) + \frac{k_{hi} A_{hi}}{d_{hi}} \left(T_h^{t+1} - T_i^{t+1}\right) \qquad \text{Equation 4-1}$$

Variable "ρ" is the element density, "V" is the volume, "c" is the specific heat capacity, "T" is temperature and "dt" is the timestep. Variable "h" is the convection coefficient, "A" is the area for convection or conduction, "k" is the thermal conductivity, and "d" is the total distance between nodes. Subscript "i" represents the node of the current element, subscript "j" represents the node of an element with convection to "i", and subscript "h" represents the node of an element with conduction to "i". Superscript "t" represents the value at the current time, while superscript "$t+1$" represents the value at the next timestep.

However, this equation is not complete for our purposes since it assumes that conduction between the nodes of two elements is across a distance with constant

conductivity, and that convection occurs using the temperature at the node of each element. Equation 4-1 was re-written to separate the conduction within the boundaries of each element. Convection between nodes was captured as conduction from the first element's node to its surface, then convection between the first and second element surfaces, followed by conduction from the second element's surface to its centroid node. This is shown in Equation 4-2.

$$\rho_i V_i c_i \frac{(T_i^{t+1} - T_i^t)}{dt} = \frac{(T_j^{t+1} - T_i^{t+1})}{\frac{1}{h_{ij}A_{ij}} + \frac{d_{i-s}}{k_i A_{ij}} + \frac{d_{j-s}}{k_j A_{ij}}} + \frac{(T_h^{t+1} - T_i^{t+1})}{\frac{d_{h-s}}{k_h A_{hi}} + \frac{d_{i-s}}{k_i A_{hi}}} \qquad \text{Equation 4-2}$$

Subscripts with "-s" indicate the distance from the node to surface of the referenced element. Combinations of subscripts indicate shared values, such as the cross-sectional area between nodes "i" and "j" depicted as A_{ij}. Both convection and conduction could use the same convection term as well, since convection with an infinite coefficient is equivalent to conduction. The appropriate distance between the node and the element surface depends on the conduction or convection connection: all finite meshing elements are assumed to be rectangular so the distance parallel to convection from the combustion chamber gas can be different from the direction towards surrounding elements in conduction within a component.

The calculation rate at which the wall temperatures were solved could be down-sampled from the rate at which experimental data was taken or the frequency at which the thermodynamic model provided a solution. Down-sampling from 1440 points/cycle (data acquisition rate equivalent to 0.5° crank angle steps) to 180 points/ cycle (4° crank angle steps) only produced a 0.5% difference in the average temperature and a 1% maximum difference in temperature at any individual point in the cycle. The calculation time using 180 points/ cycle was slightly over $1/8^{th}$ of the time for the 1440 points/cycle as expected, due to some computational overhead that is necessary regardless of sample rate. Down-sampling was done by taking the mean of the original points that were contained within the range of each individual down-sampled point, weighted by the percentage of each original point within the down-sampled point's range. This method preserves the total heat flow of the original, finer resolution data and does not risk mis-estimating spikes or transients the way that interpolation would. Down-sampling by interpolation approximately doubled the minimum down-sampling resolution to 360 points/cycle while maintaining a 0.5% difference in the cycle-average temperature. The implicit formulation of the model enables this method of speeding calculation time without risking model instability the way an explicit formulation would.

The engine structure is split between five components that are exposed to the combustion gas; the piston, head, bore, intake valves, and exhaust valves. Each component consists of multiple paths that are oriented from the combustion chamber

surface back to a heat sink. These paths are comprised of individual layers of specific thicknesses, material properties, and convection coefficients to the surrounding layers (conduction is assumed between layers unless explicitly disabled). Finite elements are automatically assigned positions and sizes within layers based on the material properties and nature of the heat flux at the layer boundaries to maintain model accuracy while minimizing the number of elements and thus calculation time. More details on element mesh generation are given in the next section.

A general representation of the piston and bore components, their structural layout, and their interactions is shown in Figure 4-3. The piston model in this example consists of two paths, with the outermost path including the piston skirt. Heat is lost through convection to the oil from the underside of the piston crown and inside of the piston skirt. Convection can also occur between the outermost path in the piston and paths in the bore. The amount of convection between these components tracks the relative positions of the piston and bore and calculates the overlapping area between outside elements in the piston and the top (inner surface) elements in the bore to apply the correct amount heat to the each path in the bore at every timestep. Likewise, the surface area of the first element of each path in the bore that is exposed to the combustion gas is calculated based on the piston position. This allows the bore's surface area to be masked by the piston based on the piston's position within the cycle. Convection coefficients and exposed areas for the piston and bore backsides are assumed to be constant. Heat off of the backside of the piston is lost to oil temperature, while heat from the bore is lost to the average coolant temperature entering and exiting the block structure.

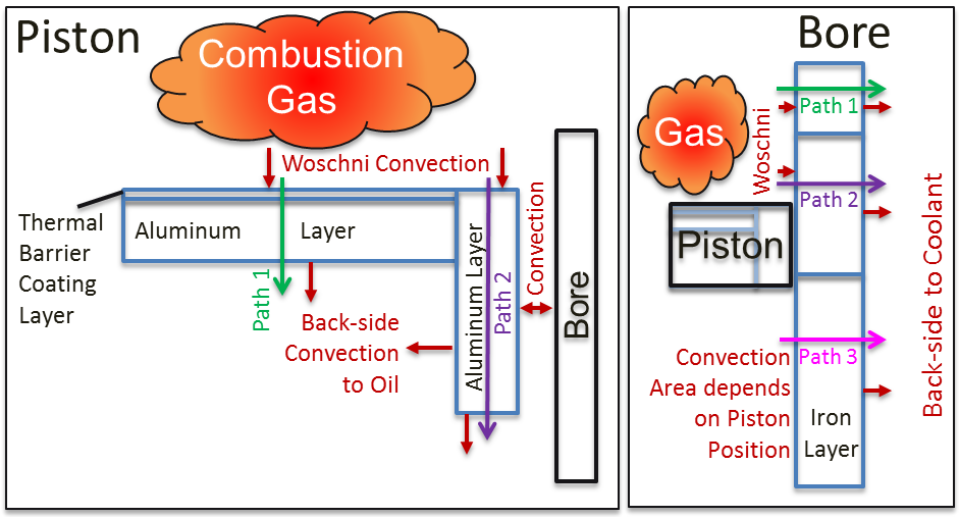

Figure 4-3: Piston and Bore 2D Component, Path and Layer Depiction

Heat transfer geometries to the valves and head are more complex, and required many more variables to create a reasonable facsimile of reality. An example of the

valve and head geometries is shown in Figure 4-4. The valves experience convection from the combustion gas on their faces and conduction up the valve stem to the valve guide, but also have intermittent convection through the valve edge to the valve seat (when the valve is closed), followed by a strong increase in convection to the valve backside as the valve opens and gas flows across it. Combustion gas properties are used for flow out of the combustion chamber, while port gas properties are used for flow into the engine. For simplicity, convection between the gas on the backside of the valve and the valve surface only occurs on the back of the valve head, not on the stem. The back of the valve head represents most of the valve surface area exposed in the exhaust port, and all of the calibrations were done with this assumption to ensure that the resultant heat transfer between exhaust gas and valves was correct. The head experiences convection from the combustion gas and intermittent convection from both valves, as well as convection to the average coolant temperature into and out of the head from its backside.

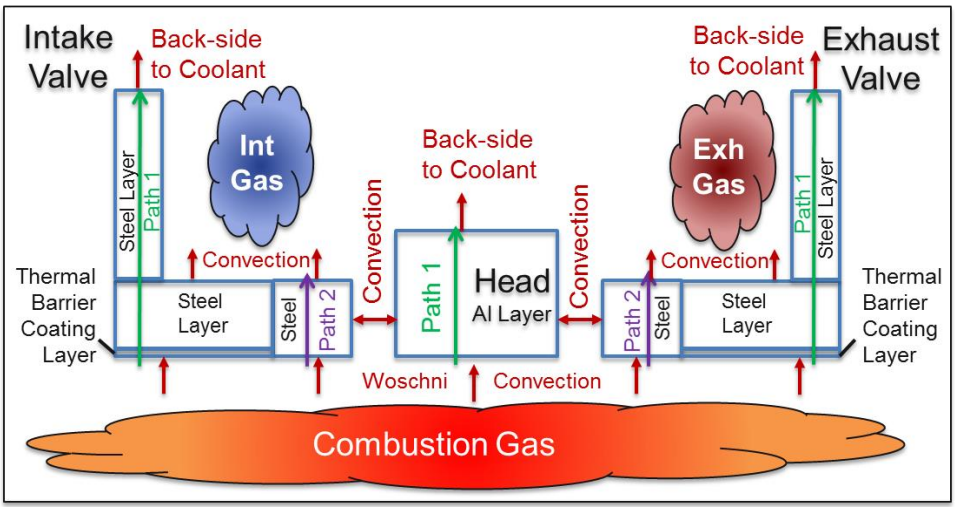

Figure 4-4: Valves and Head 2D Component, Path and Layer Depiction

The surface temperature of a layer was specified as the surface temperature of the exposed first or last element, which was calculated from that element's properties at the node and heat flow between the surface and the node using a quasi-steady approximation. This is correlated to the way that conduction and convection are described in Equation 4-2. Essentially, within each time step the heat transfer from the element surface to the center is assumed to be steady. This allows the surface temperature at the current time step to be calculated from the conduction equation assuming the quasi-steady conduction heat, material thermal properties and temperature of the node. This method allows for fewer, larger elements to accurately track the surface temperature swing throughout the cycle while improving computation time. This is shown in Figure 4-5, where calculation through this technique for a hypothetical highly-swinging wall allows the surface temperature to

converge on the final value with 10 evenly spaced nodes within the top layer. When the top element's node temperature was used, neglecting this method, 20 evenly spaced elements still did not capture the stabilized temperature swing as shown in the plot to the right.

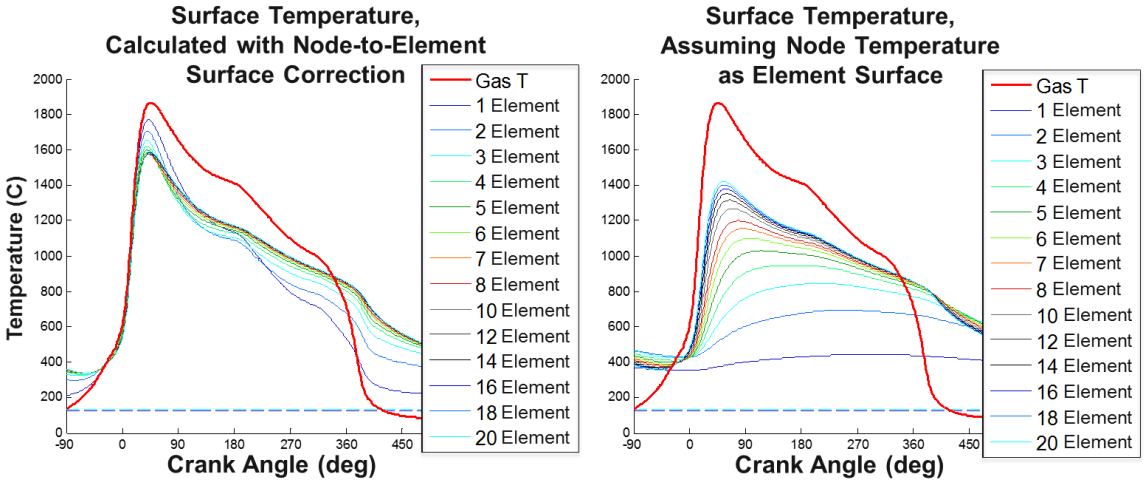

Figure 4-5: Surface Temperature Compensation Results vs. Node-as-Surface Temperature Assumption

The calculated surface temperature of large finite elements (demonstrated by low numbers of elements in the above figure to the left) exhibits over-prediction of the temperature swing, driven by the peaky cyclical nature of heat transfer from combustion gas to the wall. This is because the quasi-steady approximation breaks down as the distance between the element surface and node grows too large, allowing unrealistic amplification of the predicted wall temperature swing based on the instantaneous heat flux. The number, size, and location of elements near a highly transient surface such as the combustion chamber wall or valve head backside is critical to accurate prediction of wall temperature.

4.3.2 Optimal Finite-Element Organization

An understanding of the nature of the temperature swing within the wall is necessary to construct a robust method for assigning the finite element sizes and meshed locations in a highly transient heat transfer environment. A relationship between intrinsic material properties and cyclic frequency had been utilized by (Assanis & Badillo, 1987) to estimate the depth that a temperature wave will propagate within a continuous material. Fundamentally, the depth at which temperature waves due to a cyclical heat flux have decayed to 1% ($depth_{1\%}$) of their surface amplitude can be expressed by this relationship as shown in Figure 4-6. A cyclical transient heat flux representative of in-cylinder heat transfer at 2000 RPM has been applied to the surface at 0 mm depth and a constant thermal sink was applied at the backside at a

depth of 10 mm. The solid red and blue lines in the plot show the temperature throughout the material at the time of the maximum and minimum surface temperature, respectively, and the grey shaded area is the total range that material at a specific depth would swing through over the cycle. The temperature profiles at the times of maximum and minimum surface temperature highlight that the thermal energy travels through the material as a wave, with local maxima and minima dependent on previous cycles.

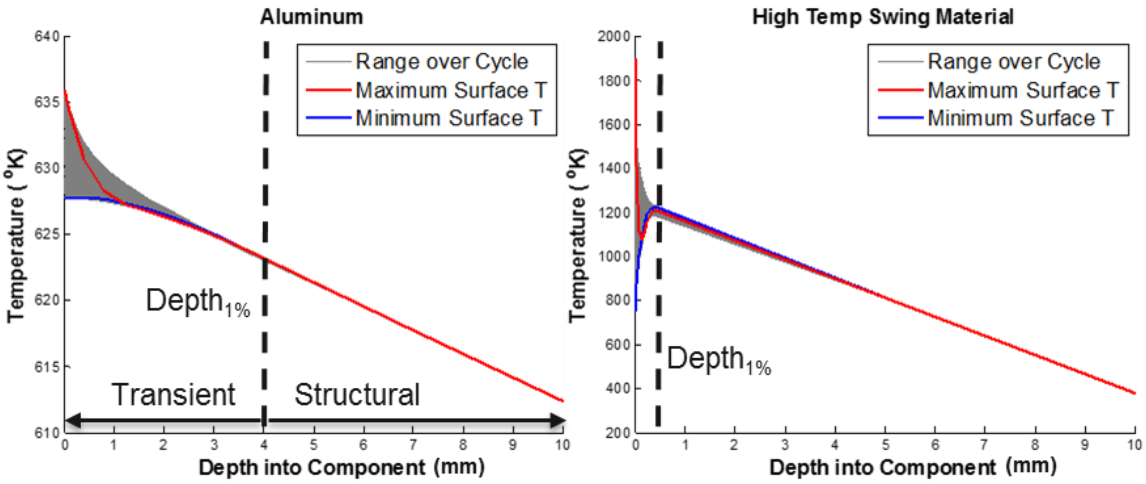

Figure 4-6: Analytical Solution of the Decay of Temperature Swing with Depth in Continuous Material

This critical $depth_{1\%}$ relationship is comprised of the square root of the ratio of the diffusivity over the cyclic frequency, as shown in Equation 4-3 with a multiplicative constant of 2.0 added to fit the equation to the modeled results. Despite widely varying thermal properties and effective engine speeds of the heat flux, the $depth_{1\%}$ is captured consistently using this method. The portion of the material closer to the surface experiences much greater transient temperature swings throughout the cycle, while material beyond the $depth_{1\%}$ primarily contributes to the structural thermal environment through conduction alone.

$$\boldsymbol{depth_{1\%} = 2.0 \times \sqrt{\frac{\kappa}{f}} = 2.0 \times \sqrt{\frac{60 \times n_c \times k}{\rho \times c \times S_{eng}}}} \qquad \textbf{Equation 4-3}$$

κ is the thermal diffusivity, and *f* is the frequency at which the temperature profile repeats. Both the thermal diffusivity and the frequency are broken apart into their contributing fundamental variables for an internal combustion engine, such as the thermal conductivity (k), specific heat capacity (c), density (ρ), engine speed (S_{eng}) in rpm, and the firing frequency (n_c) in revolutions/cycle. The $depth_{1\%}$ is very important in the design of parts that include thermal barrier materials with temperature swing properties.

The depth$_{1\%}$ described above was used as a basis for optimizing the element mesh, which dictated the inclusion of the factor of 2 in the above equation. This constant was necessary to relate the output of the relationship directly to the depth at which 99% of the surface temperature swing had decayed. A constant of 1.0 resulted in the depth at which only 90% of the surface temperature swing had decayed according to the analytical results, but the remaining 10% of temperature swing still present caused issues for element grouping into "transient" and "structural" regions. As Equation 4-3 is currently formulated, the number of elements present beyond the depth$_{1\%}$ has no impact on the surface temperature profile because the heat transfer has degenerated to a temporally steady condition. Therefore, only a single element is assigned between this depth and the back edge of the layer for computational efficiency, assuming that the heat transfer coefficient on the back edge is constant. If the back-side heat transfer is also highly transient (such as for an exhaust valve that experiences hot, pulsating flow along its back face), then the back side also has elements assigned using the transient methodology. Effectively, this clusters the elements close to combustion chamber surface and other transient heat sources for precision, while sacrificing detail in the deeper structure and the second dimension consistent with the goals of the model and lack of spacial accuracy of the heat transfer model from the gas to the walls. The arrangement of elements in the transient region is also based around this depth$_{1\%}$.

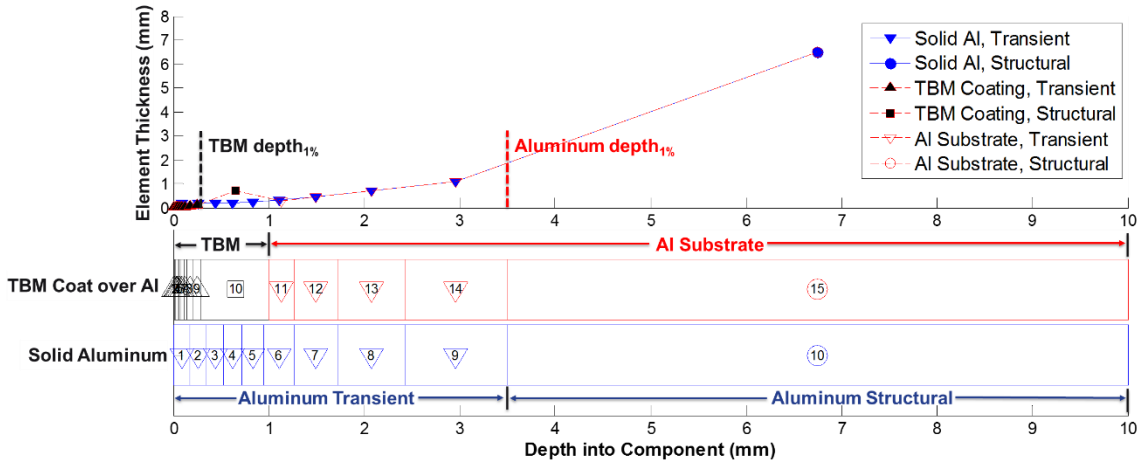

Figure 4-7: Optimized 1-Dimensional Finite Element Mesh for Layered Materials

It was found through experimentation that the first element next to a surface with transient heat flux could be no greater than 1/20th of the depth$_{1\%}$ without sacrificing precision. The remaining transient region needed 8 elements or greater to maintain precision, with better results when the elements were clustered more closely to the surface. A total of 10 finite elements for a material layer in contact with a cyclically fluctuating surface was necessary, with 9 of those as transient and one as structural. The element thickness is plotted on top in blue in Figure 4-7 for a single-material

aluminum component, and visually laid out with each element's edges and the centroid node marked in the bottom plot. The results presented previously in Figure 4-5 are representative of the errors incurred by including too few elements in the transient layer. Fewer elements are larger by necessity, which breaks down the quasi-steady approximation used to calculate the surface temperature.

Components that consist of layers of dissimilar materials, such as a hypothetical thermal barrier material (TBM) coating 1mm thick applied over the top of an aluminum substrate, have the finite element mesh in the coating layers replace the overlapped elements in the substrate layer. The TBM coating elements are shown in black, with the remaining aluminum substrate in red in Figure 4-7. Any elements in the substrate layer that are beyond the depth of the coating layer remain unchanged, such as elements 12 – 15 in the Al substrate. Since the TBM coating depth does not fall on an existing element edge, element 11 is interrupted and thus is thinner than the equivalent element 6 in the pure aluminum component. The intent of this arrangement was to preserve the accuracy of the results in instances when coating layers were too thin to damp out most of the transient temperature swing. In this example, the TBM has a much smaller $depth_{1\%}$ for the conditions due to its material properties, so the entire transient and structural collection of elements is fit within the 1mm coating depth.

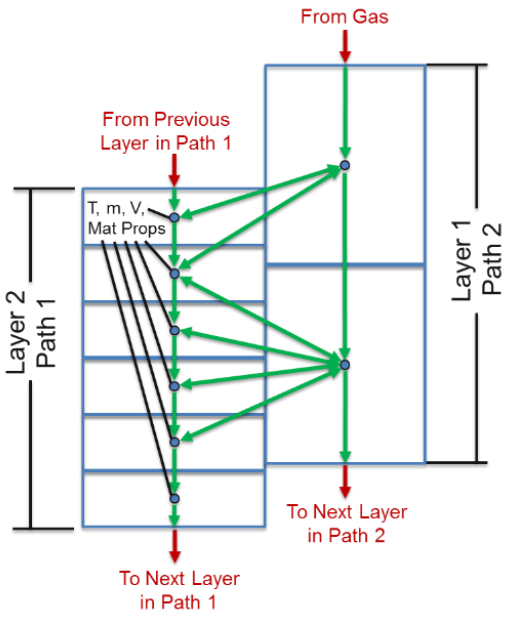

Figure 4-8: Heat Transfer Within and Between Paths in a Component

Variable element meshing complicates heat transfer between paths within a component. Conduction between nodes in different paths is established after the elements are assigned, based on whether the element edges overlap in depth from the surface as shown in Figure 4-8. The area and length necessary for calculating the amount of heat transfer between two nodes is calculated based on the gross component geometry, overlapping area between elements in different paths, and distance between nodes. For example, inter-path conduction in the piston would be between two paths at different average radii from the axis of symmetry, so conduction between paths must account for an increasing cross-section of material. Conduction between paths of the bore has a constant area because paths in the bore are arranged differently with respect to the axis of symmetry and the cross-section between paths remains constant.

4.3.3 Component Temperature Initialization & Solution

The way in which initialization is performed has a very large impact on the time it takes the model to converge on steady state, especially for materials that exhibit large temperature swings or have material properties that are more strongly dependent on temperature. First, representative temperatures, heat transfer coefficients, and other engine parameters must be calculated to provide the thermal load. If the wall temperatures are being calculated for a dataset where multiple engine cycles are available, then the representative data is calculated using a conditional ensemble average of crank-angle-resolved data. Of the 300 cycles recorded, individual cycles with an IMEP within 5% of the 300-cycle average and CA50 within 0.5° of the 300-cycle average were selected for inclusion in the conditional crank-angle-resolved representative temperatures and heat transfer coefficients. Typically, this included between 5 to 10% of the 300 cycles. Conditional averaging was performed to preserve the shape and rise rate of an individual cycle's cylinder temperature, convection coefficient, and thus heat transfer rate, while allowing a small amount of averaging to smooth noise and other inconsistencies. Conditional averaging is necessary for this type of data because the ensemble average of all recorded cycles, which include variance in CA50 and IMEP, will produce an average cylinder temperature curve that is much more rounded and dulled. Averaging cycles with varying CA50 has the effect of "smearing" the heat release out over a much longer time, which will appear as a much slower burn and in turn will produce a much longer period of slower temperature rise in surface temperatures, reducing the amount of temperature swing calculated. In cases where only a single cycle is available, such as from a thermodynamic engine simulation, data from this cycle is used as representative.

Once the representative thermal conditions are established, a steady, crank-angle-independent cycle-averaged solution is calculated from the average of all boundary heat transfer. This is repeated three times to ensure that the interpolated material properties converge for the calculated temperature. This step alone would be sufficient if just the steady-state, cycle-average wall temperature was desired for materials that did not exhibit much temperature swing. However, since the temperature swing itself will reduce the amount of heat transfer from a cyclic heat source in comparison to a wall at the constant average temperature of the swinging wall, the amount of temperature swing must be calculated as well.

Inter-cycle temperatures are then solved for as a function of crank angle using the representative cylinder conditions and the full cycle-resolved heat transfer equations including heat capacity. Two iterations of the cycle are solved to establish the amount of wall temperature swing. Because the wall temperature swing reduces the amount of heat transfer when compared to a constant wall temperature at the same average value, the total cycle-averaged heat transfer amount decreases from the steady-state

value. Therefore, the average component temperatures are initially calculated to be hotter than they should be when the wall temperature swing is accounted for. The iterative solver could continue to be used at this point to allow all the components to reach a new converged temperature, but this would take hundreds or thousands of cycles depending on the amount of temperature swing. Instead, the initially calculated amount of wall temperature swing is then incorporated into an adjusted heat transfer coefficient in the steady-state solution, which allows the correct, converged temperatures to be solved for. This wall temperature swing correction is performed for any surface that has cyclically transient heat transfer, including but not limited to the combustion chamber surface, valve backsides, valve to seat convection, and piston skirt to bore convection.

At this point the new temperatures which include the wall temperature swing correction are applied to the thermal model, and the iterative solver is run using the full equations and representative cylinder conditions. Iteration continues until all surface temperatures (including surfaces between layers within components) repeat between two consecutive iterations, within 0.05°C or 0.05% of the maximum surface temperature. This method for initialization reduces the number of iterative solutions for convergence from hundreds or thousands to typically fewer than 10, and results in converged temperatures less than 0.5°C different than the solution when the iterative solver is allowed to run to convergence without correcting for the wall temperature swing. These converged temperatures for a representative cycle can then be returned, or can serve as the starting point for a continuous solution of each cycle within a dataset. For all of the analysis performed in this paper, the representative temperatures are used for the entire dataset, as solving each cycle continuously is very time-intensive.

4.3.4 Wall Temperature Model Validation

The output of the full wall temperature model was validated against results from Abaqus, a commercially available thermal finite element software package. Abaqus was not used for the analysis itself because the Matlab-based solver could be more thoroughly integrated into both the thermodynamic modeling and the experimental data analysis routines, and because the solution time with Abaqus was considerably longer since the techniques for temperature initialization described above could not be implemented. The validation cases consisted of 1-dimensional heat transfer through 2 and 3 layered components while varying the layer thicknesses and material properties. The cylinder temperature and heat transfer coefficient were generated by the thermodynamic model at a high-load condition of approximately 20 bar IMEP, 2000 RPM. In all cases, the coating layer(s) are applied on top of a substrate representative of a 10mm thick piece of stainless steel, with the backside held at a constant 90°C. Results for the Matlab model utilize all of the down-sampling and

element meshing techniques described previously, and thus represent the operation of the full model as applied in prediction throughout this document.

The plot on the left in Figure 4-9 shows the agreement between models with a 2-layer component. The top layer is a hypothetical material with a thermal conductivity and heat capacity either 1/16th or 1/64th that of a typical zirconia oxide coating. It has a thickness of either 100µm or 200µm, as called out in the legend. Agreement between Abaqus and Matlab is excellent, and all of the general trends and magnitudes are well-captured by the Matlab wall temperature model. The right plot shows similar results, but with a 3-layer component. The top layer was a solid nickel cap of either 2µm or 5µm, laid over a 200µm coating of the 1/16th zirconia oxide coating, on top of the same 10mm stainless steel substrate. Further analysis of results like these will be performed in a later section to explain the trends seen in this plot.

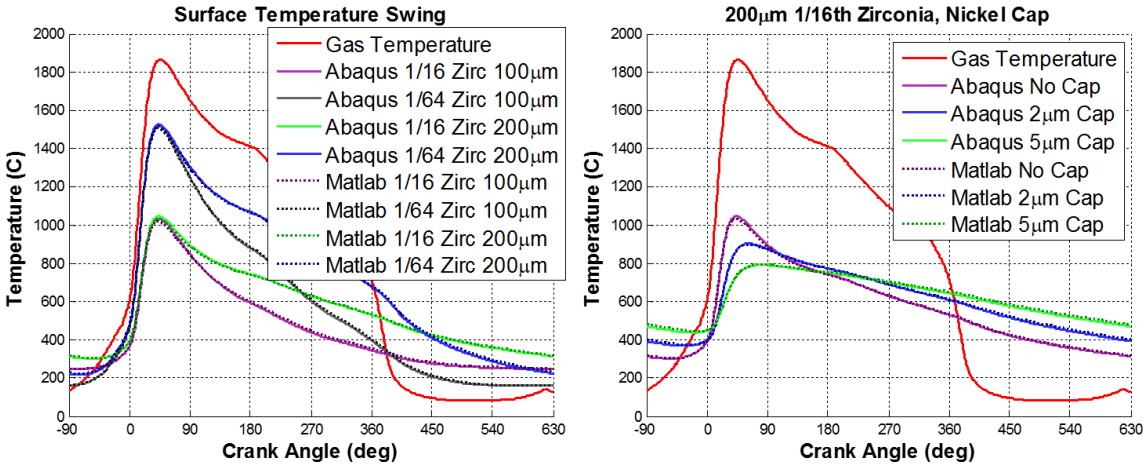

Figure 4-9: Validation of Wall Temperature Model with Commercially Available Software

4.3.5 Model Calibration with Experimental Data

Once the general model formulation was validated, the results were calibrated to experimental data where available. Heat transfer coefficients between components and to temperature sinks were the only parameters varied to get agreement with data. Heat transfer coefficients between the combustion chamber gas and the component surfaces, component geometries, and material properties were fixed.

Piston and head surface temperatures throughout the cycle could be compared to experimental data taken by (Guralp, Najt, & Filipi, 2012). The original measurements were obtained and processed using the same experimental routines described earlier in this paper for consistency. Woschni's heat transfer correlation was modified according to the method described in (Chang, et al., 2004) to make it applicable to homogeneous charge compression ignition (HCCI). HCCI is essentially controlled

autoignition, without a conventional flame front passing along combustion chamber walls. Therefore, the "pressure amplification" term in Woschni's correlation is turned off to reflect the absence of this contributing factor by setting its coefficient from 0.00324 to 0.

Surface temperatures at multiple points on the piston surface were measured using the same style of Medtherm coaxial heat flux probe used elsewhere in this research. The engine itself was very similar to the engine used in this research, with the same bore, stroke, family of pistons, Ricardo Hydra block, and lack of an under-crown oil cooling jet for piston cooling. The experimental piston surface had many facets designed to enable the HCCI combustion system, including a central bowl region with a thinner cross-section and a higher outside top-land area with a thicker cross-section. These facets were not incorporated into the thermal model beyond ensuring that the average piston-top thickness was accurate. Three of the heat flux probes were located within the bowl, and two were on the top-land. Test points with both piston and head measurements were limited due to the delicate connections between the piston heat flux probes and the data acquisition system. Four points were chosen for calibration, consisting of a speed sweep at fixed fueling rate and an additional point at higher fueling rate, shown in the plot on the right in Figure 4-10.

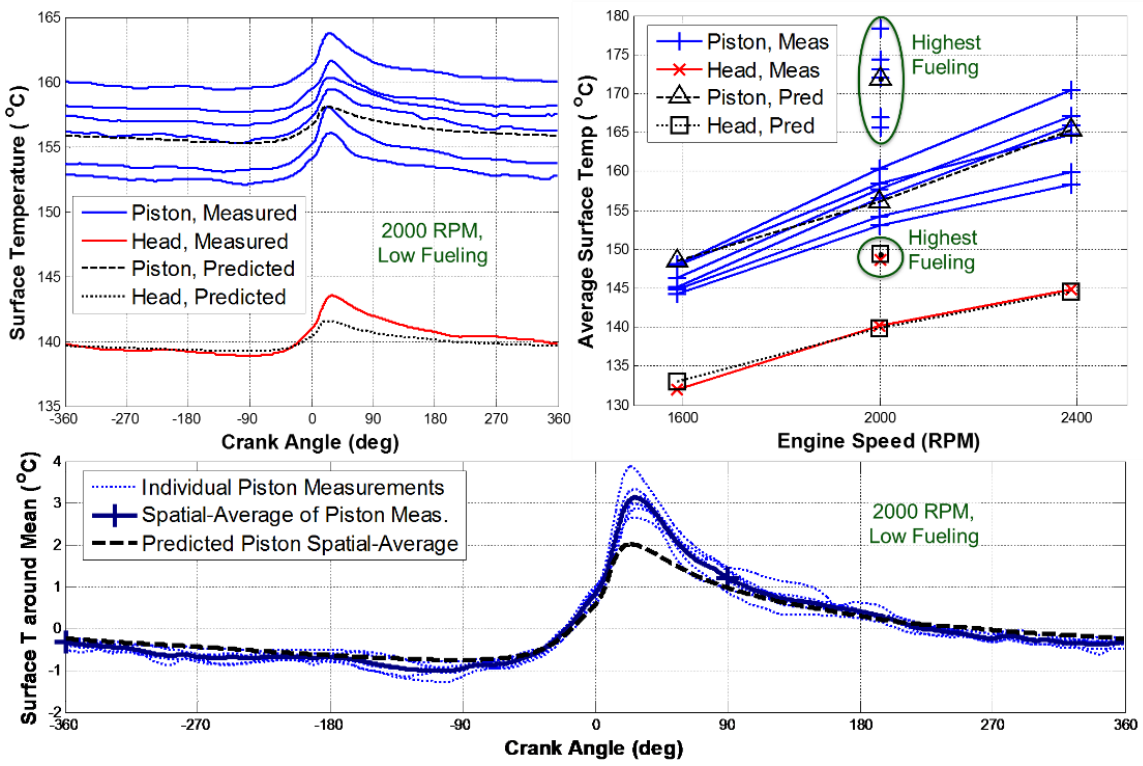

Figure 4-10: Thermal Model Calibration to Conditionally Averaged Crank-Angle-Resolved, Cycle-Averaged, and Spatially Averaged Piston and Head Measurements

The right plot shows the cycle-averaged temperature of the six piston surface thermocouples and the head surface thermocouple at all four points, as well as the model's predictions. The left plot shows the transient wall temperatures throughout the cycle at the 2000 RPM, low-fueling point. The model captures the average temperature for the head and piston well at all data points. The inter-cycle wall temperature swing predicted by the model is approximately half of the measured value, but this could be due to a number of reasons. Primarily, the modelled results only comprehend the mass and conditionally ensemble-averaged gas temperature and convection coefficient, and will not see the sudden spike that a physical probe mounted in the engine will experience as local fuel-air mixture combusts. Modifications to Woschni's convection coefficient as described previously for HCCI combustion will reduce the predicted heat flux spike by removing the pressure amplification term representing the flame front. However, because even HCCI combustion occurs over a finite temporal and spatial period due to thermal gradients in-cylinder, local measurements of wall temperature should be expected to see greater transient heat flux peaks than the area-averaged global heat transfer coefficient would predict. Comparing the absolute amount of temperature swing (maximum – minimum) reveals that the predicted temperature swing is only 55% of the swing of certain individual measurements, but the predicted swing is greater than 2/3rds of the spatially-averaged swing on the piston. No measurements were made in the bore wall surface, which would experience more retarded heat flux spikes in comparison to the piston and head. The effects of heat flux profile on the bore would further stretch the effective area-averaged heat loss rate that Woschni's equations attempt to capture, and therefore reduce the temperature swing calculated from them even further, lessening the difference between measured and predicted results.

Additionally, the temperature swing measured by the J-type thermocouples in the heat flux probes used could be biased by the iron central thermocouple element, as suggested by (Assanis & Badillo, 1989). Iron has approximately 35% of the thermal conductivity and 200% the volumetric heat capacity of Aluminum, which should result in 20% more temperature swing for a given heat flux profile. Proper design of the heat flux probe as dictated by the above reference should reduce this effect to less than 10%, but it will still bias experimental results with greater temperature swing. The specific aluminum properties of the head and piston may be different as well, due to the range of aluminum alloys and heat treatments, and their effects on primarily thermal conductivity.

Comparable experimental measurements of the intake and exhaust valve temperatures were found in the work by (Yang, Hamada, & Ohtsubo, 2000). The intake and exhaust valves in a 2.0 liter 4-cylinder naturally aspirated SI engine were instrumented with thermocouples in the center of the valve face and along the valve backside. The engine in this reference had a four-valve head and valves with solid

valve stems, similar to the engine used in the experimentation herein. Temperatures were measured at full load at 3600 and 5400 RPM. Other engine data was provided in this reference for these cases, which was used to help extrapolate experimental single cylinder results taken at comparable naturally aspirated full load points from 2000 and 3000 RPM up to the engine speeds presented in the paper. This allowed the calculation of engine boundary conditions including flow velocities through the valves in a consistent manner with other data taken in support of this project. The general formulation for the heat transfer coefficient between the valve back and the gas flow from (Yang, Hamada, & Ohtsubo, 2000) was implemented in the thermal model, and is shown in Equation 4-4.

$$h_{conv,flow} \cong Re^{0.58} \times (Lift/Radius)^{0.62} \times k_{gas}/Radius \qquad \text{Equation 4-4}$$

Re is the Reynolds number of the gas flow, k_{gas} is the gas thermal conductivity, and both Lift and Radius refer to the valve's instantaneous lift and representative port radius. The Reynolds number was calculated from the gas velocity (described in the Experimental Data Analysis section), and used the temperature-dependent dynamic viscosity of air. The gas thermal conductivity was also assumed to be equal to that of air. Temperature and density for the gas were taken from the cylinder at times when flow was out of the cylinder, and from the port for flow into the cylinder. A minimum convection coefficient between the gas within the port and the valve backside was specified, and both the minimum coefficient and the flowing coefficient of convection were adjusted with a single multiplier to calibrate the model to data in literature.

Convection between the valve stem and valve guide and between the valve edge and valve seat were calculated using the coefficients measured by (Wisniewski, 1998). The valve stem to guide coefficient was 1350 W/m^2-K, and the valve to valve seat coefficient was 15,000 W/m^2-K. A convection coefficient between the valve and valve seat on the high end of the measured range in the reference was chosen because SI engines typically can be run at higher speeds and need greater spring force to control the valve motion at those speeds, increasing the contact force and convection coefficient over diesel engines. Convection between the valve stem and guide was constant, while convection between the valve and valve seat was limited to the time when the valve was not open.

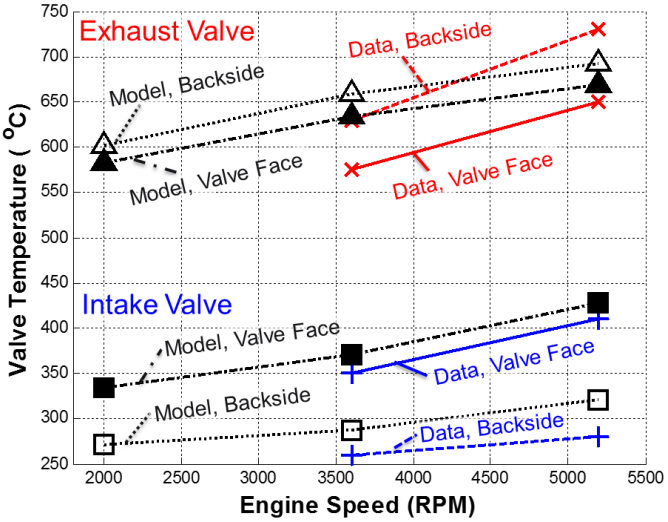

Figure 4-11: Intake and Exhaust Valve Calibration, using Spatially and Temporally Averaged Surface Temperatures

Agreement between the experimental data measured in (Yang, Hamada, & Ohtsubo, 2000) and the results of the thermal model and heat release analysis code was reasonable, given the number of assumptions that were made in generating the boundary conditions. Notably, the model predicts the recorded trend that the exhaust valve back temperature is higher than the valve surface temperature, which is driven by the high temperatures and rates of convection from the exhaust gas flow. Roughly 90% of the energy flow to the head takes place through the valve seat, as reported by (Wisniewski, 1998), and the general trends of temperature with speed are captured. The exhaust valve face and back temperatures were much closer to each other in the model because of the geometric simplifications of the valve, which confined all of the valve back heat transfer to the top of the valve head, and removed the radius between the valve head and valve stem. The model overpredicted the intake valve back temperature because fuel vaporization off of the back of the valve for a port-fuel-injected engine was not captured in the model. This factor was neglected because the experimental engine used for this project is direct-injected, and because characterization of the processes of fuel vaporization off the valve back such as the liquid fuel fraction delivered by the injector, fuel impingement and sticking rates were deemed outside of the scope of the thermal model. However for these examples, the difference between intake valve back temperatures of the model and data was equivalent to the energy required to vaporize approximately 20% of the fuel injected for these conditions.

4.3.6 Discussion of Thermal Wall Model

The thermal wall temperature swing model was developed to estimate the average temperature swing of a surface exposed to combusting gas in a reciprocating internal combustion engine. To enable comparison between measured experimental data and predicted simulation data, the thermal model utilizes a bulk gas temperature and convection coefficient derived from this temperature. As such, it prioritizes temperature effects on a surface that represents the average within the engine, with the underlying engine structure used to dictate the ease of heat loss to the coolant or the oil. Effects in the second dimension (parallel to the local combustion chamber

surface) are treated with minimal spacial precision because the form of the convection coefficient correlation that has been fitted to extensive experimental data does not support detail in this dimension. It therefore follows that the shape of the heat flux on the surface is dulled with respect to the heat flux that would be present at a specific point on the surface within an engine. This is alluded to in the analysis of the model calibration with respect to measured piston surface temperatures in conjunction with Figure 4-10, where the predicted temperature swing is only 55% of the temperature swing of individual measurements, but is over 2/3rds of the swing of the spatially-averaged temperature profile. In an engine operating with traditional SI combustion as opposed to HCCI as employed by (Guralp, Najt, & Filipi, 2012), the presence of a flame front sweeping across the chamber dividing burned and unburned mixture would increase the peakiness of convection at a specific position due to the sharper gradient between unburned and burned mixtures and thus temperatures and heat transfer coefficients. As long as the flame front travels more quickly than the component surface can warm due to conduction from another location, then the local temperature swing will be higher than predicted by the thermal model in its current iteration. Additionally, the temperature swing would be expected to be greater than noted in the measurements from Guralp due to the sharper gradient of SI combustion. Capturing this effect would require at least 2-zone in-cylinder temperature estimations, refinement of the convection correlations for multiple combustion zones, tracking of flame-wetted surfaces across components, and greater precision of the thermal model in the second dimension. Therefore, any predictions of temperature swing by the current thermal model will be conservative, as will the resulting effects on engine performance.

4.4. Coupling Thermodynamic & Thermal Models

The thermodynamic and thermal models were run independently due to the difficulty in integrating codes written in disparate languages. Wall temperatures were initially estimated for the first thermodynamic model iteration, and resulting cylinder conditions were passed back to the thermal model to estimate wall temperatures. This process was iterated until all surface temperatures had stabilized to within 0.1°C.

The commercial thermodynamic model only had 3 temperature zones available in total for the piston, bore and head. Therefore, the surface temperatures for all paths in each component had to be averaged, weighted by surface area. Furthermore, the intake valves, exhaust valves, and cylinder head were then area-averaged together to form the composite head temperature to be applied to the thermodynamic model. This area averaging served to dull the apparent temperature swing experienced by the composite surfaces, or of any insulated path that was part of a component that also contained un-insulated paths. The individual layer surface and node temperatures were saved external to the thermodynamic model for later reference,

and the instantaneous heat transfer rate from the gas to the walls was identical when calculated using individual surface temperatures and the composite temperatures. The restricted number of temperature zones in the thermodynamic model also limited the ability to accurately capture spatial thermal effects from burned vs. unburned gasses, so a single gas thermal zone was adopted for most modelled results to preserve consistency with the experimental data analysis output. Unfortunately, implementing a more integrated solution would have required a disproportionate amount of additional time for the improvement in solution accuracy.

4.5. Coupling Experimental Data Analysis & Thermal Model

The data analysis techniques presented in Section 3.5 were solved iteratively in series with the thermal model, since the wall temperatures must be known prior to beginning the porosity mass calculations, but can only be solved for after energy closure. Surface temperatures for all five components were calculated from the surface-area-weighted average of individual path temperatures within a component, and were used to estimate convection between the gas and engine structure. The porosity volume for permeable coatings was assumed to be evenly distributed throughout the coating depth, and therefore the porosity wall temperature was calculated as the temperature at each node throughout the coating, spatially averaged by the thickness of each element within the coating. Iteration between data analysis techniques and the thermal model was continued until all wall surface temperatures in subsequent iterations were within 0.1°C. When this constraint was satisfied, the convective coefficient energy closure multiplier α was generally changing by less than 0.1%, showing that the surface temperatures were the most sensitive element in the iteration process.

For simplicity, all of the heat transfer due to porosity was placed on the top node of the coating in the thermal model. The predominant term in the porosity heat transfer for permeable coating material properties was due to mass entering the porous volume, where it would encounter the top surface first, providing further justification for this decision. A sensitivity study was performed on how to apply the porosity losses, which compared them all assigned to the top node, assigned evenly throughout the coating accounting for the varying element thicknesses, or with a calculated distribution based on node temperatures throughout the coating. While there were some small differences noted between methods in the temperature profile throughout the coating and at the surface, the fundamental learnings, porosity losses and energy balances did not change significantly. However, the number of iterations required between the data analysis and thermal modeling was more than doubled when adding additional complexity to the porosity heat loss energy distribution.

4.6. Summary and Conclusions

A thermodynamic model and a thermal model were built, coupled, and calibrated to experimental data to enable predictions of the effects of various material properties on engine operation. The thermodynamic model matches un-coated experimental results with a high degree of precision. The thermal model was written specifically in support of this project and its predictions were validated against commercially available software. Furthermore, it captures effects noted in literature and recorded in experiments.

5. Analytical Material Properties Investigations

5.1. Introduction

Prior to engaging in experimental tests, it is necessary to understand the problem and explore the tradeoffs present in potential solutions. Analytical investigations were used to build further knowledge on the various effects of hypothetical material properties on wall temperature and heat transfer during different parts of the cycle for a fixed set of thermodynamic conditions. Then the interaction between the heat transfer and other engine processes such as work extraction, breathing, and compression was investigated as more realistic boundary conditions and thermal model geometries were included. This methodology enabled a fundamental understanding of both the theoretical and the practical concerns with implementing wall temperature swing materials in an internal combustion engine, and helped to guide the development of novel materials for experimental investigations.

5.2. Fixed Thermodynamic Conditions

The volumetric heat capacity and thermal conductivity of a material in contact with combustion chamber gas were independently varied over a rectangular matrix of points to map out trends in heat transfer. The same high-load gas temperature and heat transfer coefficient from the thermal model validation in Section 4.3.4 were used, and were kept constant despite changing wall temperatures and total heat loss rates for simplicity and computational speed. This point represents a roughly 20 bar IMEP condition at 2000 RPM with retarded combustion phasing for knock mitigation. This is a considerably higher load than the experimental testing will comprehend, primarily because the experimental testing on the single-cylinder engine is limited in load due to material thermal constraints of the piston and exhaust valves. Testing of options for additional component cooling would not have been possible in the time available for experimentation. However, for a temperature-swing material to be viable it must survive the higher temperatures that would accompany high load operation. It is recognized that as heat losses from the gas to the wall are reduced, the gas temperature will remain hotter, which will increase heat losses later in the cycle. Therefore the results of this study represent an optimistic prediction of the magnitude of the wall temperature swing for these conditions, and the effects of that

swing on heat losses. Results that include the coupling between wall temperature and thermodynamic performance are included in Section 5.3.

5.2.1 Model Formulation

The wall temperature was modeled as a simple 1-D geometry consisting of the variable material properties applied as a coating over a 10mm thick substrate with hypothetical properties similar to Aluminum or Steel. It was assumed that the coating and substrate were well-bonded, and thus there was no thermal contact resistance between them. The backside of the substrate was in contact with a 100°C thermal sink through a 1400 W/m^2-K convection coefficient. Initially, the coating thickness was specified as the depth at which only 1% of the temperature swing on the surface is still present (depth$_{1\%}$), and therefore also varies with the material properties through the relationship described in Equation 4-3. In further analysis, the coating thickness as a percentage of the depth$_{1\%}$ was also varied, as the balance between convection to the surface of the coating and conduction off of the backside of the coating towards the thermal sink is very important to the balance between heat losses during expansion and intake air heating during intake and compression. The resulting heat fluxes during different parts of the cycle were analyzed to estimate the overall effects on the engine. It is assumed that additional heat transfer from the walls to the gas during the intake stroke will hurt volumetric efficiency, during intake and compression will hurt knocking tendencies, and increased heat transfer from the gas to the walls during combustion & expansion will hurt IMEP and exhaust energy.

5.2.2 Analysis & Results

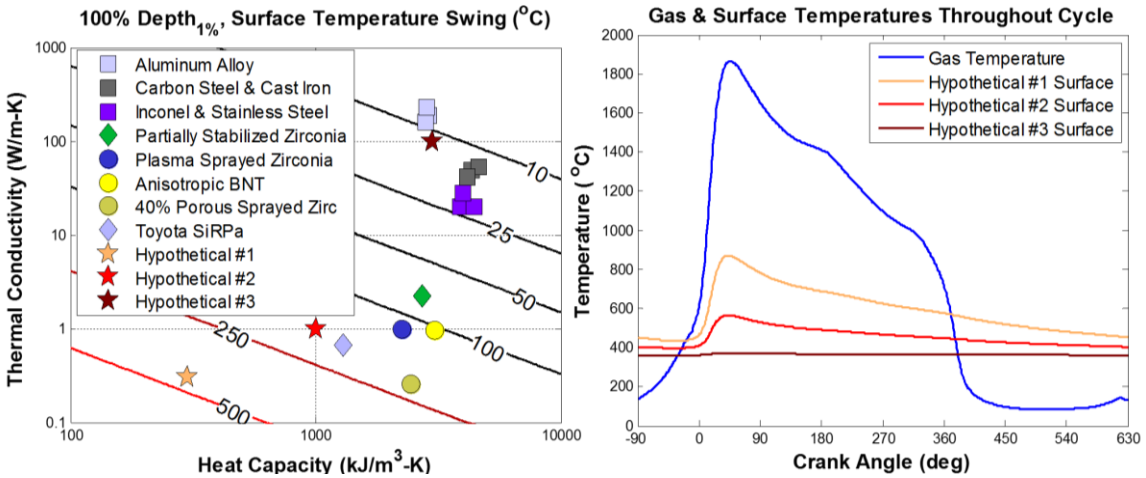

Figure 5-1: Surface Temperature Swing for Various Hypothetical Materials at 100% Depth$_{1\%}$

Initially, the thermal conductivity and volumetric heat capacity were swept over a wide range with a coating thickness equal to the depth$_{1\%}$ to allow the temperature

swing to fully develop. Contours of the resulting surface temperature swing, as well as the shape of the temperature profile throughout the cycle, are shown in Figure 5-1. As predicted by equations and calculations in literature, reductions in both heat capacity and conductivity increase the temperature swing. As long as the thickness of the temperature-swing material layer is specified as a function of the $depth_{1\%}$, reductions in either heat capacity or thermal conductivity are equally as effective at promoting temperature swing. The magnitude of the temperature swing in comparison to those references will be different, since the magnitude also depends on the gas temperature profile, gas-to-wall convection coefficient, and the frequency at which the temperature cycles. Three hypothetical materials were explicitly examined to gain further insight into the processes at play, with properties shown in Table 5-1. Hypothetical material #3 was chosen to give similar representative properties to solid metals, and hypothetical #2 was chosen to be similar to "state-of-the-art" temperature swing insulation like Toyota's SiRPa and highly porous sprayed zirconia. Hypothetical #1 carries these trends further to estimate the effects of desirable properties for a novel, highly porous insulating material.

Table 5-1: Hypothetical Material Thermal Properties

	Thermal Conductivity [W/m-K]	**Specific Heat Capacity [kJ/kg-K]**	**Density [kg/m^3]**
Hypothetical Material #1	0.3	1.0	300
Hypothetical Material #2	1.0	1.0	1000
Hypothetical Material #3	100	1.0	3000

Although the temperature swing increases as the hypothetical materials move down and to the left in the properties plot, the temporal-average temperature of the surface of these materials is also increasing. This will have the negative consequence of hurting the engine's volumetric efficiency, and promoting knock in homogeneous SI combustion systems. The average surface temperature is increasing because the equivalent thermal resistance is increasing as materials properties move in this direction. Drawing upon an electrical system analogy, the equivalent thermal resistance is the combined resistance to heat flow of the coating, the substrate, and the convection coefficient from the backside of the substrate to the temperature sink. Calculation of the equivalent thermal resistance is shown below in Equations 5-1 through 5-3. The total thermal resistance of our coating and substrate is the sum of the individual terms from conduction and convection of each layer, and is inversely proportional to the heat loss through the combined structure for steady heat flow conditions.

$$r_{equiv,Conduction} = \frac{d}{k} \equiv \frac{thickness}{thermal\ conductivity} \qquad \text{Equation 5-1}$$

$$r_{equiv,Convection} = \frac{1}{h} \equiv \frac{1}{convection\ coefficient} \qquad \text{Equation 5-2}$$

$$r_{equiv,Total} = r_{Cond,Coating} + r_{Cond,Substrate} + r_{Conv,Backside} \qquad \text{Equation 5-3}$$

The calculated thermal resistance of the entire coating and substrate, not including convection from the gas to the coating surface, is shown in the left plot in Figure 5-2. The coating properties do not have much effect on the total resistance for materials that are similar to the substrate, composed of hypothetical material #3 for this analysis. Lower conductivity and capacity both increase the conductive thermal resistance; conductivity increases resistance directly through the denominator in Equation 5-1 and capacity increases resistance indirectly through the $depth_{1\%}$, which appears in the numerator in that equation. The substrate conduction and backside convections are constants, which alone are approximately equal to 0.00078 m^2-K/W. The combustion-gas-side convection had an equivalent thermal resistance that varied between 0.016 and 0.0003, with a time-average of 0.005 m^2-K/W.

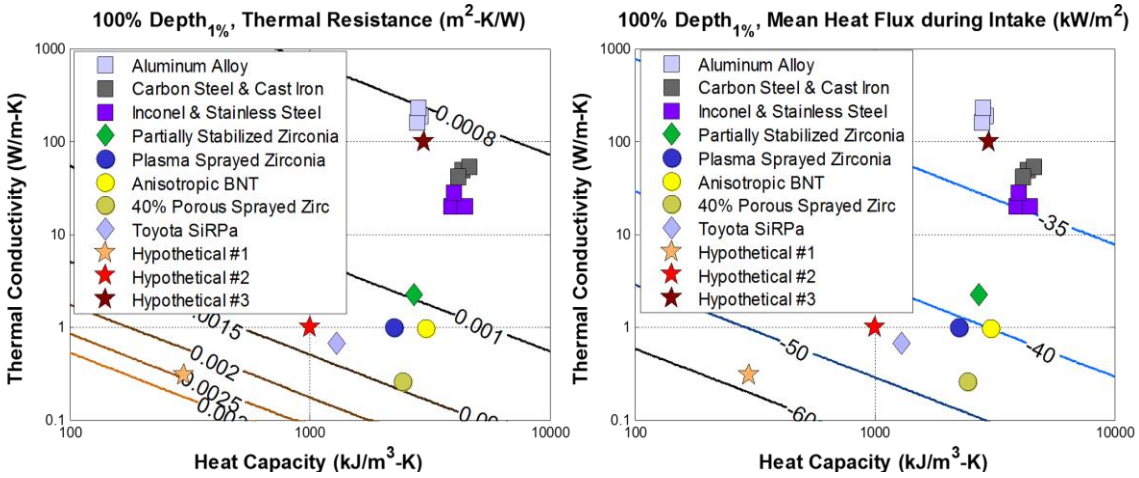

Figure 5-2: Thermal Resistance of Coating Layer and Heat Flux during Intake Stroke

The average heat flux from the gas to the walls during the intake stroke can be seen in the plot on the right in Figure 5-2. Greater thermal resistances with decreasing heat capacity and thermal conductivity contribute to increase the wall temperature during the intake stroke, which will heat the intake gas, reducing its density and hurting the engines volumetric efficiency. Other contributions to the thermal resistance must be examined to avoid this penalty of increasing insulation.

Reducing the thickness of a coating without changing the material's thermal properties will reduce the thermal resistance, and therefore could benefit the intake heat transfer. The plots in Figure 5-3 were generated using hypothetical material #1 while reducing the coating thickness to the specified percentages of the $depth_{1\%}$.

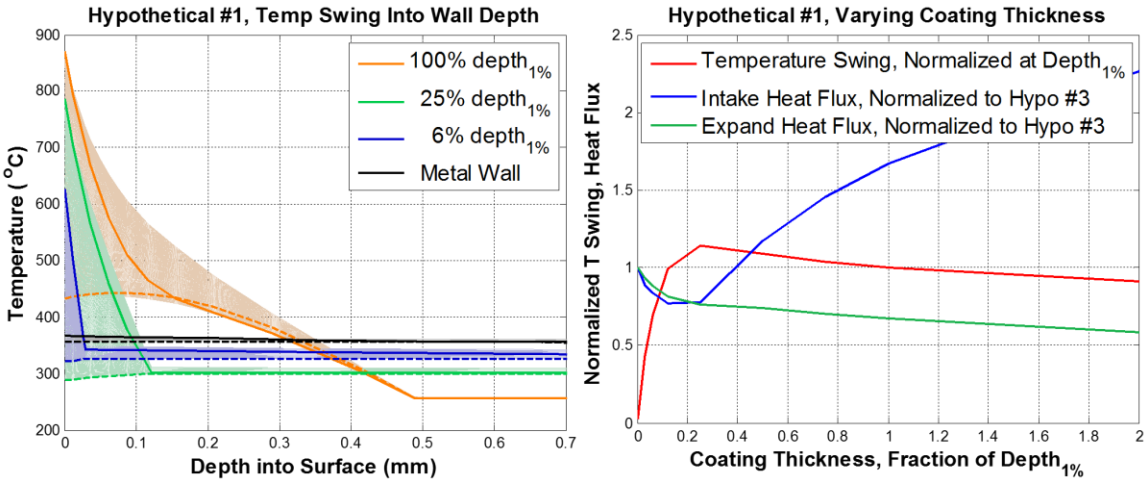

Figure 5-3: Effects of Coating Thickness on Temperature Profile throughout Wall Thickness, on Temperature Swing, Intake Stroke Heating and Expansion Stroke Heat Losses

The plot on the left shows the temperature swing as it travels through the depth of the coating before reaching the coating-substrate interface. The darker solid lines represent the temperature profile when the surface temperature is at its maximum, while the dashed lines show the profile when the surface is coolest. The shaded area for each color shows the entire range of temperatures experienced at each depth. Heat passes through the coating as a cyclical wave, with a phase delay between the surface peak and the peak at a given depth. This explains why the profile for the coolest surface temperature with the 100% depth$_{1\%}$ coating shows a local peak at approximately 0.1mm; the standing temperature wave that has developed in the coating has only penetrated 0.1mm between the previous peak heat flux and the occurrence of minimum surface temperature almost a full cycle later. Material at a depth greater than this point still experiences temperature swing over the course of a cycle, but the additional coating thickness beyond this point primarily contributes thermal resistance, increasing the average wall temperature with little effect on the amount of temperature swing.

The plot on the right in Figure 5-3 illustrates the total temperature swing at the surface of the coating as a function of the coating thickness, normalized by the temperature swing at 100% of the depth$_{1\%}$. It can be seen that the total temperature swing actually increases with decreasing coating thickness until 25% of the depth$_{1\%}$, at which point it begins falling rapidly. At 25% of the depth$_{1\%}$, the heat wave is essentially anchored at the point where the profiles for minimum and maximum surface temperature cross. The temperature swing is greater than for a fully developed temperature wave here because the temperature beyond this point cannot oscillate to the same degree as it could in a thicker coating due to the much higher heat capacity and conductivity of the substrate. Therefore, as the surface approaches the local minimum or maximum temperature, it is experiencing fewer effects from

the thermal inertia of the previous waves which actually increases the total minimum-to-maximum swing by 15%. Coatings that are thinner than this depth are overly constrained by the thermal inertia of the substrate, as demonstrated by the 6% $depth_{1\%}$ case. Heat flux during the expansion stroke is also shown in this plot normalized by the average heat flux using hypothetical material #3, which is the stand-in for a solid metal wall (shown as such in the left plot above and in Figure 5-4) and represents a logical, uncoated baseline. Expansion heat transfer initially decreases rapidly with thicker coatings as wall temperature swing is established. Beyond 25% $depth_{1\%}$, the rate of heat flux reduction slows because the temperature swing is relatively constant, leaving just the increased thermal resistance with coating thickness to drive lower heat losses during expansion.

The average heat flux during the intake stroke is also shown in the right plot in Figure 5-3, normalized to the uncoated hypothetical #3 baseline. As the coating thickness of hypothetical material #1 increases, the heat flux between the gas and the wall initially decreases, showing a reduction in intake charge heating from the wall. Beyond a coating thickness of 25% of the $depth_{1\%}$, the heat flux during the intake process begins increasing again, which would have negative repercussions on engine breathing. This shape comes about because of the temperature swing capability of the material, coupled with the total thermal resistance of the coating and substrate. As the coating increases in thickness from uncoated, greater surface temperature swing is achieved, which allows the minimum surface temperature to drop below the uncoated temperature and the substrate temperature. Additionally, the thermal resistance of the coating and substrate grows larger, which reduces the average heat transfer over the uncoated case, allowing the temperature at the interface between the substrate and coating to decrease. This combination of trends continues until the coating thickness reaches 25% of the $depth_{1\%}$, at which point the surface temperature swing has levelled off.

Beyond this point, the added coating thickness primarily increases the thermal resistance, which decreases the cycle-average heat transfer further by driving up the average surface temperature. Furthermore, additional thickness slows the temperature decay after the peak by allowing the effects of heat flux waves from previous cycles to affect the current cycle surface temperature. Both of these effects hurt the intake and compression stroke heat flux, as can be seen by the hotter surface temperatures prior to 0° and beyond 360° in the left plot in Figure 5-4. Ultimately, a coating thickness of 25% of the depth1% is ideal for minimizing heat losses from the gas to the wall during expansion while also minimizing the intake air heating, and represents the target thickness for coatings designed for four-stroke reciprocating internal combustion engines. This thickness is a balance between allowing enough thickness for substantial temperature swing to develop on the surface, while allowing

adequate cooling through the coating backside to the substrate so that the surface temperature decays to the un-coated surface temperature during the intake stroke.

The effects of lower heat capacity and thermal conductivity on the average heat flux during the expansion stroke are shown in the plot on the right. The effects of varying material properties on the expansion heat flux are small in the range associated with conventional metal alloys, but the rate of heat flux reduction increases dramatically as properties move to the lower left of the plot beyond the range of conventional insulating materials.

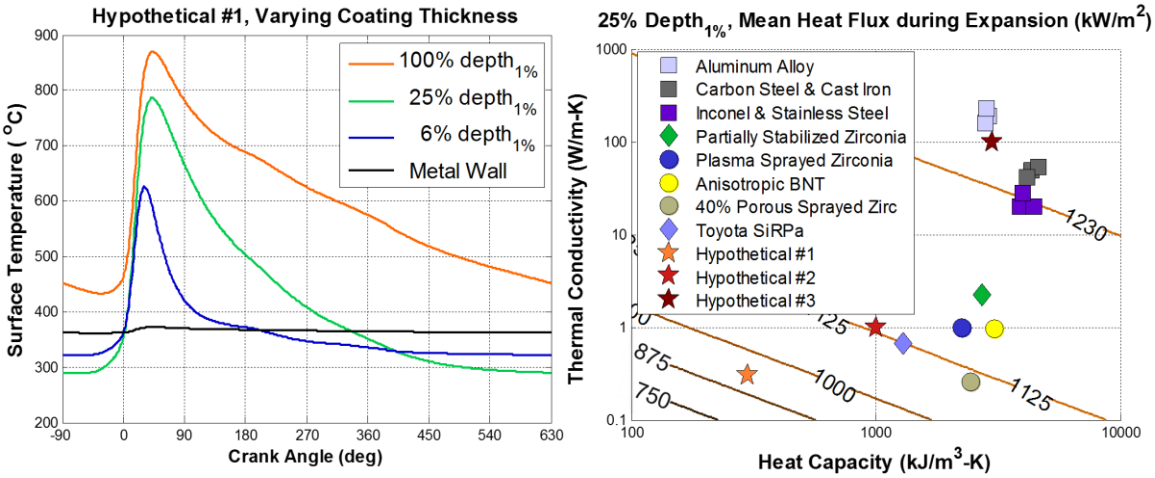

Figure 5-4: Coating Thickness Effects on Surface Temperature Profile, Effects of Material Thermal Properties on Expansion Heat Flux at 25% Depth$_{1\%}$ Coating Thickness

Fundamentally, these results are valid for any operating condition, since the depth that a temperature wave propagates into a material are only dependent on the material properties and the frequency of the cyclical heat flux. However, for a coating with fixed depth designed to work optimally at a certain frequency (engine speed), operation at a different frequency results in a different depth$_{1\%}$, and thus the fixed coating thickness would represent a different percentage of the depth$_{1\%}$. The inverse square root of the frequency impacts the depth$_{1\%}$, so slower operation will decrease the percentage, but not linearly. If a coating is applied at 25% of its depth$_{1\%}$ calculated at 2000 RPM, operation at 1000 RPM will make the fixed coating depth equivalent to 18% of the depth$_{1\%}$ at this speed, and operation at 6000 RPM would make the fixed coating 43% of the depth$_{1\%}$ at this speed. Therefore, at 1000 RPM, the heat loss during the intake stroke is slightly less negative (less intake heating), but the insulation is less effective during the expansion stroke. Conversely, at 6000 rpm, heat losses are lower during expansion, and heat transfer from the walls to the gas during the intake stroke is slightly higher than with conventional un-coated walls. This should have the effect of improving the engine's knock tolerance at low speeds while minimally penalizing volumetric efficiency at high loads, all while enabling maximum

temperature swing of the coating for reduced heat losses during combustion and expansion.

5.3. Variable Thermodynamic Conditions

A single-cylinder thermodynamic model similar to that which generated the fixed gas temperature and heat transfer coefficient was coupled to the thermal model to predict the effects of wall temperature swing on engine performance. This thermodynamic model is described in greater detail in Section 4.2. Three combinations of speed and fueling rate were investigated, as shown in Table 5-2; 2000 RPM and 60 mg/cycle (High-Load), 2000 RPM and 20 mg/cycle (Low-Load), and 1000 RPM and 20 mg/cycle (Low-Speed), with most analysis at High Load. Intake pressure was adjusted to maintain a constant air-fuel ratio of 14.2 (1% excess oxygen) for each point, and the exhaust pressure was kept at the maximum of 104 kPa or 10 kPa higher than the intake pressure. This would roughly simulate turbocharged boundary conditions while avoiding the more complex interplay between the turbomachine efficiencies, exhaust temperature, and engine volumetric efficiency, thereby simplifying the analysis and focusing on the in-cylinder effects. Combustion was modeled as a simple Wiebe function with CA50 fixed at 18° aTDC for the high load point, at 8° for the mid-load point, and at 12° for the low-speed point. The burn duration was held fixed at each point, specified as a function of the CA50. Heat transfer was modelled using the continuous form of the Woschni equations presented earlier, with a global multiplier calculated by an empirical formula fit to stoichiometric boosted SI data. This global multiplier was held fixed at each speed & fueling point.

Table 5-2: Analytical Engine Operating Points

	Low Speed	Low Load	High Load
Fueling Rate	20 mg/cycle	20 mg/cycle	60 mg/cycle
Engine Speed	1000 RPM	2000 RPM	2000 RPM
Intake Pressure	70 kPa	67 kPa	196 kPa
Exhaust Pressure	104 kPa	104 kPa	206 kPa
Exhaust Air/Fuel Ratio	14.2:1	14.2:1	14.2:1
CA50	12.0° $aTDC_f$	8.0° $aTDC_f$	18.0° $aTDC_f$
Approx. IMEP	6.0 bar	6.1 bar	16.0 bar
Approx. NMEP	5.6 bar	5.7 bar	15.8 bar

5.3.1 Simple Engine Geometry

The same simple one-dimensional thermal geometry was assumed for this comparison and the “Fixed Thermodynamic Conditions” study above. All combustion

chamber surface temperatures were set to the surface temperature value of the simple 1D solution. The heat transfer coefficient between the backside of the wall and the temperature sink was held constant at the value calibrated for a non-oil-jet-cooled piston. The layers of the simple wall used in the various cases is described in Table 5-3. Cases #1 and #2 represent a coating of hypothetical material #1 and #2 respectively over a solid metal substrate represented by material #3. The coating thickness was calculated as 25% of the $depth_{1\%}$ of the coating material, as described in the previous section. The total thickness of the walls for cases #1 and #2 is the same as for the baseline, which is made of only hypothetical material #3. Case #3 also consists of only material #3, but the thickness is increased so that the total conductive thermal resistance of the wall is the same as Case #1. Therefore, the comparisons presented by this analysis are of different materials used as an insulating coating within a constant thickness part (Case #1, #2, and Baseline), and the effects of equal amounts of insulation with and without wall temperature swing (Case #1 and #3).

Table 5-3: Simple Engine Geometry Wall Layers

Case	#1	#2	#3	Baseline
Coating Material	Hypo. #1	Hypo. #2	None	None
Coating Thickness	0.122 mm	0.122 mm	None	None
Base Material	Hypo. #3	Hypo. #3	Hypo. #3	Hypo. #3
Base Thickness	4.18 mm	4.18 mm	45.0 mm	4.30 mm
Comparison	Constant Total Thickness	Constant Total Thickness	Constant Resistance as #1	Constant Total Thickness

Thermal resistance was held constant between case #1 and case #3 to illustrate the differences in engine operation with insulating materials that encourage or limit wall temperature swing. For steady, constant heat transfer, both of these cases would produce the same heat transfer rate. The results for highly transient cyclical boundary conditions, such as those that exist within a reciprocating internal combustion engine, are considerably different.

Surface temperature results at the high-load point are shown to the left in Figure 5-5. All three cases reduced the amount of heat transfer when compared to the baseline, but the way in which they did it and the other effects that they had on engine processes were much different. The temperature swing on the wall surface for hypothetical material #1 is over 700°C, which is greater than predicted in the fixed thermodynamic analysis above. This greater swing is driven by a peakier heat loss rate in this comparison than in the fixed thermodynamic analysis due to the different pressure and temperature profiles of the gas. In a constant heat-loss scenario, walls of equal thermal resistance would have the same surface temperatures, and the heat

transfer rate would be constant between the two cases. This is not true for a cyclical heat source such as the gas in a reciprocating internal combustion engine. Materials that exhibit lower thermal inertia and can track the gas temperature more closely will still reduce the heat transfer over materials with little temperature swing, even when the total thermal resistance is constant. This is shown by the lower temporal-mean surface temperatures and heat transfer rates in the legends of Figure 5-5. Hypothetical material #1 reduced the peak heat transfer rate by almost 25 kW in comparison to case #3 while cutting the heat transferred from the wall back to the gas during the intake and compression process by approximately half. This resulted in a lower average surface temperature for case #1 than case #3, despite identical thermal resistances.

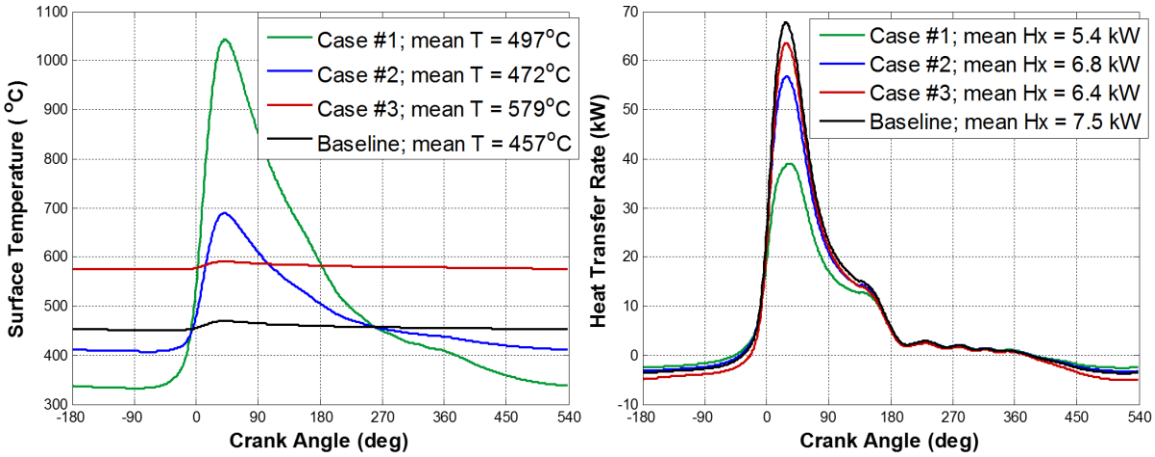

Figure 5-5: Surface Temperatures and Total Heat Transfer Rates at 2000 RPM, 60 mg Fueling Point

The observed temperature swing and resulting reduction in heat transfer for hypothetical material #2 are more modest than case #1 despite its thermal conductivity and heat capacity appearing closer to material #1 than to material #3 in Figure 5-3. (Assanis & Badillo, 1987) suggest that the expected temperature swing is proportional to the inverse of the square root of the product of the conductivity and the heat capacity, as described in Equation 1.1. A multiplicative scalar was applied to this proportional equation to capture the surface temperature swing predicted by the thermal model for material #3. When Equation 1.1 with the tuned scalar is applied to the other material cases, the thermal model results for material #1 only achieves 72% of the theoretically predicted swing while material #2 achieves 92% of the theoretical swing. The difference is explained by the effects of the wall temperature swing on the heat transfer rate; as the swing gets greater, the difference in temperature between the gas and wall and thus the peakiness of the heat transfer rate driving the swing decreases, which mitigates the increase in wall temperature swing with lower thermal material properties when compared to theoretical predictions against a constant thermal driver. These results also highlight the observation made at the end

of Section 5.2.2, that the wall temperature swing and its effects on the engine become more dramatic as material properties move away from conventional bulk insulation towards high-porosity insulation.

Figure 5-6 shows the differences in the total heat transfer rate for each of the cases in comparison to the baseline, and the effects on the combustion chamber gas temperature. The differences were plotted to highlight the effects of the different forms of insulation on the heat transfer process throughout the engine cycle. Positive differences indicate that there was more heat transfer at that time from the gas to the walls for the specified case than the baseline, or that the gas in the specified case was hotter. At this operating point the temperature swing coatings in cases #1 and #2 have the desired effect of decreasing heat transfer and thus increasing the gas temperature during the expansion and exhaust strokes while reducing the gas temperature during the intake and compression strokes. Case #3 also reduced heat transfer during combustion and exhaust, but not to the same extent, and it increased the gas temperature during intake and compression. When the heat transfer rate of the baseline case was negative (meaning heat flowed from the wall to the gas), cases #1 and #2 made it less negative which resulted in less intake and compression air heating, while the much hotter wall of case #3 heated the gas more than the baseline during these strokes. Therefore, the temperature swing materials improved the engine's volumetric efficiency (VE) by 3.6% for case #1 and by 1.3% for case #2, which lowered the intake pressure requirement for a fixed air mass flow and thus kept the pressure lower during compression. Case #3 suffered a reduction in VE of 4.1% due to the hotter, less dense air in-cylinder.

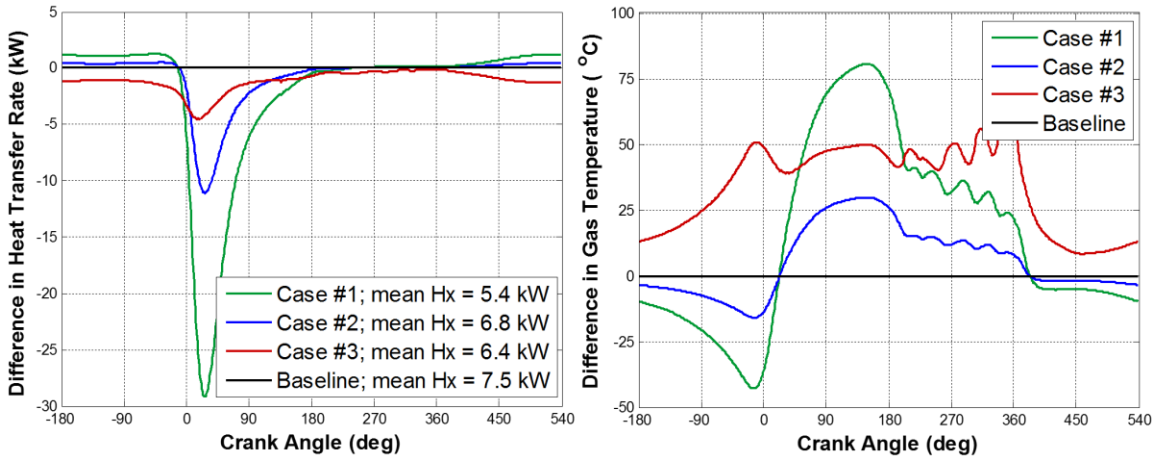

Figure 5-6: Difference in Heat Transfer Rate and Gas Temperature between Cases and Baseline

The effects on the gas pressure and instantaneous indicated piston work are shown in Figure 5-7. The overall shapes of the P-V curves are very similar, but cases #1 and #2 can be seen to be at a lower absolute pressure than the baseline for the entire cycle

except for the end of expansion, while case #3 is at consistently higher pressure than the baseline. Therefore the power required for compression for cases #1 and #2 was decreased, appearing as a positive in the right-hand plot of Figure 5-7 due to the difference. Conversely, case #3 required more work for compression. The greater pressure during expansion for all three cases is apparent as a positive difference in indicated power versus the baseline. This greater expansion power is barely sufficient to offset the compression losses for case #3, but is in addition to compression gains for cases #1 and #2. The differences during the gas exchange process are negligible because the exhaust pressure was pegged with a fixed difference to the intake pressure for this point. Notably, if the intake pressure was fixed instead of controlled to hold mass flow constant, then the differences would be seen almost exclusively in the expansion stroke but the results would be muddied due to different AFR or fuel energy which would affect the gas temperature more significantly. It is apparent through these results that the temperature swing ability of case #1 is the largest contributor to a positive difference in indicated work with increasing insulation. Even case #2, which has approximately 1/3 of the thermal resistance of case #3 outperforms it in net indicated work despite having higher average heat losses.

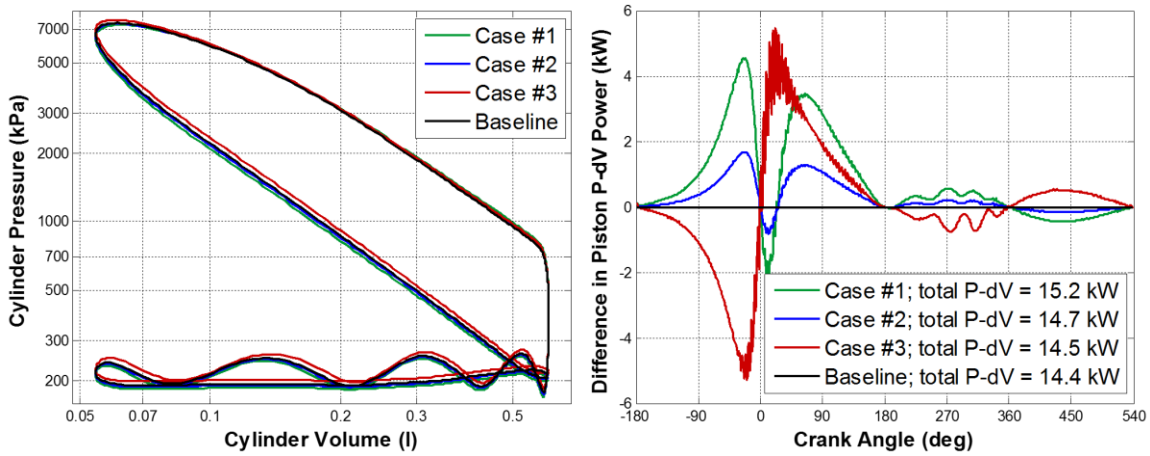

Figure 5-7: Logarithmic P-V and Difference in Instantaneous Indicated Piston Power from Baseline

The combination of temperature swing and increased thermal resistance decrease heat losses when using a coating of material #1 by 150 J in comparison to the baseline during the expansion stroke, of which 45.5 J is recovered by the piston. A coating of material #2 prevents 55 J of heat loss during expansion and allows piston recovery of 16.5 J of that energy. Case #3 decreased expansion heat losses by 30 J, but only recovered 4.5 J with the piston due to the increased compression work. The rest of the energy prevented from leaving the gas remained in the exhaust, for an increase of 39.3°C for case #1, 14.4°C for case #2, and 28.6°C for case #3. Overall the NSFC has improved by 4.9% for a coating of material #1, by 1.9% for a coating of material #2,

and by 0.5% for case #3, not accounting for any changes in the pumping loop due to lower VE or higher exhaust temperature.

It can be concluded that a positive difference in heat transfer rate is desirable during the intake and compression strokes to improve the volumetric efficiency and reduce the compression work, in addition to any positive effects for SI knock mitigation. As expected, a negative difference in heat transfer rate is desirable during expansion and exhaust to improve expansion work and increase the exhaust temperature. More so, a reduction in heat transfer early into the expansion stroke allows for the most potential work extraction from the energy since the piston still has the majority of the expansion to perform, allowing the greatest positive change in volume over which to increase piston work as discussed by (Morel, Fort, & Blumberg, 1985) with the concept of "Pumped Heat". Therefore, the greater the temperature swing potential of the material, the greater the conversion of gains from insulation during expansion to indicated work; otherwise most of the energy is left in the exhaust stream.

5.3.2 Realistic Engine Geometries

The complete engine thermal model including all components was employed for this study, using the geometries and backside heat transfer coefficients calibrated to experimental data as detailed in Section 4.3.5 unless otherwise specified. The piston top surface and intake and exhaust valve faces were modeled as coated, using the same materials and thicknesses as in Table 5-3, while the piston skirt and valve stems were uncoated and unchanged from the model formulation as it was calibrated. Case #3 was not simulated, as the extreme component thicknesses were not realistic. The cylinder head and the bore were not coated, and held constant as material #3 with no adjustments throughout this study since the piston and valve faces comprise almost 70% of the combustion chamber surface area at TDC. Initially, the same operating condition as the above section is analyzed to describe the differences due to engine geometry. Finally, the results at all three described operating conditions are examined.

The surface temperatures for the piston and the exhaust valve face are shown to the left in Figure 5-8. The exhaust valve surface had less temperature swing than the piston surface despite having the same material properties for each material cases because flow of the exhaust gas over the backside of the valve presents a competing cyclical heat addition to the component partially out-of-phase with the heat flux from the combustion chamber. The temperature wave from the valve backside travels through and destructively interferes with the surface temperature swing, lessening the magnitude of the surface swing. Furthermore, the temperature of the exhaust valve is higher due to the heat transfer from the exhaust gas flow, which reduces the rate of heat transfer from the in-cylinder gas during combustion, decreasing the

peakiness of the heat flux profile on the exhaust valve faces. The intake valve temperature profiles were largely the same as the piston profiles since heat transfer between the valves and the intake flow did not represent as much of a departure from the in-cylinder heat transfer conditions. The intake valves were an average of 40°C lower than the piston surface since the intake air sink temperature was cooler than the oil and coolant temperature. Additionally, the average piston temperatures (shown in the legend) are lower than the wall temperature from the previous section despite having the same back-side heat transfer coefficient to the oil because of the additional area exposed to the oil heat sink by the piston skirt. A heat transfer path from the piston to the bore has also been added as part of the realistic engine geometry, and the bore and head had much higher heat transfer coefficients to the coolant than the simple engine geometry component had, befitting forced fluid-wall convection.

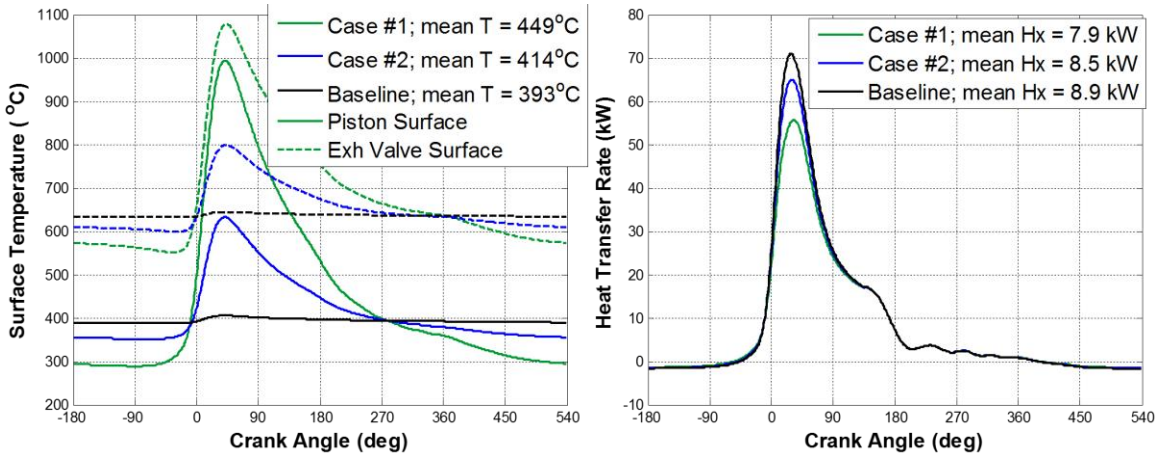

Figure 5-8: Surface Temperatures and Total Heat Transfer Rates for Complete Engine Geometry

Overall heat transfer rates from the gas to the coolant were not as different between material cases as in previous sections because only a portion of the combustion chamber surface was insulated. Near TDC when heat transfer was greatest, the coated surfaces represented over 60% of the exposed surface area, and the wall temperature swing contributed to reducing the peak rate. Other times in the cycle had more bore area exposed and the coated surface temperature was similar to the un-coated temperature, both of which reduced the differences in heat transfer rate. Heat loss during the expansion stroke was reduced by 66 J and 24.5 J for cases #1 and #2 in comparison to the uncoated baseline, while piston work was increased by 21.7 J and 7.9 J respectively. Roughly 1/3 of the heat prevented from leaving the gas during expansion is still recovered by the piston, but the total magnitude of these energies is approximately half versus the previous comparison where all the walls were coated.

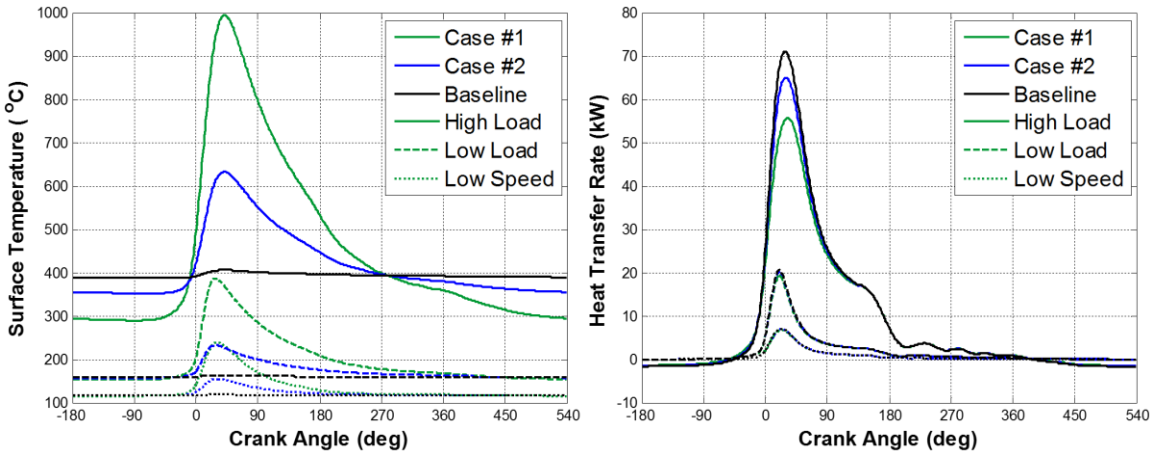

Figure 5-9: Piston Surface Temperatures and Total Heat Transfer Rates for All Points

The differences between material coatings is most pronounced at the high load point, shown for the piston surface as solid lines in Figure 5-9. Wall temperature swing is still noted at lower speeds and loads, but it is reduced since the fuel energy and thus heat transfer rate driving the swing is diminished. The wall temperature swing for cases #1 and #2 at the low speed 1000 RPM point also decay more quickly, returning to the baseline temperature sooner than the low load point. This is because the coating is fixed at a specific thickness, determined by 25% of the $depth_{1\%}$ at 2000 RPM. Lower engine speeds will increase the characteristic $depth_{1\%}$ for a material, therefore the effect of lower engine speeds on a fixed thickness coating are to reduce the percentage of the $depth_{1\%}$ that the fixed thickness coating represents. This explains why the surface temperature decays more quickly at the 1000 RPM low speed point than at the 2000 RPM low load point at the same fueling and similar IMEP.

The smaller wall temperature swing for the low load and low speed points is reflected in the difference in peak heat transfer rate between the three materials. At low speed there is only 1.7 J difference in total heat transfer during the expansion stroke from the baseline for material #1 and 0.5 J for material #2, as shown to the left in Figure 5-10. Heat transfer for the low load and speed cases is also essentially zero outside of the expansion stroke. This basically eliminates the differences in temperature seen during the intake and compression strokes since the coating has sufficient time to cool through conduction to the underlying substrate and reach similar temperatures to an un-coated component without heat flux through the combustion chamber surface. At these speeds and loads there should be no impact on VE expected; however this is not a bad thing since these points are throttled and any increase in VE would need to be accompanied by greater throttling which would impose a greater pumping loss on the engine.

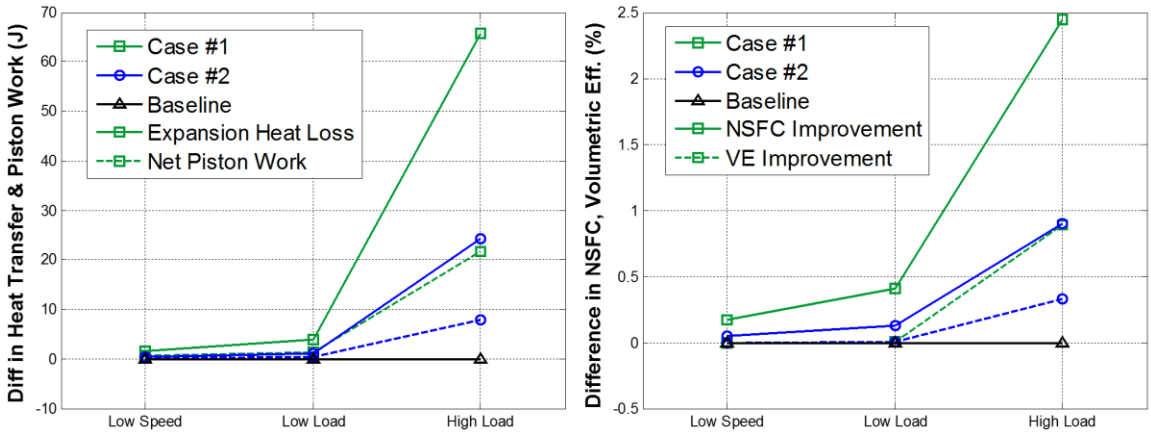

Figure 5-10: Differences in Energies, NSFC and Volumetric Efficiency for All Points from Baseline

As observed before, the high load operating point demonstrated the largest difference between the coating materials. The low load and low speed points did not allow the coatings to prevent much additional energy from leaving the gas, and therefore the differences in piston work and thus NSFC are very small for these points. Consistently, almost 1/3 of the additional energy not lost to the walls during expansion was converted into net indicated work by the piston when using temperature-swing materials for all points. Volumetric efficiency was unchanged at low speeds and loads, and was actually improved at high load by these coatings, demonstrating that temperature-swing materials can have both a breathing and an efficiency benefit. Exhaust temperatures only varied by 1.5°C at the low speed point and by 3.2°C at the low load point. At the high load point, material #1 had 18°C hotter exhaust and material #2 had 6.5°C hotter exhaust than the baseline.

5.4. Summary and Conclusions

Thermal barrier materials that enable wall temperature swing show the potential to improve the performance of reciprocating internal combustion engines without negatively impacting engine breathing or knock tendencies.

- Low heat capacity and low thermal conductivity both promote surface temperature swing in combustion chamber wall materials. Equivalent percentage reductions in either volumetric capacity or conductivity will have the same net effect on the surface temperature swing and thus engine performance effects, assuming that the thickness of the coating is appropriately varied according to the $\text{depth}_{1\%}$ derived from the characteristic thermal depth.
- Coating thickness of a temperature-swing material has a large influence on the amount of temperature swing, the total insulation capability, and the rate of temperature decay during expansion and exhaust, which all will affect engine

performance. The ideal thickness to minimize the wall temperature during the intake stroke while maximizing the total temperature swing to achieve the greatest reduction in heat losses during combustion and expansion is approximately 25% of the $depth_{1\%}$. This thickness is a balance between allowing enough thickness for substantial temperature swing to develop on the surface, while allowing adequate cooling through the coating backside to the substrate so that the surface temperature decays to the un-coated surface temperature during the intake stroke.

- Wall temperature swing in response to the engine's instantaneous heat flux can reduce heat transfer more effectively than conventional insulation without the traditional negative impacts on volumetric efficiency or in-cylinder thermal environment that have historically plagued adiabatic engine efforts.
- Approximately 1/3 of the energy prevented from leaving the gas during the expansion stroke can be recovered by the piston using wall temperature swing coatings, while conventional coatings force the engine to expend much of that recovered energy on additional compression.
- Greater benefits are found at high load where the heat transfer rates that drive wall temperature swing are highest.

6. Conventional Materials: Experimental Investigations

Introduction

Prior to developing a novel insulating material, conventional alternatives needed to be assessed for applicability. Anisotropic barium-neodymium-titanate (BNT – $BaNd_2Ti_3O_{10}$) was selected as a promising material for promoting temperature swing characteristics while maintaining adequate strength and adherence to the aluminum components it was applied to. The natural layering that was formed through the material structure and application process enabled a tailored coefficient of thermal expansion that could be matched to the underlying aluminum, while offering low-conductivity planes to reduce heat transfer through it and isolate the uppermost material to promote temperature swing throughout the cycle.

6.1. Conventional Insulating Materials

The environment that thermal barrier materials must survive within a reciprocating internal combustion engine is very demanding. Both the pressure and the temperature that they are exposed to cycle by orders of magnitude at a high frequency, which can quickly induce mechanical and thermal fatigue if not outright failure. In-cylinder flows and fuel sprays often directly contact the surfaces that the thermal barrier materials would be applied to, enabling erosion and increasing the chance of thermal shock. Oxygen is present, and products of combustion can often be acidic, encouraging oxidation. In addition, many of the components are reciprocating and vibrating, making for a very harsh environment.

Many types of in-cylinder insulation have been explored in literature and prior work. Plasma-sprayed zirconia-based coatings have tended to be the most popular in recent times because they can survive the in-cylinder environment, and are relatively easy to implement over existing parts. Zirconia-based materials can be stabilized with yttria or other elements to improve strength and better match the coefficient of thermal expansion with aluminum or other metal surfaces that they are applied to. Plasma-sprayed zirconia coatings have a low thermal conductivity of approximately 0.5 – 2 W/m^2-K, which is less than $1/10^{th}$ of materials like steel and iron, and $1/100^{th}$ of aluminum. These properties are achieved partially because of the porosity inherent

in the plasma-spraying process, which can create a total void volume of 10 – 40% of the total coating volume.

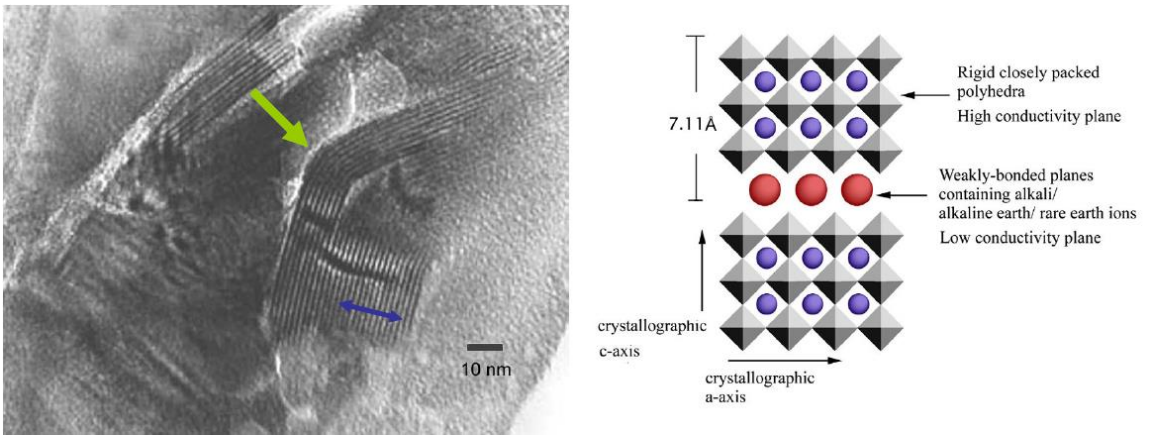

Figure 6-1: Crystalline Structure of a sample of Anisotropic BNT Material, from (Applied Thin Films Inc., 2011)

Other plasma-sprayed ceramic coatings are available that could offer greater performance than zirconia. A BNT material was chosen for experimentation due to some unique properties that it exhibits. BNT is a layered perovskite that has an anisotropic crystalline structure that introduces planes of low thermal conductivity into the material, as shown by the layers across the blue arrow in the transmission electron micrograph image shown in Figure 6-1. The angle of these planes can be tailored during the application process to match the coefficient of thermal expansion between the coating and the metal substrate to promote better bonding and reduce thermal stresses as the component heats and cools. The resulting structure was reported to be very compliant to externally imposed stresses, shown by the bend in structure highlighted by the green arrow. The thermal conductivity and heat capacity of the plasma-sprayed BNT material was comparable to plasma-sprayed zirconia coatings, shown in Figure 1-1. BNT had also shown durability as an insulating coating high-temperature oxidizing environments. (Applied Thin Films Inc., 2011) (United States Patent No. 7,838,121 B1, 2010)

Simulation of BNT as an in-cylinder insulating material was performed, and the $depth_{1\%}$ of its surface value was calculated to be 300μm. Coating depths of 300, 600 and 1200μm were chosen for experimental testing to attempt to record a range of reductions in net heat transfer at varying average surface temperatures. These target thicknesses were cut into the piston face, creating a pocket that the BNT could be applied into to preserve compression ratio and piston surface position. The BNT coating was created with a highly controlled plasma-spray process by Applied Thin Films, Inc. within the pockets of the pistons described above and shown previously in Figure 3-2. The actual coating thicknesses were measured before and after testing, and spatially averaged across the coated surface to 230, 500, and 1000μm

respectively, representing 77%, 167%, and 333% of BNT's $depth_{1\%}$. These thicknesses are greater than the ideal 25% of the $depth_{1\%}$ identified previously, but the pistons were coated prior to the conclusion of the modeling work. Nevertheless, they could still be useful in confirming the trends identified by the model. A second set of pistons were coated to the same nominal thicknesses at the same time, and the resultant measured coating thicknesses were essentially the same. Pictures of two of the coated pistons prior to being installed in the engine are shown in Figure 6-2.

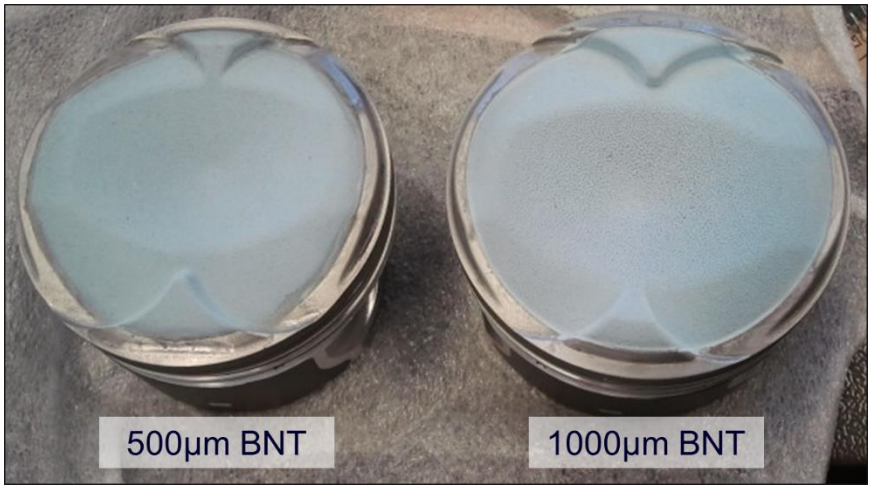

Figure 6-2: BNT-Coated Pistons Prior to Installation in Experimental Engine

No insulation was tested on the cylinder bore. The bore has minimal area exposed to the combustion gas near firing TDC when the highest temperatures and convection coefficients are occurring, and thus contributes the least to heat transfer at this critical time. Conversely, at BDC after the intake stroke, the bore area dominates in-cylinder heat transfer and has a disproportionate effect on the reduction of volumetric efficiency. In addition, the bore has tribological and durability constraints due to the need to seal the piston rings which would limit the area of application to above the top ring uppermost position. For these reasons, the bore was unmodified for all of these tests.

6.2. Test Plan

Two pistons of each coating thickness were tested in the single-cylinder experimental engine introduced previously. Each piston was run for a total of over 20 hours at varying speeds and loads prior to performing the measurements presented herein in order to reach a stabilized condition for the coating, piston sealing rings, and in-cylinder deposits. The results from one piston with each of the coating thicknesses are presented subsequently. In all cases, the other piston not shown performed very similarly, but was not shown for clarity, or to illustrate a point captured specifically in one hardware configuration. An ignition timing sweep was recorded at three load

points at 2000 RPM, defined by the fueling rates of 10.5, 21, and 31 mg/cycle. These aligned with roughly 3 bar, 6 bar, and 9 bar IMEP, evenly sweeping operation of a naturally aspirated SI engine. The target fuel rates were 10, 20 and 30 mg/cycle as described in the Experimental Methodology section, but errors in calculation that were uncovered after testing resulted in a slight offset that affected the entirety of the conventional materials dataset. This offset does not affect comparison of any of the data within this section, but is present between this section and Section 0.

6.3. Analysis and Results

6.3.1 Experimental Results

Experimental results were measured using the anisotropic BNT coatings applied to pistons at target thicknesses of 300, 600 & 1200µm. Actual coating thicknesses were measured at 230, 500 & 1000µm, so a reduction in compression ratio with coating thickness, without the inclusion of any porosity effects, was expected, presented as the "Expected" increase in clearance volume in Figure 6-3. However, the recorded drop in CR at the motoring control point was considerably more than expected. Motoring compression ratio and piston-top clearance volume measurements were repeated multiple times through different engine builds using the two different pistons with the same coating thickness, or through multiple builds of the baseline aluminum piston. The solid lines represent the motoring control point prior to testing but with the engine fully warm, while the dashed lines are the motoring control point taken after testing.

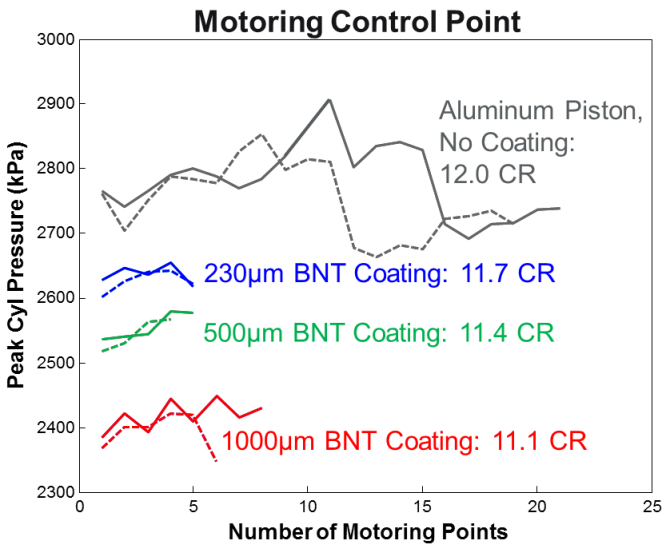

Case	Alum	230µm	500µm	1000µm
Measured	0.0 cc	+0.8 cc	-0.2 cc	+3.4 cc
Motoring	0.0 cc	+1.4 cc	+2.9 cc	+4.5 cc
Expected	0.0 cc	+0.4 cc	+0.6 cc	+1.1 cc
Porosity	0.0 cc	+1.0 cc	+2.3 cc	+3.4 cc

Figure 6-3: Reduction in Compression Ratio and Increase in Clearance Volume with Coating Thickness

The "Measured" reductions in compression ratio were obtained through static fluid displacement in a test fixture used to measure clearance volume changes due to piston surfaces. The 500µm coating piston was measured to have less clearance volume than the baseline aluminum piston – this result was repeated but could only

be explained with a combination of measurement errors due to improper piston seating in the fixture and optical measurement of the volume of fluid added to the fixture. Measurement error for this fixture is expected to be on the order of +/- 2 cc. It was speculated that the BNT coating was porous and permeable, that hot compressed air could more easily penetrate the coating than room-temperature water used in the piston surface test fixture, and that the motoring compression ratio most closely reflected the true TDC volume.

The difference between the expected TDC volume and the motoring TDC volume was assumed to be the porous volume within the BNT coating. This assumption is critical to the results presented in this work, and was carefully made after re-processing the data with a wide variety of other assumptions and comparing the results to other measured parameters. Ultimately, the assumptions presented here were compared to the measured heat flux at the cylinder head surface, a rough system-level energy balance using the measured coolant temperatures and flow rates around the cylinder head and block, the shape of the gross heat release during the closed portion of the cycle, and the energy multipliers estimated compared to historical data and other builds of the same engine.

Porosity of the coating was modeled in data analysis using the crevice model described in Section 3.5.2 as a sub-volume of the combustion chamber sharing the same pressure, but at the wall temperature. As gas pressure and temperature in the combustion chamber increased, mass was pushed into the coating porosity volume which was cooler and thus at a higher density. Heat loss from the gas entering the porosity volume was calculated using the assumption that the entering gas instantaneously reached the temperature of the porosity, which was justified by the estimated pore size and surface to volume ratio of the porosity. The pore size was roughly estimated as having an average equivalent diameter of approximately 0.05mm, based on the roughness and apparent size of the plasma-sprayed particles of the coating. This is similar to the piston-to-bore clearance that the crevice volume model conventionally models, but with a much more discontinuous shape due to the sputtered nature of the plasma-sprayed coating. Heat was also transferred between the walls and the gas as the walls changed temperature throughout the cycle, forcing the gas contained within to follow. Heat transfer to the porosity from these two sources was tracked and applied to the top node in the piston coating to simulate their effects on surface temperature. Wall temperature for the porosity was estimated as the thickness-averaged temperature of the BNT coating. It was necessary to use both this porosity model and the wall temperature solver to get physically possible results. Without using both the wall thermal model and the porosity model, non-real solutions were generated for many of the points with unrealistic heat release curves, zero or negative convection, or compression ratios that varied with load and speed.

The results of this heat release analysis using the porosity and thermal models is shown in Figure 6-4. All three coating thicknesses were analyzed alongside the un-coated piston at three loads and 2000 RPM. Combustion phasing at 50% mass fraction burned (CA50) for all points at a load was matched as best as possible, although knock prevented the thickest coating from duplicating the combustion timing of the other cases at the highest load. The energy closure multiplier (α) applied to the convection coefficient is displayed in the legend for all datasets. The top set of solid lines, denoted as "Fuel in Comb. Chamber", are an estimation of the fuel energy that is still in the combustion chamber and can still participate in combustion. Therefore, the deviation of this line from one represents the fuel energy forced into the porosity volume. The "Gross Heat Release" is the combination of the apparent heat release in the recorded pressure data and the convective heat losses required to achieve energy closure for the closed portion of the cycle.

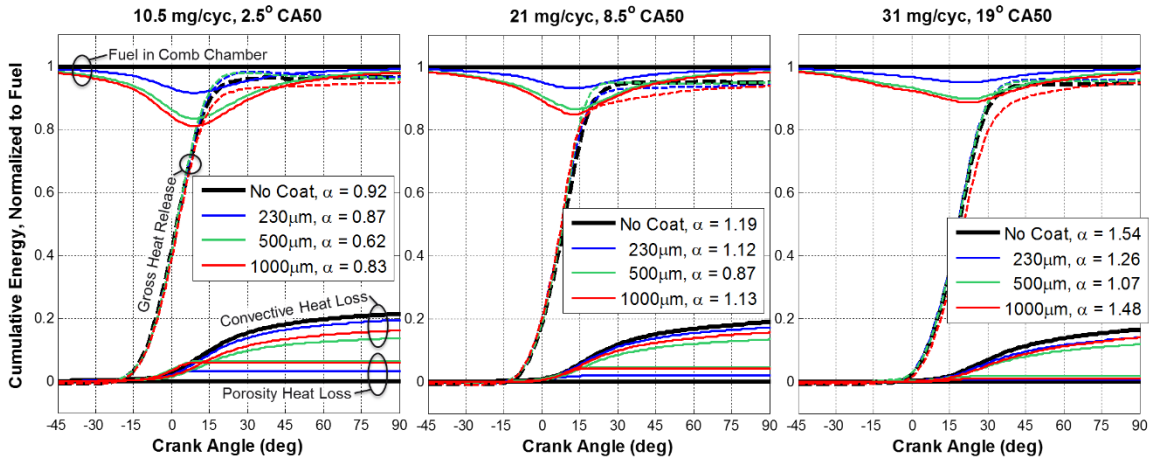

Figure 6-4: Cumulative Energy Distribution of BNT-Coated Pistons at Three Loads, 2000 RPM

At the low and mid-load points, the energy closure multiplier was very similar for the un-coated, 230 and 1000μm thickness coatings. The 500μm coating consistently showed a 20-30% lower energy closure multiplier and cumulative convective heat loss than the other coating thicknesses without showing a significant difference in the measurements of the heat flux probe or thermal energy rejected to the head or cylinder liner coolant. Additionally, this coating consistently showed a stronger late burn, with earlier CA90 timings than would be expected from the permeable porosity volume. Recorded points with the 500μm coating were the only ones in which the cumulative gross heat release greatly exceeded the estimated fuel energy present in the combustion chamber, assuming that the fuel energy was homogeneously distributed amongst the total in-cylinder mass. This was true for both 500μm pistons tested, which suggests that the data shown for the selected piston is not an outlier.

It is speculated that the 500µm coating may have been less permeable than the others to liquid fuel, which could have kept more fuel from entering the coating and enriched the mixture in the combustion chamber, promoting stronger late burns and lowering losses due to combustion phasing. The higher load points used split injections to minimize piston wetting, guided by the smoke number recorded in the exhaust, but some amount of fuel-piston interaction was still occurring based on the patterns observed on the piston crown after running. This relative impermeability could also explain the negligible difference in clearance volume measured between the 500µm coated and the uncoated piston in the measured fluid displacement test results presented in Figure 6-3. Furthermore, this would imply that the calculated porosity losses for the 500µm coating using the assumptions about porosity volume derived from motoring listed above could be higher than reality, to which the energy balance responds by reducing the convection energy closure multiplier predicted.

Conversely, the 1000µm coating consistently had the slowest late burn rate despite having very similar early and bulk combustion to the other cases, which could be due to more fuel mass getting trapped in the greater porosity volume in addition to substantial porosity heat losses. This coating had cumulative convective heat losses less than the 230µm and un-coated pistons, but had the combined heat and porosity losses on par with the 500µm coating despite having considerably hotter predicted surface temperatures. As discussed above, the 500µm coating may have underestimated convection losses due to overestimation of its porosity losses, which result in the 1000µm coating appearing out of order. Ultimately, the addition of insulating coatings for any of these pistons did not result in a decrease in total heat losses to the piston from convection and porosity.

The predicted piston surface and porosity wall temperatures are shown for all cases in Figure 6-5 as solid and dashed lines, respectively. The surface temperature for the piston is spatially-averaged across the coated center and the aluminum outside ring exposed to the gas, while the porosity temperature is thickness-averaged throughout the depth of the coating. The porosity temperature is significantly damped because of this averaging and the effects of phase lag and decay of the temperature swing as depth into the coating surface increases. The porosity temperature is higher than the average surface temperature for the thickest coating since the surface temperature is area-weighted between the coated center portion and the uncoated aluminum outer ring, which pulls down the surface average the most for the thickest coating. Comparatively, the porosity temperature only includes the coating and is thus hotter for the thickest coating. The total heat energy transferred to the piston through convection and through porosity losses are listed for each data point in the legend.

From 10.5 to 21mg fuel/cycle, the temperatures increase for all coating thicknesses, but from 21 to 31mg all of the coating temperature stagnate or decline, especially 1000µm which falls by 50°C. Although convection to the piston increases, the porosity losses for the 1000µm coating fall by 2/3rds between these two conditions, resulting in a net reduction in heat transfer of 13%. Other coatings also see a large decrease in porosity losses at the highest load, but convective losses increase at a greater rate.

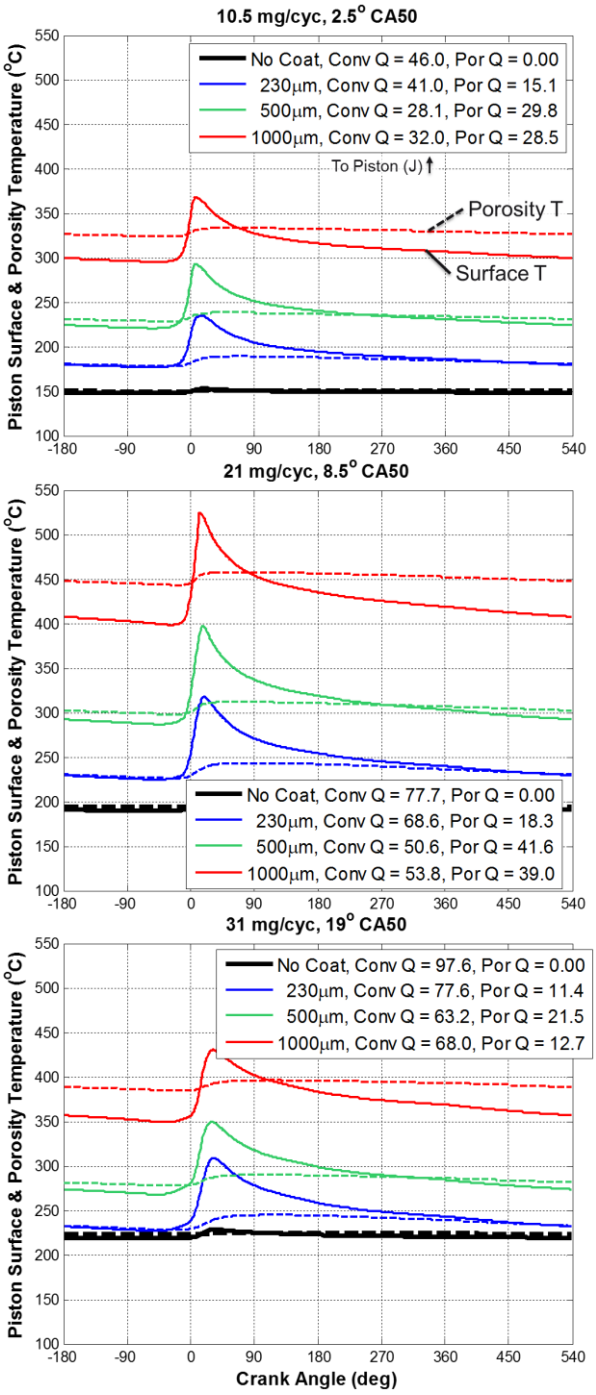

Figure 6-5: Predicted Piston Surface and Porosity Temperatures

Similarly, the temperature swing is greatest at the 21mg fueling point, primarily due to the largest porosity losses at this load. The porosity losses are much more abrupt than convection losses, as shown in Figure 6-6. These losses are calculated when gas enters the porous volume and changes temperature to match the porosity temperature, and when the porosity gas temperature changes to follow the wall temperature as a function of piston coating heating and cooling. Energy is not transferred as gas leaves the porous volume. Therefore, the biggest contribution to porosity heat losses is when hot gas is driven into the relatively cooler, more dense porous volume through compression and combustion, which takes the shape of an impulse leading up to and through the bulk of combustion near TDC. The resulting porosity losses introduce a sharp increase in the surface temperature of the coating. At lower loads, there is less heat loss overall to drive a temperature swing, and at higher loads the reduction in porosity losses coupled with the combustion phasing retard necessary to avoid knock serve to dull the temperature swing peakiness.

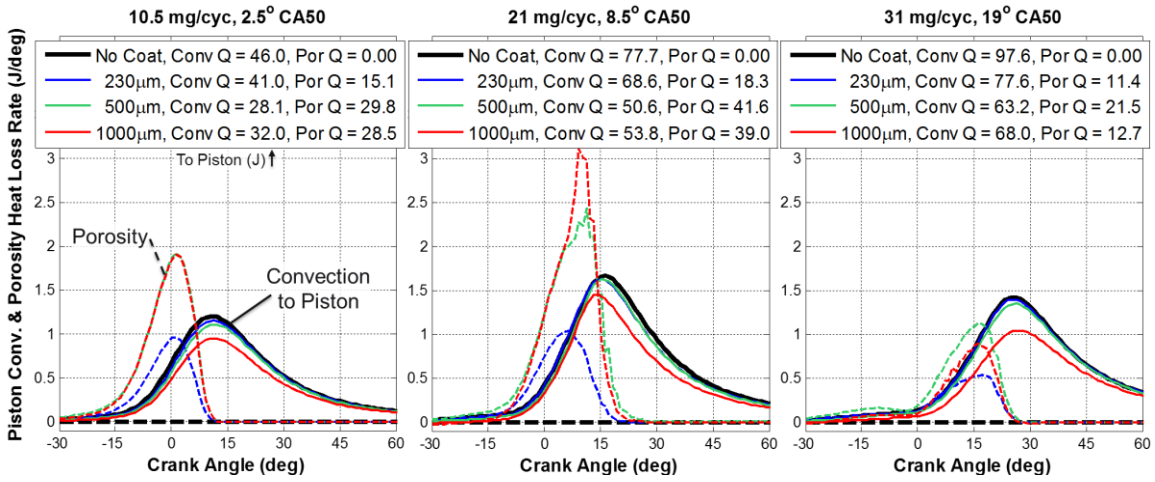

Figure 6-6: Piston Convective and Porosity Heat Losses

At low and mid-loads, the peak porosity losses rival convection for the two thickest coatings as shown in Figure 6-6. The 500 and 1000µm coating thicknesses experience similar peak and total porosity losses at low and mid-loads despite the 1000µm coating having 50% more porosity volume because it is also at a hotter temperature. Hotter coating temperatures limit porosity heat losses by reducing the difference in temperature between the coating and the gas, as well as decreasing the density and therefore mass of gas that can be held within the porosity volume at a given temperature. The porosity losses end up approximately equal for these two coatings because the 1000µm coating has less porosity volume given the total coating volume, which allows the temperature effects to outpace the additional volume effects. When the porosity volume is roughly constant as a percentage of total coating volume, as is the case for the 230 and 500µm coatings, then the increase in the total porosity volume with coating thickness has a greater effect than the increase in temperature.

The step between the 21mg and 31 mg fuel/cycle points show the largest reduction in the porosity heat losses. The porosity losses drop because of more retarded combustion at high load to avoid knock. Later combustion timing results in lower, retarded pressure rise rates and lower peak gas temperatures because combustion is competing with the rate of volume increase at later timings. These effects drive less, cooler mass into the porosity volume, which reduce the porosity heat losses. Combustion with the 1000µm coating was retarded a further 2° beyond the other 31mg points due to a lack of acceptable data at this load due to coating degradation, accentuating this trend and ultimately reducing the total heat rejection to the piston when compared to the 21mg point.

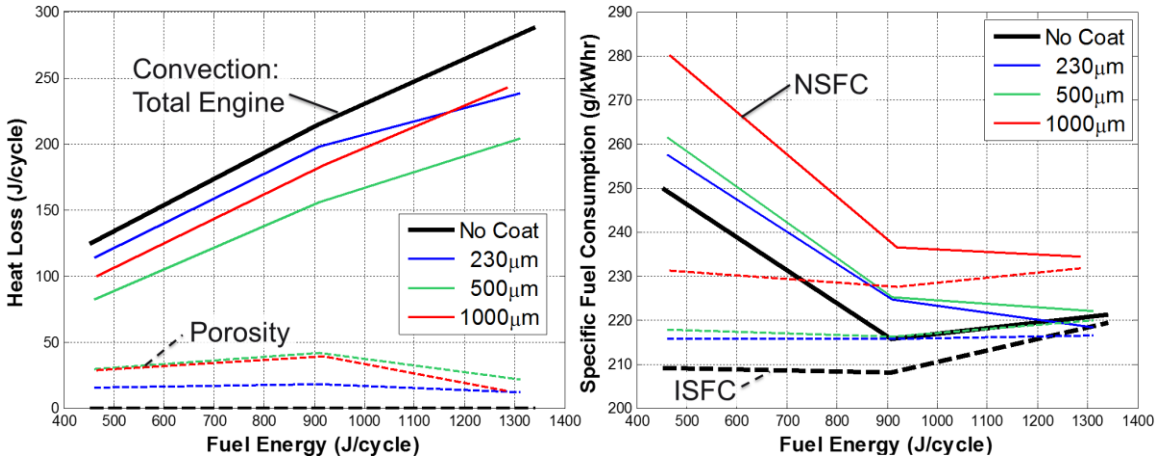

Figure 6-7: Coating Effects on Engine Performance

None of the coated pistons showed any efficiency improvement over the uncoated piston. The specific fuel consumption continually decreased with coating thickness, although the 500µm coating performance was better than could be expected solely based on thickness. At high loads, efficiency between the un-coated piston and the 230 and 500µm coatings converged due to the reduction in porosity losses with retarded combustion. The 1000µm coating continually performed worse than the others due to porosity volume as well as slow late combustion. These observed losses from permeable porosity reflect similar observations made in the literature with respect to coatings (Assanis, Wiese, Schwarz, & Bryzik, 1991) (Hoffman, 2012) (Wakisaka, et al., 2016) and combustion deposits (Anderson & Prakash, 1985). Additionally, the thickest coating hurt volumetric efficiency by 2.6%, the 500µm coating decreased it by 1.2%, and the thinnest coating had no impact. Ultimately, permeable porosity introduced additional heat losses that could not be overcome by decreased convection, and must be avoided if gains in efficiency are to be achieved.

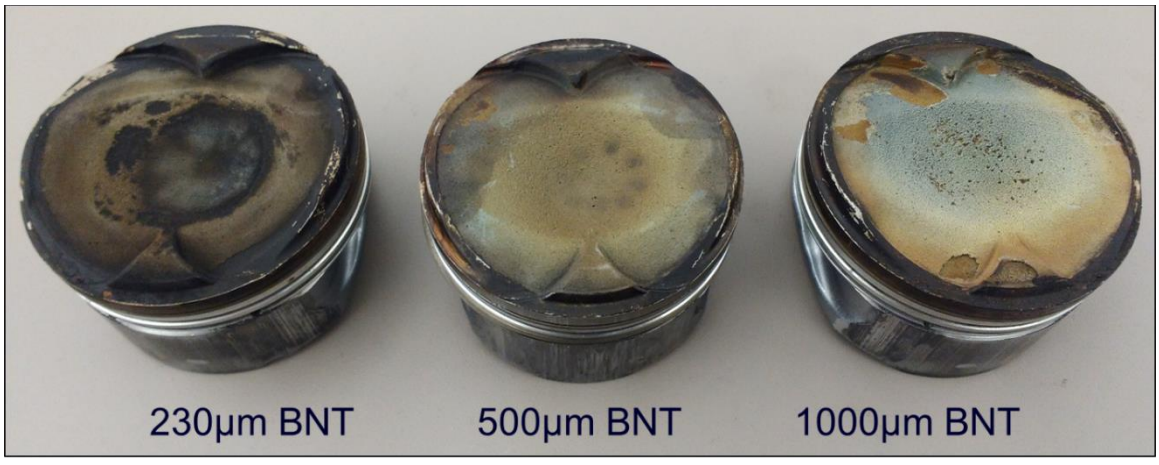

Figure 6-8: Piston BNT Coating Appearance Post-Testing

The piston coatings were all inspected after completing the engine tests, and are shown in Figure 6-8. Inspection of the 500μm piston surface after running showed considerably less discoloration around the fuel spray impingement region than the 230μm piston, but did not reveal the very big pores or large-scale flaking of the 1000μm coating. This suggests that the 500μm coating represented a robust thickness that presented a more impermeable surface to liquid fuel. The surface roughness of the 500μm piston was comparable to that of the 230μm piston in visual inspection, which implies that the greater impermeability was primarily due to thermal effects. The top surface of the 500μm coating was approximately 50°C hotter than the 230μm coating, which would promote liquid fuel evaporation upon impingement. This could prevent the fuel from wicking into the coating and packing the porosity with partially reacted hydrocarbons and soot, which appears to have occurred for the 230μm coating. Additionally, the surface temperature of the 500μm and 1000μm coatings exceeded 320°C throughout the cycle for most of the points, which was the temperature at which large deposits failed to form on the combustion chamber walls as noted by (Nakic, Assanis, & White, 1994). This evidence lends credence to the hypothesis that the 500μm coating had better-than-expected performance due to a lack of fuel penetration, deposit formation, and overall degradation of coating integrity.

The 1000μm coating was the most susceptible to physical degradation because it was the thickest. The thermal gradient from top to bottom would be the greatest for this coating, and therefore the thermal stresses due to expansion and contraction would be the greatest. Additionally, the hottest piston surface will experience the greatest heat transfer to colder temperatures such as the fuel spray and the intake air flow, which will increase the shock experienced by the coating from these sources. All of the coatings showed more flaking on the intake side than on the exhaust side, but this was most pronounced with the thickest coating. It is difficult to draw firm conclusions from this dataset due to the porosity and continued degradation of some of the coatings which could have changed their properties and response to the engine environment over the course of testing.

One form of physical degradation throughout testing that was observed with the 1000μm coating is shown in Figure 6-9. This is not the onset of a traditional auto-ignition mode of knock; instead this is a transition from controlled spark-ignition to unintentional pre-ignition. The source of pre-ignition is suspected to be loose particles that broke free from the coating, got heated by combustion in previous cycles, did not leave the cylinder with the exhaust gas, and then ignited the air-fuel mixture in the next cycle. This is supported by the large pock-marks visible in the 1000μm coating surface but not in the other thicknesses and by substantial scoring of the bore wall accompanied by larger gritty particles found in the ring-pack after running this piston. The particles were likely big enough that they were not ejected

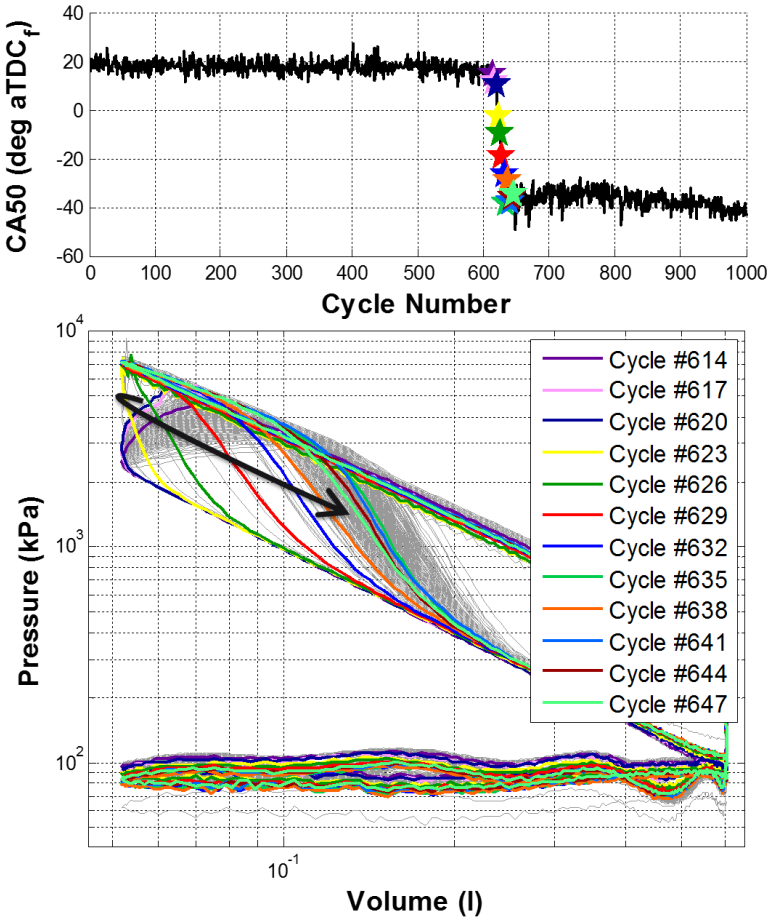

Figure 6-9: 1000µm Coating Physical Degradation at 31 mg Fueling

from the combustion chamber immediately, and resulted in hotter temperatures which could encourage more coating erosion to provide a steady source of unintentional ignition sources necessary to sustain pre-ignition at a relatively constant CA50 of 38° bTDCf. The only occurrence of the ringing pressure signature of knocking auto-ignition occurred in the 25 cycles immediately before the burn began rapidly advancing, suggesting that the increased heat transfer to the piston surface and percussive pressure waves from knock broke the first particles free from the coating where they could heat to higher temperatures in the burned gas. This pre-ignition was noted with both 1000µm coated pistons, but was only captured in recorded data for the piston presented above.

Besides the pre-ignition noted above, there were no observed trends in autoignition with the coatings. The difference in gas temperature between the un-coated case and each of the coating thicknesses is shown in Figure 6-10 for the 31mg fueling point. During the majority of the intake and compression strokes, the bulk gas temperature of all of the coatings were within 20°C of the uncoated case, providing a very small difference in activation energy for autoignition. The spikes in temperature just after TDC are due to slight differences in combustion phasing between each coating and the uncoated case for the experimental data. Effectively, the reduced compression ratio due to coating porosity was preventing an increase in bulk gas temperature despite the hotter wall surface temperature. This was borne out in measured knock amplitude over a combustion timing sweep, where increasing coating thickness actually showed a reduction in knock at a given bulk combustion phasing.

Lower knock amplitudes with increasing insulation is counterintuitive, but could potentially be explained when considering the reduction in thermal stratification with hotter walls but lower compression ratio. Hotter walls will increase the local gas temperature close to the walls, but lower compression ratio will reduce the overall temperature. If the walls are hot enough to drive up the bulk gas temperature during intake and compression despite a reduction in compression ratio, then what would traditionally be the coldest packets of gas near the wall will be hotter while the more central packets of gas further away from the wall would necessarily be cooler than the un-coated case to maintain a similar average gas temperature. Autoignition would be most likely to occur in the unburned packets that are near the periphery of the chamber but not directly adjacent to the walls. These gas packets will still be hotter than the gas near the wall, especially after the combustion has been initiated and further compresses the unburned gas, and will be the most likely to cross the autoignition threshold. Therefore, it can be reasoned that the combination of a reduction in compression ratio and increase in wall temperature from these specific coatings could potentially flatten the thermal stratification and the likelihood of autoignition within the most prone regions.

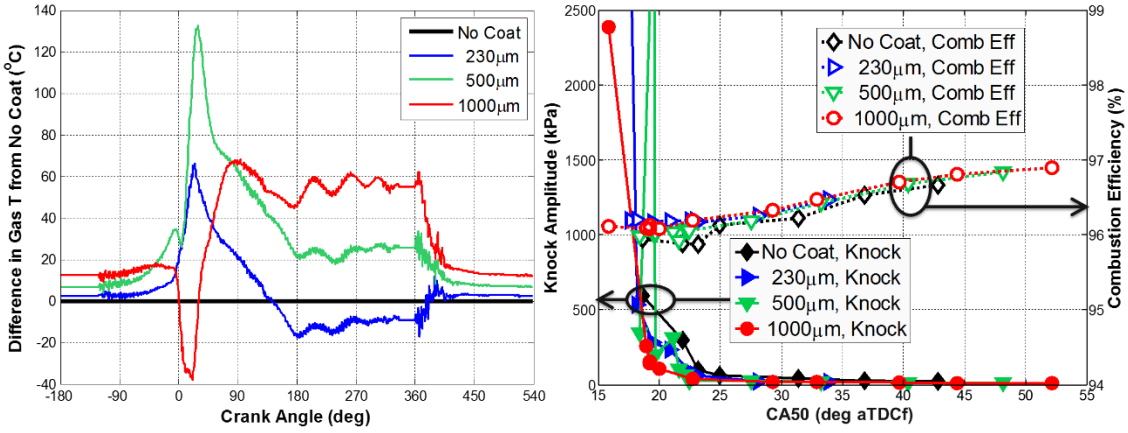

Figure 6-10: Difference in Gas Temperature, Knock Amplitude, and Combustion Efficiency at 31mg Fueling

Combustion efficiency tended to be slightly higher for coatings than for the un-coated baseline as well. The differences were very small, but could have been driven by the generally hotter late expansion and exhaust temperatures that accompanied a longer later burn and thermal insulation.

6.3.2 Simulated Performance

The effects of the coating porosity on heat losses, fuel mixing, and compression ratio all acted to confound the experimental results. To understand the individual contributions of each of these effects, the calibrated thermodynamic model was used in conjunction with the thermal model to simulate the engine with each of the coated

pistons in multiple steps. Each comparison line in Figure 6-11 is the difference between the coated-piston data or modeled results and the uncoated aluminum data or modeled results.

The first step, shown by the lines labelled “All Effects”, is a comparison of the instantaneous convective and porosity heat losses, and of the instantaneous indicated power, derived from the experimental data. The thermodynamic model did not allow for a porosity volume and the subsequent heat loss assumptions in the data processing routines to be applied, so the first step had to use experimental data.

The second step is represented by the second set of curves, dubbed “No Porosity Hx”, which utilized the calibrated thermodynamic and thermal models. Porosity heat losses from the experimental data were excluded from the modeling results, as described in the previous paragraph. The experimental compression ratio, combustion profile, boundary conditions, and piston thermal geometry were maintained for the various coating thicknesses. However, the energy closure multiplier from the un-coated case at the same load and combustion phasing was applied to the coated model. The rationale for this was that the energy closure multiplier should be the same for all cases at the same load and combustion phasing as long as the wall temperature for convection and other energy loss mechanisms were being properly captured, since the convection coefficient would respond only to the combustion chamber gas properties. This was experimentally observed when comparing most of the different hardware sets at matched fueling and combustion phasing when the porosity losses were accounted for. Additionally, a comparison of the instantaneous heat flux measured at the cylinder head showed that there were minimal differences in heat transfer at this location, indicating that the in-cylinder thermal environment, turbulence, and boundary layer were similar, at least in the measured location. While this certainly does not mean that the conditions for convective heat transfer were identical everywhere in the chamber, especially at the piston top surface, it does suggest that there is some basis for making this assumption. Following this assumption, the largest impact on the energy closure multiplier from experimental data would be whether the heat loss from permeable porosity was accurately captured. Referring back to Figure 6-4, this multiplier (α) was consistent between the un-coated baseline and the 230μm and 1000μm coatings, with the 500μm coating consistently requiring a slightly lower multiplier that suggested it was less permeable than the others. This methodology would remove the heat losses from porosity, but retains the effects of fuel absorption and mixing due to the porosity evidenced in the heat release profile, and the reduction in compression ratio. The modeled results for this and all subsequent steps for the uncoated engine remained the same, since the uncoated piston did not have any of the porosity loss mechanisms.

The third step involved the removal of the fuel absorption and mixing effects on performance, shown in the third set of curves ("No Comb Effects"). This step consisted of the application of the combustion profile and boundary conditions from the non-coated hardware set to the coated thermodynamic model, while retaining the lower compression ratio from the coated data. This assumes that the primary way that the effects of fuel absorption into the porous coating are seen is through the shape and cumulative magnitude of heat release in the experimental data. The energy closure multiplier from the un-coated baseline is also applied for the same reasons as the previous paragraph.

The fourth step accounted for the reduced compression ratio due to the permeable porosity volume. This was accomplished by using the compression ratio from the un-coated baseline in the fourth curves. In essence, the thermodynamic model for the fourth set of curves ("No CR Reduction") for coated cases and the baseline are identical. Only the thermal model of the piston was different, which reflected the presence and thickness of each coating.

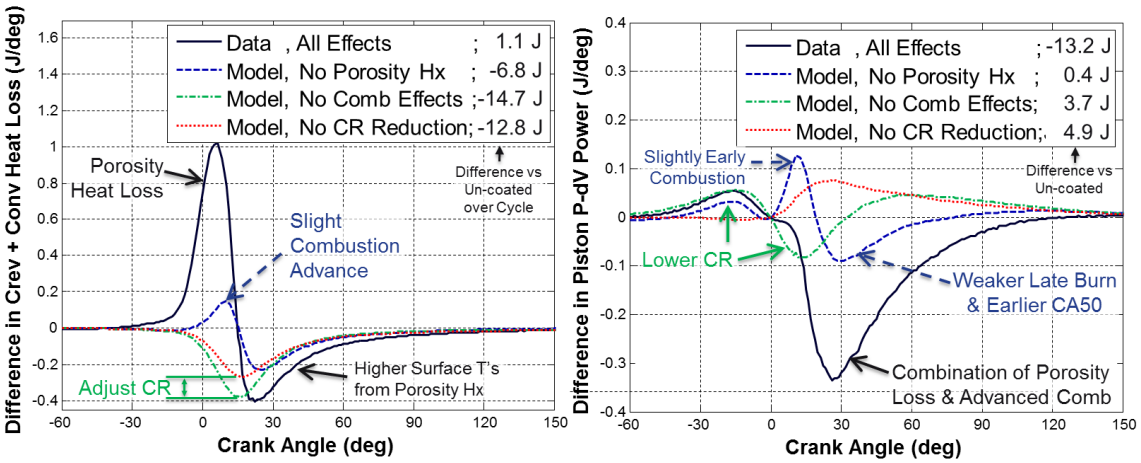

Figure 6-11: Individual Effects of 230µm Coating on Heat Loss and Indicated Power at 21 mg/cycle Fueling

The individual effects from each of these steps are shown in Figure 6-11, with the difference in heat transfer (including porosity losses) between the 230µm coating and the un-coated baseline at 21mg fueling rate on the left, and the difference in indicated piston power on the right. This coating thickness and load were chosen for clarity, but other thicknesses and loads showed similar effects. The difference in heat loss in the trace for the experimental data is dramatic, with a large spike around TDC due to the increasing pressure and temperature driving hot gas into the porous volume. After approximately 15° $aTDC_f$, the curve becomes negative which signifies that the heat loss rate in the data is lower than for the uncoated baseline because the piston surface is hotter and the gas is cooler due to the porosity heat loss. Comparing the total heat loss of the first step "Data, All Effects" trace to the second step "Model, No Porosity Hx" line shows the net effect of the permeable porosity to be worth 7.9 J

over the entire cycle. However, a cumulative 14.6 J in heat energy was lost due to porosity around TDC between -30° and 15° aTDC. This phasing has the greatest impact on piston indicated power because energy has already been expended to compress the gas, but additional heat losses near TDC will lower the gas pressure through the entire expansion stroke, hurting the positive energy generation by expansion. The total difference in piston indicated work due to the porosity heat losses alone amounts to a loss of 13.6 J each cycle.

Removing the combustion effects by moving from the second "Model, No Porosity Hx" curve to the third "Model, No Comb Effects" line had the same net effect on total heat losses of 7.9 J/cycle, but the impact on indicated work was only 3.3 J/cycle. The primary combustion effect was a slight CA50 retard of 0.9° when removing combustion effects, which can be seen as an early positive peak in heat loss and indicated work after TDC of the "Model, No Porosity Hx" trace in comparison to the "No Comb Effects" line. The more advanced combustion causes pressure and temperature to increase earlier in the cycle when the volume is smaller, resulting in higher gas temperatures and pressures for the early part of the cycle. In this instance, since the additional heat loss early in the expansion stroke was accompanied by an increase in cylinder pressure at this time, the effects on indicated work were minimized. A peak in heat transfer early is usually accompanied by less heat transfer later in expansion since the gas will be cooler, but the differences in the indicated work traces beyond 20° are primarily due to the heat release shape for the final 4% of fuel energy. Despite having a more retarded CA50, combustion for the un-coated engine was considerably faster towards the end, having reached its final value by 40° aTDC. The tail of combustion with the permeable coating was dragged out until the exhaust valve opened, which prevented the piston from extracting as much work from the last 30 J of fuel energy. Physically, this likely represents fuel energy trapped within the permeable porosity of the coating that was only released back into the combustion chamber when the in-cylinder pressure was falling, delaying the release of the trapped fuel's chemical energy.

The last step was to remove the effect of the compression ratio difference observed in the coated engine data, moving from the third "Model, No Comb Effects" line to the fourth "Model, No CR Reduction" trace. Increasing the compression ratio from 11.7 to 12.0 for this coating thickness while holding everything else constant results in a smaller reduction in heat loss from the coating since the gas temperature near TDC was higher. Additionally, more work was required for compression, shown as a reduction in the positive indicated work difference prior to TDC. All of this additional compression work and more was recovered during expansion with the thermal barrier coatings at the higher compression ratio, providing the most relative and absolute benefit in indicated work.

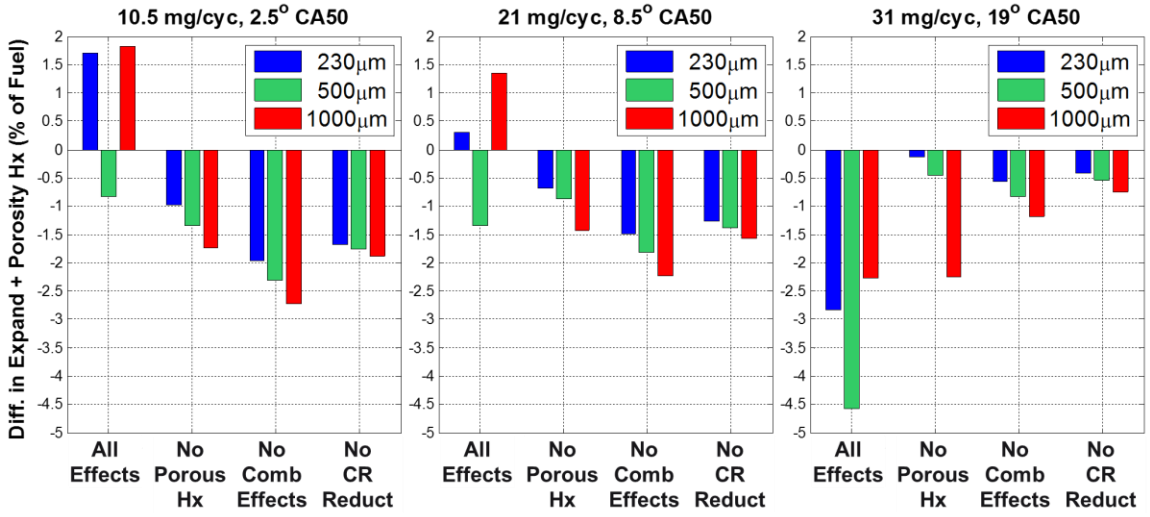

Figure 6-12: Difference in Expansion plus Porosity Heat Transfer from Un-coated Baseline

The total heat losses from porosity and convection during the expansion stroke are plotted for all cases and loads in Figure 6-12. It is clear that the 500μm coating was experiencing lower total heat losses in the experimental data ("All Effects") than the other coatings, as suggested previously by the difference in the energy closure multiplier for this coating. Otherwise, the effects of porosity heat losses were the largest deviation from the expected reduction in heat losses, especially when CA50 was near TDC. At the 31 mg fueling point when porosity heat losses were minimal, all three coatings did exhibit 10 to 20% lower heat losses than the baseline, although the baseline likely had higher convection losses than the coated cases at this load due to the higher knock amplitude. Removing the combustion profile effects consistently decreased heat losses by 5 to 8 J, while increasing the compression ratio to the baseline level increased the heat losses by roughly 3 J. All of the modeled results showed the expected trend of decreasing heat losses with coating thickness. Once the coating thickness was the only difference between the modeled results, all three coating thicknesses decreased heat losses by similar amounts. This was because the thinnest coating was already 77% of the $depth_{1\%}$, allowing it to have the same amount of temperature swing as the thicker coatings. Similarly, the coatings had the greatest effect at the 21 mg fueling point, since the combination of sufficient fuel energy and earlier combustion timing enabled the most temperature swing coupled with the hottest gasses.

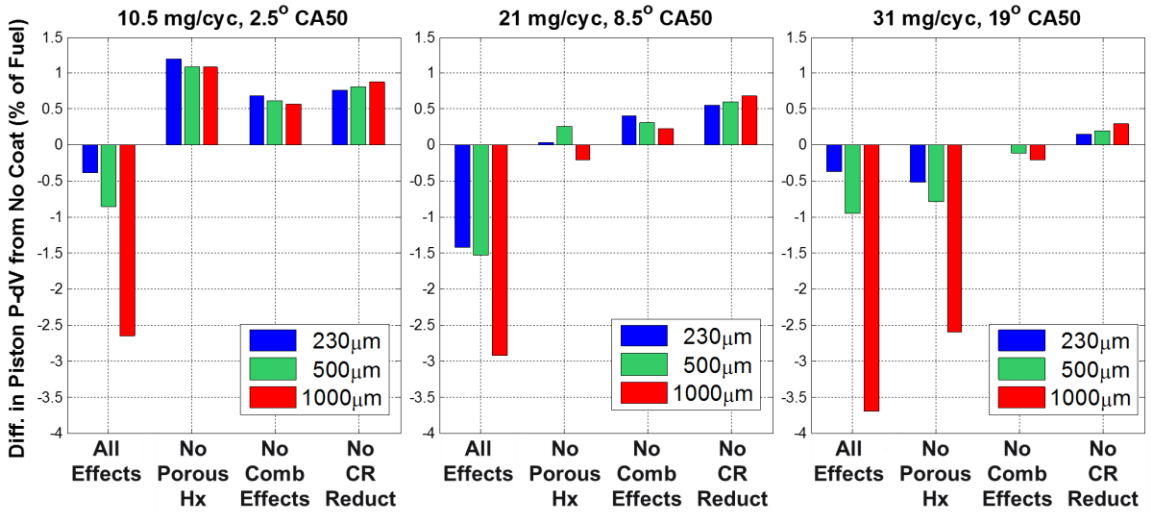

Figure 6-13: Difference in Indicated Piston Work from Un-coated Baseline

The impact of the change in heat losses for each of these configurations on piston indicated work is shown in Figure 6-13. Porosity heat losses had the largest impact on indicated work at the lowest two loads, while their magnitude was diminished and the combustion profile impacts dominated at the highest load. Additionally, the reduction in compression ratio due to porosity in thicker coatings more than offset the benefits of higher surface temperature. Furthermore, the presence of fully developed temperature swing enabled all three coatings to have a similar level of indicated improvement at low and mid loads. The importance of reducing heat losses at the highest load was reduced because of the retarded combustion phasing, leaving less change in volume after the heat loss reduction for extracting energy from the gas. A larger portion of the improvement in indicated work therefore is derived from the reduction in throttling losses with hotter surface temperature during the intake stroke, which favors coating thickness.

6.4. Summary and Conclusions

The interplay of many processes related to the presence of coatings besides their thermal properties tends to muddy the results of experimentation. Effects from permeable porosity heat losses, fuel absorption, and a reduction in compression ratio all confounded the analysis, requiring careful consideration to draw conclusions.

- Porous heat losses remove energy and fuel mass from the combustion chamber near TDC and throughout the combustion process when they can be the most beneficial, having a severely negative impact on indicated work.

- Utilization of the thermal engine structure model coupled with assumptions on the permeable porosity heat losses allowed for analysis of experimental data using observed engine properties without unreasonable results.
- Earlier combustion phasings near or prior to TDC suffer the worst porous heat losses due to the large mass flows of hot gas generated by compression and combustion pressure; late combustion phasing avoids these losses but is generally sub-optimal for efficiency
- Lengthened heat release tails were observed with the coatings, indicating fuel was trapped within or on the surface of the coating and effectively prevented from combusting until much later in the cycle.
- Porosity heat losses impacted indicated work most severely, followed by combustion profile effects, then by reduced compression ratio from permeable porosity
- Successful implementation of temperature-swing enabling insulation requires negligible permeable porosity, necessitating a way of sealing the porosity from combustion gasses.

7. Novel Materials: Development and Testing

7.1. Introduction

Learnings from the prior analytical and experimental investigations were applied to develop a novel thermal barrier material that could exceed the temperature-swing performance of conventional insulating materials. Requirements for the material were defined, and a variety of solutions were investigated, with the most promising presented herein. Samples of this material were created for thermal properties testing, and for experimental evaluation within the single-cylinder test engine.

7.2. Material Requirements

There are many requirements for any potential material that will be used in-cylinder. The material must be strong enough to survive peak combustion pressures while at elevated temperatures, since the pressure and temperature peaks at the surface occur in close proximity. Chemical and oxidation resistance are essential due to the combination of high temperatures, pressures, and presence of oxygen and caustic products of combustion. High ductility and a relatively low coefficient of thermal expansion are necessary to mitigate and relieve thermal stresses from frequent temperature cycling. Lastly, chemical compatibility or a durable bonding process must exist between the material and conventional metals used in engine construction.

Previous analysis had identified the need for very high levels of porosity to leverage the low heat capacity and thermal conductivity of air for achieving surface temperature swing. The lowest conductivity achievable with solid materials suitable for use inside an engine is approximately 1 W/m-°K for certain ceramics. Lower conductivities are possible only through the use of structural elements such as engineered and naturally occurring air gaps, or anisotropic planes. Similarly, most bulk materials have volumetric heat capacities of over 1500 kJ/m^3-°K, purely due to the range of densities that solids possess.

The addition of porosity will lower both the conductivity and the volumetric heat capacity. Void volumes will effectively replace some fraction of the cross-sectional area available for conduction within the material with less-conductive air. Assuming that the voids are evenly distributed, conductivity should fall approximately linearly

with the increasing volumetric void fraction, although specifically engineered structures can alter this path significantly. Assuming certain geometric traits allows for a rough estimation of the thermal conductivity, based on the average cross sectional area and conduction path length. Volumetric heat capacity is more straightforward, combining the density calculated with the volumetric porosity ratio, and the heat capacity utilizing the porosity mass-ratio. For solid materials with gas-filled porosity volumes, the mass-ratio is almost consistently 0 due to the three-to-four order of magnitude difference in density between solids and air; therefore the mass heat capacity of the porous material can reasonably be assumed to be the same as the solid. This porosity must be sealed from the combustion gas to avoid all of the loss mechanisms determined in Section 6.3, necessitating a closed-cell structure or specific sealing layer.

7.3. Material Structure and Application

All of the criteria were taken into consideration when evaluating possible materials. High-temperature strength and oxidation resistance dictate a metal or alloy that includes nickel or chromium, such as a stainless steel or Inconel, or a stable, inert ceramic like yttria-stabilized zirconia. In general, metal alloys tend to be more ductile than ceramics, but ceramics have lower thermal expansion coefficients, both of which alleviate the thermal stresses that will arise from temperature-swing behavior.

A hollow microsphere structure with void space within and between the microspheres was chosen as a promising path to achieve very high porosity while maintaining strength and manufacturability. Porosity is achieved through the hollow void area within the microsphere, and in the interstitial volume between microspheres. A simple cubic structure, as assumed for properties analysis below, has a packing ratio of 0.52, meaning that 48% of the volume is interstitial voids between spheres while 52% of the volume is within the spheres. Higher packing ratios can be achieved through different arrangements of the spheres, and by including a distribution of sphere sizes.

There are multiple companies that make hollow glass, ceramic, and metal-coated spheres with a wide variety of diameters and thicknesses that can be sintered directly together to create insulating layers, although precise control of variables necessary for a thermal barrier are not present in commercially available samples. Therefore, the basic stock of appropriately created microspheres needed to be created through experimentation and careful control of the process. Sintering the microspheres without a separate binder preserves the high porosity by not filling the interstitial voids with material. However, this type of structure requires a sealing layer to cap the insulating layer and prevent gas intrusion into the interstitial volume, and to prevent this volume from filling with hydrocarbons and deposits that would reduce the

coating effectiveness. Bonding layers designed to bridge the difference in thermal expansion coefficient between the insulating layer and underlying component, and absorb the thermal stresses that would result at the joining surface were considered for both ceramic and metallic microspheres.

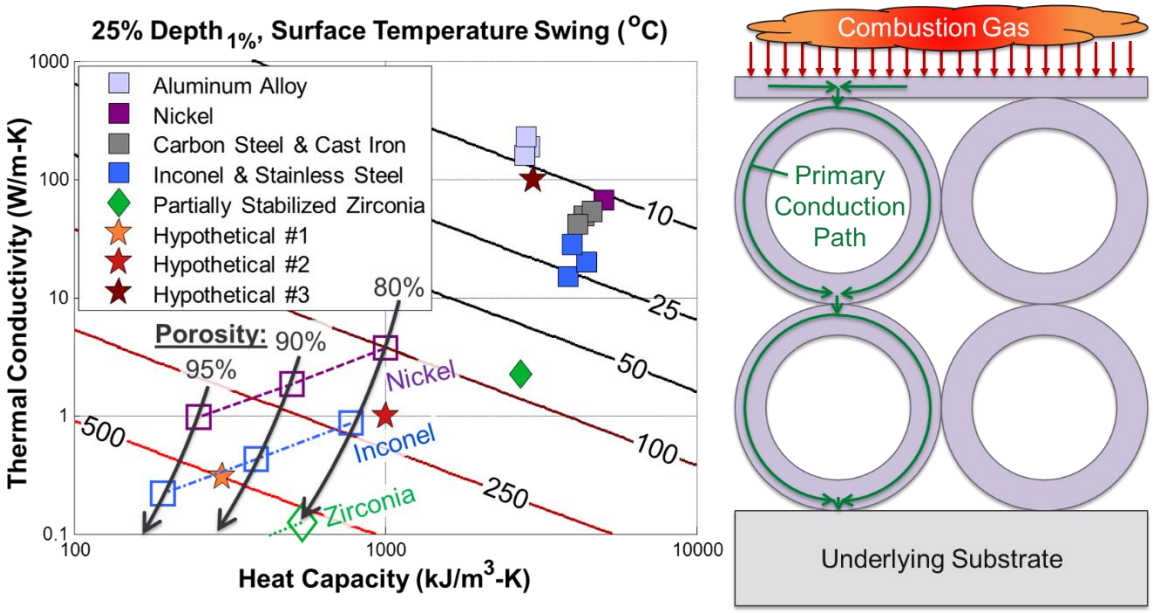

Figure 7-1: Predicted Properties and Assumptions for Highly Porous Materials

Estimations of the material properties for porous structures, and a pictorial representation of the underlying assumptions, are presented in Figure 7-1. The temperature swing lines from the "Fixed Thermodynamic Conditions" analysis for a coating of 25% depth$_{1\%}$ thick were plotted for reference, as well as some of the material properties discussed there. The path length used in calculating the conductivity is shown to the right, which assumes that the path follows the "area-averaged" radius through the hollow spheres of the solid material, with all spheres arranged in a simple cubic structure. The wall thickness of the spheres was calculated from the total volumetric porosity. Additionally, the mean horizontal distance that energy would need to travel when deposited evenly along the top sealing layer was considered for a unit section (a square of the same diameter as the sphere for simple cubic packing). The sealing layer was assumed to be of the same material as the microsphere shell. Both pure nickel and Inconel can theoretically reach a combination of properties that would give equal or better temperature swing than the hypothetical materials #1 and #2, but over 90% porosity is required. Stabilized zirconia does not require as much porosity due to the lower intrinsic heat capacity and thermal conductivity that form the starting point.

The addition of a sealing layer to cap the surface will impact the wall temperature swing, since the sealing layer will concentrate mass at the point where it is least

desirable for temperature swing. To evaluate the effects, the simple "Fixed Thermodynamic Conditions" 1D thermal model was employed. The sealing layer was modeled over an insulating layer of Hypothetical material #1 as a surrogate for the hollow microsphere material, over the aluminum-like material #3 substrate. The sealing layer was modelled with the properties of pure Nickel, as plotted above. Cap layer thickness and insulating layer thickness (as a percent of the depth$_{1\%}$) were varied to see the effects on temperature swing, shown in Figure 7-2.

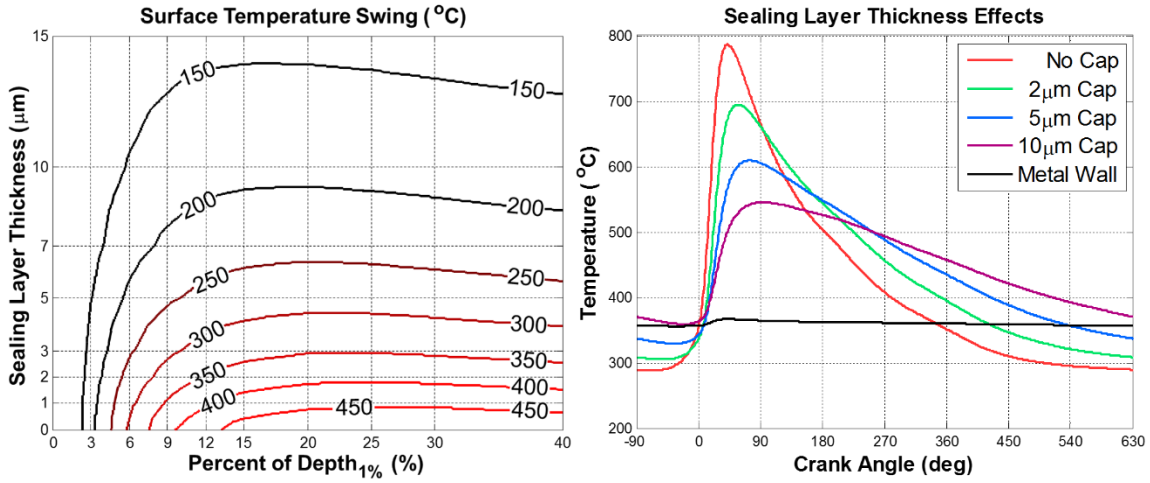

Figure 7-2: Effects of Sealing Layer over Hypothetical Material #1 on Surface Temperature Swing

Increasing the cap thickness quickly reduces the peak surface temperature swing due to the thermal inertia of the sealing layer's dense mass at the surface of the coating. The result is a considerably more gradual surface temperature profile with a delayed and muted peak, and a much slower decay to the minimum temperature. While the layer without the cap reaches the same temperature as the metal wall by the end of the exhaust stroke, a 5μm cap delays this point until the end of the intake stroke, and a 10μm cap barely reaches the metal wall temperature at its minimum, just before TDC$_f$ of the next cycle. The 10μm thick sealing layer therefore would have more harmful heat transfer from the walls to the gas during intake and compression, hurting the volumetric efficiency and compression work.

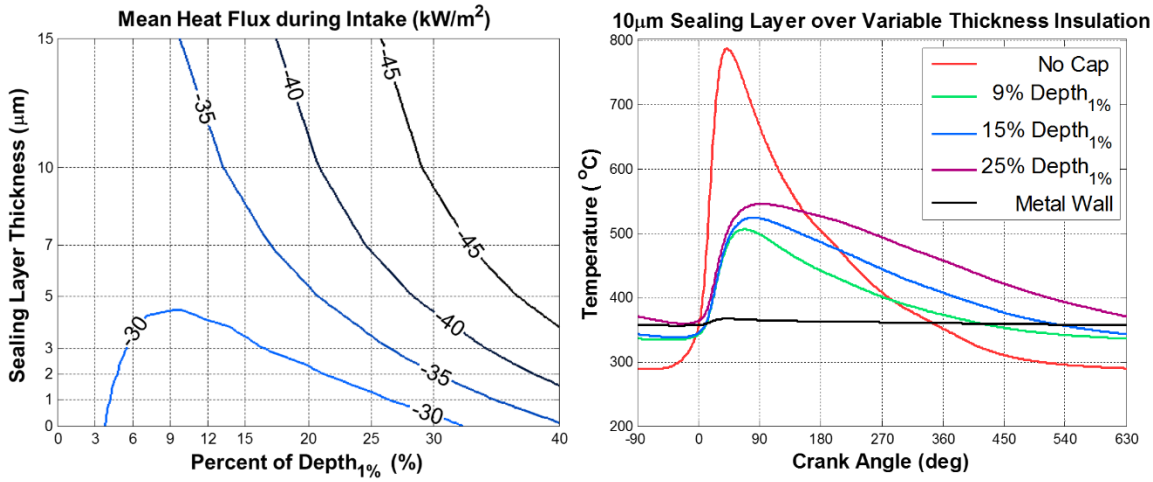

Figure 7-3: Effects of Sealing Layer on Intake Heat Transfer and Surface Temp over Variable Thickness Insulation

The muted behavior of the surface temperature profile can be mitigated by decreasing the thickness of the insulating layer beneath the sealing cap without incurring a large reduction in the total surface temperature swing. This behavior can be seen for the 10μm cap thickness to the right in Figure 7-3. Essentially, reducing the insulating layer thickness increases the heat transfer from the backside of the capping layer, allowing it to shed heat more quickly in order to minimize heat transfer during the intake stroke, as shown to the left. A balance must be struck between heat transfer during the intake stroke and ultimate temperature swing in Figure 7-2 for a given capping layer thickness. Ultimately, a 10μm cap over Hypothetical material #1 at the optimum thickness will result in a 170°C temperature swing; on par with the un-coated Hypothetical material #2. A 5μm cap will give a 280°C swing which is considerably better than predictions for a thicker cap, but still falls short of the ideal.

7.4. Measured Properties

An example of the novel insulating material was created, with the end result consisting of hollow Nickel alloy spheres sintered together to form the insulating layer. The average microsphere diameter was 40μm, with a shell thickness of only 1μm. The measured density of the final structure indicated a total porosity of 92%, in comparison to an estimated density using the nominal measured parameters and a simple cubic structure of 95.2%. The difference is likely due to the distribution of sphere sizes around the nominal 40μm and the difference in packing density from the assumptions that would accompany that distribution. A sealing layer of 5.9μm Nickel foil was sintered over the top of the microsphere layer.

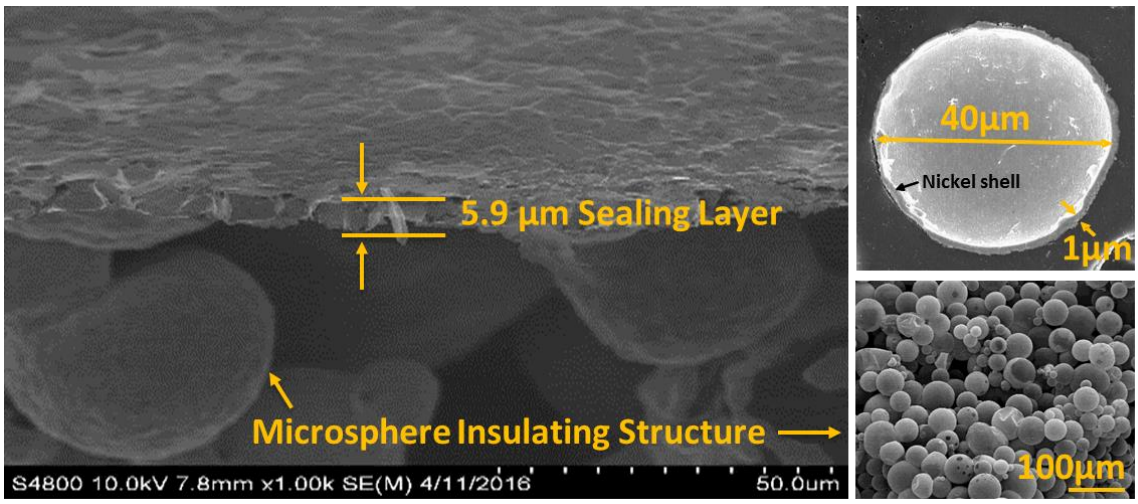

Figure 7-4: Novel Insulating Coating Structure with Sealing Layer, Nickel-Coated Microspheres, and Sintered Microsphere Insulating Structure

For components destined for testing within an experimental engine, the insulating layer thickness was approximately 200µm due to a confluence of concerns. This equates to approximately 40% of the depth$_{1\%}$ of the average microsphere material at 2000 RPM. A nominal 5µm Nickel foil was applied to the top of the insulating layer to seal the layer from combustion gas, and to provide a smooth surface to the combustion chamber to minimize heat transfer.

Wafers of the insulating layer were created following the aforementioned methodology and tested using the procedures documented in Section 3.2. The resultant thermal conductivity was approximately 0.2 W/m-K, and the calculated density was approximately 470 kg/m^3, which put the combination of thermal properties in a similar regime to Hypothetical material #1. The necessary sealing layer would reduce the achievable temperature swing by approximately 40% based on the modeling work previously described, but the estimated gain in engine performance would still be greater than with the current state-of-the-art insulation.

7.5. Experimental Results

Engine components destined for experimental testing were developed using these coatings. Intake and exhaust valves were the more simple pieces to attach the coating to, as the conventional material of the valves was compatible with the Nickel alloy and could survive the sintering temperatures necessary to affix the coating. For these coatings, the sealing layer must be relatively flat so that it can be accomplished with a sheet foil, although other processes to create the complete insulation and sealing layer are being developed. Aluminum parts such as the piston require additional

bonding layers and processes due to the difference in the melting temperature of Aluminum and the sintering temperature of the Nickel alloy.

Figure 7-5: Coated Intake Valves, Before and After In-Cylinder Firing Conditions

The results of running the intake valves are shown in Figure 7-5, with the left-most picture in each row taken immediately after installation. There were some minor scratches from lapping the valves to ensure adequate sealing. These scratches are accentuated in the image since they still have some darker lapping compound that squeezed out and got spread by the lapping cup pressed into them. First, the engine was motored for 10 minutes, at which point the coatings were examined with a bore-scope in-situ. The coating on one intake valve was still present, but the coating had detached from the other valve. No evidence of the coating was seen in the engine, and the motoring compression was still strong at the end of the test, so firing tests at two loads for 15 minutes each were conducted. The remaining coating was inspected between and after firing tests to check its integrity. After these tests, the head was removed to permit closer inspection and replacement of the failed valve, at which point the middle picture in the top row was taken, and the valve in the bottom row of

pictures was installed and photographed. The engine was then reassembled and the full set of experimental testing sweeps was repeated twice for a cumulative 70 hours of operation. The rightmost image in each row shows the condition of the valves after running the full set of testing. The Nickel foil sealing layer has continued to deteriorate throughout testing, exposing more of the underlying microsphere structure. In general, the greatest deterioration observed was in areas that did not have complete foil coverage to begin with, but small breaches and cracking were observed throughout the coating surface.

Similar results were observed with the exhaust valves, although none of the exhaust valve coatings completely separated from the valve. The total coated surface area was only 6.9% of the TDC surface area for the intake valves and 4.4% for the exhaust valves, so the difference in measured performance was expected to be minimal. The effects of the fuel spray interaction with the intake valves could potentially confound the results, since the fuel injection timing was centered on the intake stroke to coincide with maximum air flow rates. At this time, the intake valves were between 8mm and 10mm open, allowing the valve seats and back-sides to intersect the fuel spray. Because of the fuel jet and valve angles, the coated valve faces were never directly exposed to the spray, but estimated differences of up to 40°C in intake valve back temperature may have an effect on fuel vaporization and mixing. Approximately 40% of the fuel delivered could experience these effects, as estimated by the nominal spray plume and valve geometries; fuel injected towards the front, back, and exhaust-side of the engine would be unaffected.

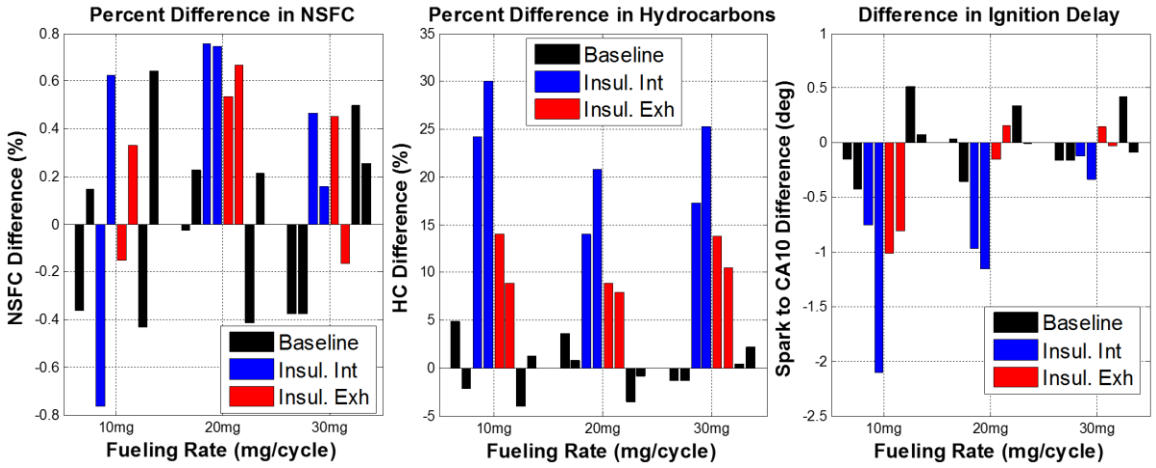

Figure 7-6: Experimental Results from Baseline, Insulated Intake, and Insulated Exhaust Hardware Sets

Experimental results from all of the hardware sets in the order in which they were taken are shown in Figure 7-6. Two sets of points with the baseline hardware were run, followed by two sets with the coated intake valves, then two sets with the coated exhaust valves, and finally a repeat of the baseline. All results are normalized by the

average of the baseline measurements taken before and after the insulated valve measurements. Individual measurements at the same CA50 were chosen for this comparison.

It is clear that both the insulated intake and exhaust valves resulted in considerably higher hydrocarbon measurements than the roughly 15 g/kg fuel of the un-coated metal valves in the baseline (presented as difference in emissions index to remove any effects of slight fuel flow variance). The ratio of the hydrocarbon increase for the intake valves versus the exhaust valves is commensurate with their difference in surface area and thus permeable volume. This was counter to the observations with the conventional insulating materials, but a considerably larger surface area on the piston was insulated with those materials. This difference would decrease overall heat losses and therefore increase the gas temperature late into the expansion stroke and throughout exhaust, which could have assisted hydrocarbon oxidation. The coated area for the novel materials on the valve faces was considerably smaller, with a much larger interstitial void volume (in comparison to the BNT used previously) within the coating that could trap more hydrocarbons yet fail to cause them to decompose at the same rate. This suggests that the sealing layer was breached and the coating did not remain impermeable to combustion gasses, and supports the visual evidence of the sealing surfaces after removing the valves from the engine.

Higher unburned hydrocarbon emissions were accompanied by an average increase in the NSFC for coated components, although the variability of this metric between different baseline cases is similar in scale to the differences observed, and all of the differences are close to the measurement uncertainty of +/- 0.5%. On average, the greater hydrocarbon emissions for the intake valves would account for approximately 0.4% and 0.15% higher NSFC for the coated intake and exhaust valves respectively at 10mg, 0.18% and 0.12% at 20mg, and 0.16% and 0.1% at 30mg. These changes in NSFC due to the drop in combustion efficiency are difficult to determine because of data variability at 10mg, but they only account for about 1/3 of the observed NSFC losses with coated parts at 20mg, and about ½ of the losses at 30mg. Previous analysis of conventional permeable coatings showed the greatest porosity heat losses at the 20mg fueling point due to a combination of greater trapped mass & fuel energy, and more advanced combustion, with relatively small losses at the lower and higher fueling points, which roughly aligns with the unaccounted-for net losses with coated intake and exhaust valves. It is difficult to make any precise determination with respect to NSFC for these parts because of the measurement uncertainty and the small areas coated, but in general it would appear that there was a slight detriment to NSFC with the coated parts.

A consistent reduction in the ignition delay between the spark and CA10 was noted for all of the insulated hardware sets. This could be the result of a variety of processes:

hotter valve faces improving the local flame speed near their surfaces, hotter valve faces more completely vaporizing any fuel that was carried near them through injection or charge motion, or a hotter intake valve seat and backside where some portion of the fuel could impinge during the injection event. The first two effects could affect the early flame development with either coated intake valves or coated exhaust valves, while the last effect is only possible with the intake valves. However, for the backside temperature of the intake valves to be hotter, the insulating material must not be working to reduce heat transfer or porosity heat losses to the coating are increasing the intake valve temperature. As load increases, the effects become less noticeable, possibly as the flame speeds increase with less intake throttling and vaporization improves with hotter wall temperatures at higher load. The faster ignition delay is observed with both the intake and exhaust valves at the lowest load, but only with the intake valves at the mid-load condition, suggesting that a combination of effects are responsible for this behavior.

Between these results and the images of the coating surfaces in Figure 7-5 post-combustion, it was concluded that the coatings had permeable porosity, and the subsequent losses were modeled in the results presented here. The sealing layer appears to have failed early in testing, as evidenced by the higher hydrocarbons, visual pock-marking, and suggested by the NSFC and ignition delay differences. The permeable volume was estimated as the void volume (1 – simple cubic packing ratio) of the insulating layer.

Valve face temperatures predicted by the thermal model for hardware sets with conventional valves, the set with just the insulated intake valves, and the set with just the insulated exhaust valves are shown for the low and high fueling rates in Figure 7-7. The insulation and sealing layer ensemble allowed for a surface-averaged temperature swing of 40°C at the low load and 100°C at the high load for the intake valve surface. The exhaust valve was predicted to experience less surface temperature swing due to the interference from the exhaust event heating from the valve backside, as discussed in Section 5.3.2: Realistic Engine Geometries. For each of the engine builds with insulated valves, the non-insulated valve temperatures (e.g. the exhaust valves when the engine was built with insulated intake valves, and vice versa) were very similar to the baseline temperatures, displaying the similarity of the general thermal environment present between engine builds. Heat flux measurements taken with the heat flux probe mounted in the cylinder head with each hardware set at each operating point also confirmed the similarity of the thermal environments, but are not shown for brevity.

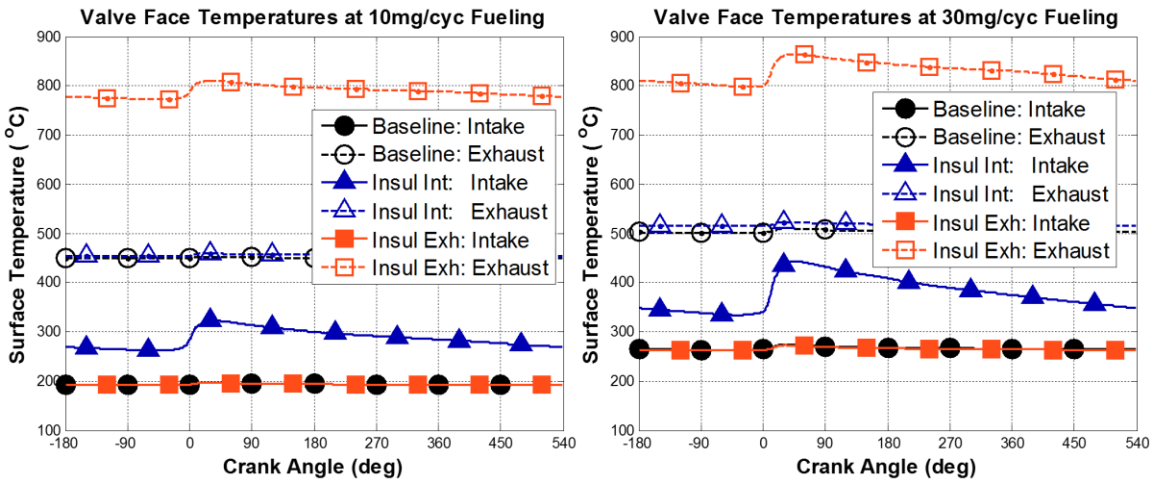

Figure 7-7: Valve Face Temperatures for Baseline and Insulated Engine Builds at 10 and 30mg Fueling Rates

Both the insulated intake and exhaust valve average surface temperatures were considerably higher than the baseline un-insulated temperatures. This is caused by the thickness of the insulating layer in these components, estimated to be 40% of the $depth_{1\%}$ which is considerably more than the ideal thickness. The increase in average temperature for the exhaust valve is higher than the intake valve because of the permeable porosity losses assumed to be occurring due to the higher hydrocarbon and lower NSFC measurements with coated valves. The intake valve has more than sufficient capacity to shed excess heat with the cooling effect of the intake air flow, but the exhaust valve has limited means to reject that additional energy and thus increases in temperature to a greater extent.

Experiments with insulated piston surfaces resulted in a failure of the adhesion between the bonding layer and the aluminum. This resulted in the disconnection of the entire insulating layer from the piston, and subsequent engine damage. Greater effort must be exerted to improve the bonding method between the microsphere insulation and aluminum piston before parts can be reliably tested.

7.6. Summary and Conclusions

- The success of any insulating material that relies on porosity to achieve low thermal conductivity and low heat capacity is dependent on adequate sealing of that porosity. Permeable porosity losses can easily overshadow the potential gains through surface temperature swing.
- Addition of thin dense layers to attempt to seal the porosity can result in a significant degradation of the surface temperature swing, and the underlying insulation thickness must be adjusted to compensate.

- A material was created with a thermal conductivity of only 0.2 W/m-K and a volumetric heat capacity of 250 kJ/m^3-K through the inclusion of over 95% porosity. This material was capable of withstanding the environment within an internal combustion engine, although the sealing layer showed continuing degradation throughout testing.
- Sealing layer integrity and bonding between the insulating layer and aluminum components both require further improvement before satisfactory results are recorded.

8. Conclusions and Future Directions

8.1. Summary and Conclusions

Temperature-swing materials can offer a substantial benefit to reciprocating internal combustion engine brake efficiency by reducing heat transfer during portions of the engine cycle when it can make the most difference while avoiding the typical pitfalls of conventional insulation techniques. Ideally, a reduction in heat transfer during combustion and the expansion and exhaust strokes is beneficial to brake work and exhaust temperature because it allows the energy that is prevented from leaving the gas to be harvested by the piston during the expansion stroke, and directly increases the exhaust gas temperature for aftertreatment or compounding strategies in the exhaust. Conversely, an increase in heat transfer during the intake and compression strokes will improve the volumetric efficiency by inducting a cooler, more dense intake air charge, by reducing the work required during the compression stroke, and decreasing the likelihood of unintentional end-gas autoignition. Materials designed to allow the wall surface temperature to track the gas temperature to a significant degree can accomplish this task, selectively affecting heat transfer from the gas to be most effective in improving engine performance.

- Low heat capacity and low thermal conductivity both promote surface temperature swing in combustion chamber wall materials. Equivalent percentage reductions in either volumetric capacity or conductivity will have the same net effect on the surface temperature swing and thus engine performance effects, assuming that the thickness of the coating is appropriately varied according to the $\text{depth}_{1\%}$ derived from the characteristic thermal penetration depth.
- Coating thickness of a temperature-swing material has a large influence on the amount of temperature swing, the total insulation capability, and the rate of temperature decay during expansion and exhaust, which all will affect engine performance. The ideal thickness to minimize the wall temperature during the intake stroke while maximizing the total temperature swing to achieve the greatest reduction in heat losses during combustion and expansion is approximately 25% of the $\text{depth}_{1\%}$. This thickness is a balance between allowing enough thickness for substantial temperature swing to develop on the surface, while allowing adequate cooling through the coating backside to

the substrate so that the surface temperature decays to the un-coated surface temperature during the intake stroke.

- Wall temperature swing in response to the engine's instantaneous heat flux can reduce heat transfer more effectively than conventional insulation without the traditional negative impacts on volumetric efficiency or in-cylinder thermal environment during intake and compression.
- Approximately 1/3 of the energy prevented from leaving the gas during the expansion stroke can be recovered by the piston using wall temperature swing coatings, while conventional coatings force the engine to expend much of that recovered energy on additional compression.
- Greater benefits are found at high load where the heat transfer rates that drive wall temperature swing are highest.
- Porous heat losses were driven by combustion chamber gasses driven into the permeable coating, experiencing heat losses beyond typical convection as they are forced to the temperature of the coating. These porous losses remove energy from the combustion chamber near TDC and throughout the combustion process when it is most harmful to the four-stroke process, having a severely negative impact on indicated work.
- Lengthened heat release tails were observed with the conventional BNT piston coatings, indicating fuel was trapped within or on the surface of the porous coating and effectively prevented from combusting until much later in the cycle.
- Successful implementation of temperature-swing enabling insulation requires negligible permeable porosity, necessitating a way of sealing the porosity from combustion gasses.
- Addition of thin dense layers to attempt to seal the porosity can result in a significant degradation of the surface temperature swing, and the underlying insulation thickness must be adjusted to compensate.
- A material was created with a thermal conductivity of only 0.2 W/m-K and a volumetric heat capacity of 250 kJ/m^3-K through the inclusion of over 95% porosity. This material was capable of withstanding the environment within an internal combustion engine, although the sealing layer showed continuing degradation throughout testing.
- The success of any insulating material that relies on porosity to achieve low thermal conductivity and low heat capacity is dependent on adequate sealing of that porosity. Permeable porosity losses can easily overshadow the potential gains through surface temperature swing.

8.2. Future Work and Directions

Continued work is necessary to address the issues with sealing the porosity and ensuring adequate bonding between the novel thermal barrier material and engine components. These criteria must be met to achieve significant improvements in engine performance and durability necessary for commercialization. Additionally, greater flexibility in construction is necessary to allow for the production of the complex combustion chamber geometries necessitated by more advanced combustion systems.

The solution that was chosen and developed for this document is certainly not the only possibility for achieving the desired temperature swing. Further study into other materials, geometries, and processing methods is necessary to find new methods to enable surface temperature swing. Alternative ways of providing sealing and insulation may prove to be more commercially viable due to durability, cost, ease of processing and application, or performance.

Lastly, greater fidelity in wall temperature swing modeling efforts is necessary to fully capture the spatial effects of flame fronts passing across a fixed wall. This is expected to increase the estimated local temperature swing and potentially improve the predicted engine performance over the models used herein. Use of a single-zone temperature and heat transfer model dulls the local transient spike in heat transfer as the flame passes a fixed location in an attempt to provide an area-averaged global heat loss rate, but this reduces the calculated wall temperature swing by an estimated 50% or more. Resolution of the walls into finer elements, coupled with the tracking of flame front wetted areas, burned and unburned temperatures, and burned and unburned heat transfer coefficients should provide more detailed predictions.

9. Works Cited

Alkidas, A. (1980). Heat Transfer Characteristics of a Spark-Ignition Engine. *Journal of Heat Transfer*, 102(2):189-193.

Anderson, C., & Prakash, C. (1985). *The Effects of Variable Conductivity on Unsteady Heat Transfer in Deposits.* SAE Technical Paper 850048.

Ando, H. A. (2009). Flow, Mixture Preparation and Combustion in Four-Stroke Direct-Injection Gasoline Engines. In C. K. Arcoumanis, *Flow and Combustion in Piston Engines* (pp. 137-171). Berlin: Springer.

Annand, J. (1963). Heat Transfer in the Cylinders of Reciprocating Internal Combustion Engines. *Proc. Inst. Mech. Eng.*, 177(1): 973-996.

Aoki, O., Tanaka, T., Nakao, Y., Kiyosue, R., Harada, T., & Yamamoto, H. (2015). *Analysis of Heat Transfer Phenomema on High Response Heat Insulation Coatings by Instantaneous Heat Flux Measurement and Boundary Layer Visualization.* SAE Technical Paper 2015-01-1996.

Applied Thin Films Inc. (2011). *NanoEngineered Thermal Barrier Coatings.* Evanston, Il.: atfinet.com.

Assanis, D., & Badillo, E. (1987). *Transient Heat Conduction in Low-Heat-Rejection Engine Combustion Chambers.* SAE Technical Paper 870156.

Assanis, D., & Badillo, E. (1989). *Evaluation of Alternative Thermocouple Designs for Transient Heat Transfer Measurements in Metal and Ceramic Engines.* SAE Technical Paper 890571.

Assanis, D., & Mathur, T. (1990). *The Effect of Thin Ceramic Coatings on Spark-Ignition Engine Performance.* SAE Technical Paper 900903.

Assanis, D., Wiese, K., Schwarz, E., & Bryzik, W. (1991). *The Effects of Ceramic Coatings on Diesel Engine Performance and Exhaust Emissions.* SAE Technical Paper 910460.

Bozza, F., Gimelli, A., Merola, S., & Vaglieco, B. (2005). *Validation of a Fractal Combustion Model through Flame Imaging.* SAE Technical Paper 2005-01-1120.

Brussovansky, S., Heywood, J., & Keck, J. (1992). *Predicting the Effects of Air and Coolant Temperature, Deposits, Spark Timing and Speed on Knock in Spark Ignition Engines.* SAE Technical Paper 922324.

Bryzik, W., & Kamo, R. (1983). *TACOM/Cummins Adiabatic Engine Program.* SAE Technical Paper 830314.

Bunce, M., & Blaxill, H. (2016). *Sub-200 g/kWhr BSFC on a Light Duty Gasoline Engine.* SAE Technical Paper 2016-01-0709.

Chang, J., Guralp, O., Filipi, Z., Assanis, D., Kuo, T., Najt, P., & Rask, R. (2004). *New Heat Transfer Correlation for an HCCI Engine Derived from Measurements of Instantaneous Surface Heat Flux.* SAE Technical Paper 2004-01-2996.

Chang, K., Lavoie, G., Babajimopoulos, A., Filipi, Z., & Assanis, D. (2007). *Control of a Multi-Cylinder HCCI Engine During Transient Operation by Modulating Residual Gas Fraction to Compensate for Wall Temperature Effects.* SAE Technical Paper 2007-01-0204.

Cheng, W., Wong, V., & Gao, F. (1989). *Heat Transfer Measurement Comparisons in Insulated and Non-Insulated Diesel Engines.* SAE Technical Paper 890570.

Choate, P., & Edwards, J. (1993). *Relationship Between Combustion Chamber Deposits, Fuel Composition, and Combustion Chamber Deposit Structure.* SAE Technical Paper 932812.

Cole, R., & Alkidas, A. (1985). *Evaluation of an Air-Gap-Insulated Piston in a Divided-Chamber Diesel Engine.* SAE Technical Paper 850359.

Dec, J., & Sjoberg, M. (2003). *A Parametric Study of HCCI Combustion - The Sources of Emissions at Low Loads and the Effects of GDI Fuel Injection.* SAE Technical Paper 2003-01-0752.

Dickey, D. (1989). *The Effect of Insulated Combustion Chamber Surfaces on Direct-Injected Diesel Engine Performance, Emissions and Combustion.* SAE Technical Paper 890292.

Fansler, T. R. (2015). Combustion Instability in Spray-Guided Stratified-Charge Engines: A Review. *International Journal of Engine Research*, 16(3): 260-305.

Flynn, G., & MacBeth, J. (1986). *A Low Friction, Unlubricated, Uncooled Ceramic Diesel Engine - Chapter II.* SAE Technical Paper 860448.

Frame, E. (1983). *High-Temperature Lubricants for Minimum-Cooled Diesel Engines.* AD-A142 426: U.S. Army Fuels and Lubricants Research Laboratory, Southwest Research Institute.

Fukui, K., Wakisaka, Y., Nishikawa, K., Hattori, Y., Kosaka, H., & Kawaguchi, A. (2016). *Development of the Instantaneous Temperature Measurement Technique of the Combustion Chamber Surface and Verification of the Temperature Swing Concept.* SAE Technical Paper 2016-01-0675.

Furuhama, S., & Enomoto, Y. (1987). *Heat Transfer into Ceramic Combustion Wall of Internal Combustion Engines.* SAE Technical Paper 870153.

Gatowski, J., Balles, E., Chun, K., Nelson, F., Ekchian, J., & Heywood, J. (1984). *Heat Release Analysis of Engine Pressure Data.* SAE Technical Paper 841359.

General Motors Engine Test Code Committee. (1994). *GM Automotive Engine Test Code Book for Spark Ignition Engines* (7th ed.). Warren, MI: General Motors.

Guralp, O., Hoffman, M., Assanis, D., Filipi, Z., Kuo, T., Najt, P., & Rask, R. (2006). *Characterizing the Effect of Combustion Chamber Deposits on a Gasoline HCCI Engine.* SAE Technical Paper 2006-01-3277.

Guralp, O., Najt, P., & Filipi, Z. (2012). *Method for Determining Instantaneous Temperature at the Surface of Combustion Chamber Deposits in an HCCI Engine.* Vancouver, BC, Canada: ASME ICEF 2012-92188.

Harder, R., & Anderson, C. (1988). Investigation of Combustion-Chamber Deposit Thermal Behavior Utilizing Optical Radiation Measurements in a Fired Engine. *Combustion, Science & Technology*, 60(4-6):423-440.

Havstad, P., Garwin, I., & Wade, W. (1986). *A Ceramic Insert Uncooled Diesel Engine.* SAE Technical Paper 860447.

Heywood, J. (1988). *Internal Combustion Engine Fundamentals.* New York NY: McGraw-Hill Book Company.

Hoag, K., Brands, M., & Bryzik, W. (1985). *Cummins/TACOM Adiabatic Engine Program.* SAE Technical Paper 850356.

Hoffman, M., Lawler, B., Guralp, O., Najt, P., & Filipi, Z. (2015). The Impact of a Magnesium Zirconate Thermal Barrier Coating on Homogeneous Charge Compression Ignition Operational Variability and the Formation of Combustion Chamber Deposits. *International Journal of Engine Research*, 16(8): 968-981.

Hohenberg, G. (1979). *Advanced Approaches for Heat Transfer Calculations.* SAE Technical Paper 790825.

Hu, H., & Keck, J. (1987). *Autoignition of Adiabatically Compressed Combustible Gas Mixtures.* SAE Technical Paper 872110.

Imaoka, Y., Shouji, K., Inoue, T., & Noda, T. (2016). A Study on Combustion Technology for a High Compression Ratio Engine: The Influence of Combustion Chamber Wall Temperature on Knocking. *SAE International Journal of Engines*, 9(2):768-776:2016-01-0703.

Kalghatgi, G. (1995). *An Experimental Study of Combustion Chamber Deposits and Their Effects in a Spark-Ignition Engine.* SAE Technical Paper 950680.

Kalghatgi, G. (1995). *Combustion Chamber Deposits in Spark-Ignition Engines: A Literature Review.* SAE Technical Paper 952443.

Kamo, R., & Bryzik, W. (1978). *Adiabatic Turbocompound Engine Performance Prediction.* SAE Technical Paper 780068.

Kamo, R., Assanis, D., & Bryzik, W. (1989). *Thin Thermal Barrier Coatings for Engines.* SAE Technical Paper 890143.

Kawaguchi, A., Iguma, H., Yamashita, H., Takada, N., Nishikawa, N., Yamashita, C., . . . Fukui, K. (2016). *Thermo-Swing Wall Insulation Technology; - A Novel Heat Loss Reduction Approach on Engine Combustion Chamber.* SAE Technical Paper 2016-01-2333.

Kogo, T., Hamamura, Y., Nakatani, K., Toda, T., Kawaguchi, A., & Shoji, A. (2016). *High Efficiency Diesel Engine with Low Heat Loss Combustion Concept - Toyota's Inline 4-Cylinder 2.8-Liter ESTEC 1GD-FTV Engine.* SAE Technical Paper 2016-01-0658.

Kosaka, H., Wakisaka, Y., Nomura, Y., Hotta, Y., Koike, M., Nakakita, K., & Kawaguchi, A. (2013). Concept of "Temperature Swing Heat Insulation" in Combustion Chamber Walls, and Appropriate Thermo-Physical Properties for Heat Insulation Coat. *SAE International Journal of Engines*, 6(1):142-149: 2013-01-0274.

Kumar, C., & Nagarajan, G. (2012). Performance and Emission Characteristics of a low heat rejection spark ignited engine fuelled with E20. *Journal of Mechanical Science and Technology, 26 (4), 1241-1250*, 26(4):1241-1250.

LaVigne, P., Anderson, C., & Prakash, C. (1986). *Unsteady Heat Transfer and Fluid Flow in Porous Combustion Chamber Deposits.* SAE Technical Paper 860241.

Livengood, J., & Wu, P. (1955). Correlation of Autignition Phenomena in Internal Combustion Engines and Rapid Compression Machines. *Proceedings of the Fifth International Symposium on Combustion*, 347-356.

Lu, J., Ezekoye, D., Iiyama, A., & Greif, R. (1989). *Effect of Knock on Time-Resolved Engine Heat Transfer.* SAE Technical Paper 891795.

McKenzie, J., & Cheng, W. (2016). *The Anatomy of Knock.* SAE Technical Paper 2016-01-0704.

Miyairi, Y. (1988). *Computer Simulation of an LHR DI Diesel Engine.* SAE Technical Paper 880187.

Moore, C., & Hoehne, J. (1986). *Combustion Chamber Insulation Effects on the Performance of a Low Heat Rejection Cummins V-903 Engine.* SAE Technical Paper 860317.

Morel, T., Fort, E., & Blumberg, P. (1985). *Effect of Insulation Strategy and Design Parameters on Diesel Engine Heat Rejection and Performance.* SAE Technical Paper 850506.

Morel, T., Keribar, R., & Blumberg, P. (1985). *Cyclical Thermal Phenomena in Engine Combustion Chamber Surfaces.* SAE Technical Paper 850360.

Morel, T., Keribar, R., Blumberg, P., & Fort, E. (1986). *Examination of Key Issues in Low Heat Rejection Engines.* SAE Technical Paper 860316.

Mutzke, J., Scott, B., Stone, R., & Williams, J. (2016). *The Effect of Combustion Knock on the Instantaneous Heat Flux in Spark Ignition Engines.* SAE Technical Paper 2016-01-0700.

Najt, P., & Foster, D. (1983). *Compression-Ignited Homogeneous Charge Combustion.* SAE Technical Paper 830264.

Nakamura, H., Ohinouye, T., Hori, K., Kiyota, Y., Nakagami, T., Akishino, K., & Tsukamoto, Y. (1978). *Development of a New Combustion System (MCA-JET) in Gasoline Engine.* SAE Technical Paper 780007.

Nakanishi, K., Hirano, T., Inoue, T., & Ohigashi, S. (1975). *The Effects of Charge Dilution on Combustion and Its Improvement - Flame Photograph Study.* SAE Technical Paper 750054.

Nakic, D., Assanis, D., & White, R. (1994). *Effect of Elevated Piston Temperature on Combustion Chamber Deposit Growth.* SAE Technical Paper 940948.

Namazian, M., & Heywood, J. (1982). *Flow in the Piston-Cylinder-Ring Crevices of a Spark-Ignition Engine: Effect on Hydrocarbon Emissions, Efficiency, and Power.* SAE Technical Paper 820088.

Nusselt, W. (1928). Der Warmeubergang zwischen Arbeitsmedium und Zylinder wand in Kolbenmaschinen. *Forschungsheft*, 300.

O'Donnell, R., Powell, T., Hoffman, M., Jordan, E., & Filipi, Z. (2016). Inverse Analysis of In-Cylinder Gas-Wall Boundary Conditions: Investigation of a Yttria Stabilized Zirconia Thermal Barrier Coating for Homogeneous Charge Compression Ignition. *Internal Combustion Engine Fall Technical Conference* (pp. ICEF2016-9401). Greenville, SC: ASME.

Omega. (2016). *Type J Reference Tables, N.I.S.T. Monograph 175 Revised to ITS-90*. Retrieved February 28, 2014, from http://www.omega.com/temperature/Z/pdf/z203.pdf

Onishi, S., Jo, S., Shoda, K., Do, P., & Kato, S. (1979). *Active Thermo-Atmosphere Combustion (ATAC) - A New Combustion Process for Internal Combustion Engines.* SAE Technical Paper 790501.

Overbye, V., Bennethum, J., Uyehara, O., & Myers, P. (1961). *Unsteady Heat Transfer in Engines.* SAE Technical Paper 610041.

Powell, T., O'Donnell, R., Hoffman, M., & Filipi, Z. (2016). Impact of a Yttria-Stabilized Zirconia Thermal Barrier Coating on HCCI Engine Combustion, Emissions, and Efficiency. *Internal Combustion Engine Fall Technical Conference* (pp. ICEF2016-9391). Greenville, SC: ASME.

Rassweiler, G., & Withrow, L. (1935). *Flame Temperatures Vary with Knock and Combustion-Chamber Position.* SAE Technical Paper 350091.

Rassweiler, G., & Withrow, L. (1938). *Motion Pictures of Engine Flames Correlated with Pressure Cards.* SAE Technical Paper 380139.

Sambasivan, S. S. (2010). *United States Patent No. 7,838,121 B1.*

Semisonic (1998). Closing Time.

Serrano, J., Arnau, F., Martin, J., Hernandez, M., & Lombard, B. (2015). *Analysis of Engine Walls Thermal Insulation: Performance and Emissions.* SAE Technical Paper 2015-01-1660.

Shabir, M., Authars, S., Ganesan, S., Karthik, R., & Madhan, S. (2010). *Low Heat Rejection Engines - Review.* SAE Technical Paper 2010-01-1510.

Siegla, D., & Amann, C. (1984). *Exploratory Study of the Low-Heat-Rejection Diesel for Passenger Car Application.* SAE Technical Paper 840435.

Sihling, K., & Woschni, G. (1979). *Experimental Investigation of the Instantaneous Heat Transfer in the Cylinder of a High Speed Diesel Engine.* SAE Technical Paper 790833.

Sjoberg, M., Dec, J., Babajimopoulos, A., & Assanis, D. (2004). *Comparing Enhanced Natural Thermal Stratification Against Retarded Combustion Phasing for Smoothing of HCCI Heat-Release Rates.* SAE 2004-01-2994.

Stivender, D. (1971). *Development of a Fuel-Based Mass Emission Measurement Procedure.* SAE Technical Paper 710604.

Sudhakar, V. (1984). *Performance Analysis of Adiabatic Engine.* SAE Technical Paper 840431.

Syrimis, M., Shigahara, K., & Assanis, D. (1996). *Correlation Between Knock Intensity and Heat Transfer Under Light and Heavy Knocking Conditions in a Spark Ignition Engine.* SAE Technical Paper 960495.

Thring, R. (1986). *Low Heat Rejection Engines.* SAE Technical Paper 860314.

Thring, R. (1989). *Homogeneous-Charge Compression Ignition (HCCI) Engines.* SAE Technical Paper 89206.

Timoney, S., & Flynn, G. (1983). *A Low Friction , Unlubricated SiC Diesel Engine.* SAE Technical Paper 830313.

Toyama, K., Yoshimitsu, T., Nishiyama, T., Shimauchi, T., & Nakagaki, T. (1983). *Heat Insulated Turbocompound Engine.* SAE Technical Paper 831345.

Tsutsumi, Y., Nomura, K., & Nakamura, N. (1990). *Effect of Mirror-Finished Combustion Chamber on Heat Loss.* SAE Technical Paper 902141.

Wade, W., Havstad, P., Ounsted, E., Trinkler, F., & Garwin, I. (1984). Fuel Economy Opportunites with an Uncooled DI Diesel Engine. *IMechE/SAE*, C432, pp 11-24.

Wakisaka, Y., Inayoshi, M., Fukui, K., Kosaka, H., Hotta, Y., Kawaguchi, A., & Takada, N. (2016). Reduction of Heat Loss and Improvement of Thermal Efficiency by Application of "Temperature Swing" Insulation to Direct-Injection Diesel Engines. *SAE International Journal of Engines*, 9(3): 1449-1459: 2016-01-0661.

Wallace, F., Kao, T., Alexander, W., Cole, A., & Tarabad, M. (1983). *Thermal Barrier Pistons and Their Effect on the Performance of Compound Diesel Engine Cycles.* SAE Technical Paper 830312.

Wallace, F., Kao, T., Tarabad, M., Alexander, W., & Cole, A. (1984). Thermally Insulated Diesel Engines. *Proc. Instn. Mech. Engrs*, 198(2): 97-105.

Wallace, F., Way, R., & Vollmert, H. (1979). *Effect of Partial Suppression of Heat Loss to Coolant on the High Output Diesel Engine Cycle.* SAE Technical Paper 790823.

Walzer, P., Heinrich, H., & Langer, M. (1985). *Ceramic Components in Passenger-Car Diesel Engines.* SAE Technical Paper 850567.

Watts, P., & Heywood, J. (1980). *Simulation Studies of the Effects of Turbocharging and Reduced Heat Transfer on Spark-Ignition Engine Operation.* SAE Technical Paper 800289.

Way, R., & Wallace, F. (1979). *Results of Matching Calculations for Turbocharged and Compound Engines with Reduced Heat Loss.* SAE Technical Paper 790824.

Wisniewski, T. (1998). *Experimental Study of Heat Transfer on Exhaust Valves of 4C90 Diesel Engine.* SAE Technical Paper 981040.

Wong, V., Bauer, W., Kamo, R., Bryzik, W., & Reid, M. (1995). *Assessment of Thin Thermal Barrier Coatings for I.C. Engines.* SAE Technical Paper 950980.

Wood, B., & Anderson, C. (1993). *Gasification of Porous Combustion Chamber Deposits in a Spark Ignition Engine.* SAE Technical Paper 930773.

Woschni, G. (1967). *A Universally Applicable Equation for the Instantaneous Heat Transfer Coefficient in the Internal Combustion Engine.* SAE Transactions, Vol. 76, 3065.

Woschni, G., Spindler, W., & Kolesa, K. (1987). *Heat Insulation of Combustion Chamber Walls - A Measure to Decrease the Fuel Consumption of IC Engines?* SAE Technical Paper 870339.

Yang, L., Hamada, A., & Ohtsubo, K. (2000). *Engine Valve Temperature Simulation System.* SAE Technical Paper 2000-01-0564.

Yoshimitsu, T., Toyama, K., Sato, F., & Yamaguchi, H. (1982). *Capabilities of Heat Insulated Diesel Engine.* SAE Technical Paper 820431.

Yun, H., & Mirsky, W. (1974). *Schlieren-Streak Measurements of Instantaneous Exhaust Gas Velocities from a Spark Ignition Engine.* SAE Technical Paper 741015.

Zhao, F. H. (2002). *Automotive Gasoline Direct-Injection Engines.* Warrendale, PA: SAE International.

zur Loye, A., & Bracco, F. (1987). *Two-Dimensional Visualization of Premixed-Charge Flame Structure in an IC Engine.* SAE Technical Paper 870454.